NAIST-IS-DD0861026

**Doctoral Dissertation**

# Respiratory Motion Tracking and Correction Simulation for Coronary Magnetic Resonance Angiography

Florencio Rusty Punzalan

March 8, 2013

Department of Bioinformatics and Genomics
Graduate School of Information Science
Nara Institute of Science and Technology

A Doctoral Dissertation
submitted to Graduate School of Information Science,
Nara Institute of Science and Technology
in partial fulfillment of the requirements for the degree of
Doctor of ENGINEERING

Florencio Rusty Punzalan

Thesis Committee:

| | |
|---|---|
| Professor Kotaro Minato | (Supervisor) |
| Professor Shigehiko Kanaya | (Co-supervisor) |
| Associate Professor Tadao Sugiura | (Co-supervisor) |
| Assistant Professor Tetsuo Sato | (Co-supervisor) |

# Respiratory Motion Tracking and Correction Simulation for Coronary Magnetic Resonance Angiography*

Florencio Rusty Punzalan

**Abstract**

Coronary magnetic resonance angiography (CMRA) is a noninvasive and non-exercise diagnostic tool that can visualize plaque progression in the coronary arteries. However, image quality has been hampered by image artifacts from sources such as heart motion during respiration. This study proposes a simulation platform that may help in the estimation of subject-specific respiratory motion parameters to correct for respiratory motion during CMRA scans.

The simulation platform involves the estimation of respiratory motion from subject scout scans and the acquisition of simulated CMRA scans using different respiratory motion correction methods. The motion coefficients of the upper and lower heart were estimated for different subjects. The variability of the upper and lower heart motion measured from MR scout scans and its effect on CMRA image quality was also assessed using the simulation platform.

In order to increase the accuracy of motion coefficient estimation, an intensity standardization method was introduced to standardize the image intensity scale of the scout scans. Joint histogram registration was done for the scout scans to achieve a more uniform gray level intensity distribution and make the edge detection more accurate.

To simulate respiratory motion, a high-resolution 3-D coronary heart reference image is deformed using the estimated linear transformation from a series

*Doctoral Dissertation, Department of Bioinformatics and Genomics, Graduate School of Information Science, Nara Institute of Science and Technology, NAIST-IS-DD0861026, March 8, 2013.

of volunteer coronal scout scans. The deformed and motion-affected 3-D coronary images are used to generate segmented $k$-space data to represent MR data acquisition affected by respiratory motion. The acquired $k$-space data are then corrected using different respiratory motion correction methods and then converted back to image data. The resulting images are quantitatively compared with each other using image-quality measures. Simulation experiment results are validated by acquiring actual CMRA scans using the correction methods used in the simulation. During the simulation of one-dimensional motion correction methods, the use of the mean correction factor gave the highest image quality improvement in signal-to-noise ratio, contrast-to-noise ratio, and vessel edge definition in relation to data without motion correction. Simulation experiments also demonstrated the effectiveness of a subject-specific respiratory gating method for coronary MR angiography. The simulation platform may be used as a tool to determine the appropriate respiratory motion parameters that can help acquire good-quality CMRA scans.

**Keywords:**

subject-specific motion correction; respiratory gating simulation; coronary MR angiography; image quality assessment; intensity standardization.

# Contents

**1 Introduction** **1**
1.1. Background and Motivation . . . . . 1
1.2. Research Aim and Approach . . . . . 4
1.3. Thesis Layout . . . . . 6

**2 Literature Review: Magnetic Resonance Imaging of the Heart and Coronary Arteries** **9**
2.1. Cardiac and Coronary Artery Morphology . . . . . 9
2.2. Coronary Artery Disease . . . . . 10
2.3. Imaging of Coronary Arteries . . . . . 12
2.4. Coronary Magnetic Resonance Angiography . . . . . 14
2.4.1 MRI Image Acquisition . . . . . 15
2.4.2 Motion during CMRA Image Acquisition . . . . . 15
2.5. Respiratory Motion . . . . . 18
2.5.1 Respiratory Motion of the Heart . . . . . 19
2.5.2 Effects of Respiratory during CMRA Imaging . . . . . 22
2.6. Respiratory Motion Correction . . . . . 23
2.6.1 Respiratory Gating in CMRA . . . . . 23
2.6.2 Summary . . . . . 24

**3 Subject-Specific Respiratory Motion Gating** **25**
3.1. Prospective Navigator-guided Gating . . . . . 26
3.1.1 Navigators . . . . . 27
3.1.2 Prospective Gating . . . . . 29
3.2. Motion Models in Subject-specific Respiratory Motion Correction 31

3.2.1 Rigid Body Translation . . . 31
3.2.2 Non-Rigid Motion with Translation and Scaling . . . 34
3.2.3 Affine Transformation . . . 36
3.3. Method . . . 38
3.4. Results . . . 40
3.5. Discussion . . . 42

**4 Respiratory Motion Correction Simulation Platform 46**
4.1. Method . . . 48
4.1.1 Simulation Platform Algorithm . . . 48
4.1.2 Modeling Respiratory Motion . . . 49
Motion Parameter Estimation . . . 50
Respiratory Waveform Generation . . . 52
Spatial Transformation of Reference Image . . . 53
4.1.3 CMRA Motion Correction Simulator . . . 55
Acquisition of Uncorrected $k$-space Data . . . 55
Motion Correction Simulation . . . 57
4.2. Experiments . . . 58
4.2.1 Image Quality Assessment . . . 59
4.3. Results . . . 61
4.3.1 Coronary Artery Visualization . . . 62
4.3.2 Simulation vs. Reference Scan . . . 64
4.3.3 Simulation vs. Clinical Scan . . . 65
4.4. Discussion . . . 67
4.5. Conclusion . . . 69

**5 Intensity Standardization 71**
5.1. Introduction . . . 71
5.1.1 Intensity Standardization . . . 72
5.1.2 Diffusion-weighted MR Imaging . . . 74
5.2. Method . . . 77
5.2.1 Data Acquisition and Joint Histogram Computation . . . 78
5.2.2 Intensity Standardization . . . 81
5.3. Results . . . 82

5.4. Discussion . . . . . 84

**6 Conclusion** **86**

6.1. Subject-specific Respiratory Motion Correction . . . . . 86

6.2. Respiratory Motion Correction Simulation Platform . . . . . 87

6.3. Future Work . . . . . 88

**Acknowledgements** **89**

**Publication List** **91**

**References** **92**

References . . . . . 92

# List of Figures

1.1 The resulting transverse scan with (A) without motion compensation, (B) cardiac motion compensation and (C) cardiac and respiratory motion compensation. . . . . 3

2.1 A view of the coronary artery system. The arteries supplying the posterior part of the heart are shown in a lighter shade. . . . . 10
2.2 The cause of coronary artery disease. (A) shows a normal artery with normal blood flow while (B) shows an artery with plaque buildup. The inserts show the cross-section of the artery (US National Institute of Health). . . . . 11
2.3 The graph illustrates the top 10 causes of death for low-, middle-, and high-income countries (World Health Organization). . . . . 12
2.4 An coronary X-ray angiography of a patient with significant coronary occlusion. (A, B) The coronary angiography showed significant stenosis in mid-LAD (Image from [1]). . . . . 13
2.5 To create the actual MR image, the received signals are encoded into the three Cartesian coordinate directions. For an axial image, the frequency encoding gradient, phase encoding gradient and slice select gradient are in the $x$-, $y$-, and $z$-direction, respectively. . . . 16
2.6 Anatomical images of the heart and coronaries arteries gathered using coronary magnetic resonance angiography. The images are the coronal slice of the heart from the base of the aorta (A) to the lower part of the heart (D); AO, aorta; PV, pulmonary vein; RA, right atrium; RV, right ventricle; LA, left atrium; LV, left ventricle; LM, left main artery; RCA, right coronary artery; LCX, left circumflex artery; LAD, left anterior descending artery. . . . . 17

2.7 A schematic plot of respiratory waveform showing inspiration and expiration. Top portions correspond to end-expiration, where the relatively flat area is the functional residual capacity (Bernstein2004, 475). . . . . 19
2.8 Axial steady state free precession (SSFP) images with ghosting (A) and blurring (B) artifacts due to respiratory motion. . . . . 22

3.1 $k$-space trajectories for (a) linear, (b) 2D spiral, (c) 2D EPI, (d) 3D spherical, and (e) 2D orbital navigators. . . . . 28
3.2 Respiratory motion correction using a gating window. The diagrams show the selection of gating open/close points. The distance between the upper and lower threshold determines the size of the gating window, which is around 2-5 mm in cardiac MR scans . . . 30
3.3 Rigid motion model ROI for diaphragm and heart. The right side shows the tracked location of the diaphragm and the heart ROI for all images in the cine scout scan. . . . . 33
3.4 A scatter plot showing diaphragm and lower heart locations. The slope of the fitted linear regression lines, shown in the formula of the line, was designated as the SI translation correction factor. The R value is the Pearson product moment correlation coefficient and is a measure of the correlation between the diaphragm and the heart motion. . . . . 34
3.5 Coronal 2D SSFP MR images indicate the regions of interest (ROI) used for the nonrigid motion with SI translation and scaling (A), and affine motion model (B). The five ROIs in (B) were placed in the right (1), lower right (2), lower left (3), left (4), and upper (5) part of the heart. . . . . 35
3.6 Tracked locations of the upper and lower heart and diaphragm edges inside the regions of interests. . . . . 41
3.7 Comparison of simulated with the original acquired cine scan. The left column shows the original cine scout scan, the middle column the simulated slices using affine motion model and the right column is the image difference between a cine scan slice and a simulated scan slice. . . . . 43

3.8 The average computed image difference of the SI translation and affine motion model with respect to the original 2D dataset for all subjects. The 2D affine transformation consistently gave lower image difference with respect to the original scan. . . . . 43

4.1 Motion of the diaphragm and the thoracic cage during respiration. During inspiration, the diaphragm contracts forcing the abdominal contents including the heart to move downward. During expiration, the diaphragm relaxes, pushing the heart upwards. . . . . 50
4.2 Region-of-interest (ROI) motion tracking model for the diaphragm and heart. The right side shows the tracked location of the diaphragm and the heart ROI for all images in the scout scan. The tracked locations are used to compute the correlation coefficient ($CC$) values. . . . . 51
4.3 The motion curve of the diaphragm. The curve resembles that of a sinusoidal wave with a varying period $P_r = 4 - 5s$ (12–15 breathes per minute). . . . . 53
4.4 $k$-Space filling using segmented rectilinear sampling. A set of $k$-space lines was filled every heart beat with the $k$-space data from the sampled diaphragm position in the respiratory waveform. . . . 56
4.5 Method for generating the $k$-space dataset of the deformed cardiac model for each respiratory diaphragm position. The range of the respiratory waveform is divided into $k$ discrete levels or positions and in each level a transformed reference image is produced. The transformed 3D images are then converted to $k$-space data using FFT. The generated $k$-space data for each diaphragm displacement level are used to create the simulated CMRA acquisitions. . . . . 58
4.6 Curved MPR view of the right coronary artery near its origin in the aortic root (a). $ROI_{fg}$ was used for SNR calculations, whereas $ROI_{fg}$ and $ROI_{bg}$ were used for CNR calculations. (b) The plot shows the multiple intensity line profiles (b), which are used to compute for sigma of the fitted Gaussian curve (c). The value of sigma was used to compute for the vessel edge definition. . . . . 60

4.7 The measured correlation coefficient ($CC$) values for all the volunteer scans. $CC_{upr}$ and $CC_{lwr}$ indicates the translation of the upper and lower heart, respectively, for every 1 unit translation of the diaphragm. While $CC_{mean}$ refers to the average of the two aforementioned values. . . . . 62
4.8 Shown are the cross-sections of the right coronary artery from the simulated (upper two rows) and clinical scans (bottom two rows). The first row of the simulated and clinical scan corresponds to the distal cross-section of the artery while the second row of each scan shows the proximal cross-section. The columns lists the motion correction methods used in the scans; namely, no motion correction (A, F, K, P), $CF_{upr}$ (B, G, L, Q), $CF_{mean}$ (C, H, M, R), $CF_{lwr}$ (D, I, N, S), and standard correction factor (E, J, O, T). . . . . 63
4.9 The measured image quality in terms of signal-to-noise ratio (A), contrast-to-noise ratio (B), vessel edge definition (C) and vessel length (D) for a number of simulations using different combinations of upper and lower heart correlation coefficients. The set of columns labelled 0.7 / 2.0 means that the simulation values for the upper heart ($CC_{upr}$) and lower heart coefficient ($CC_{lwr}$) are 0.7 and 2.0, respectively. The five individual columns for each set correspond to the methods used in the respiratory motion correction, namely, no motion correction, using $CF_{upr}$, $CF_{mean}$, $CF_{lwr}$, and standard correction factor ($CF = 0.6$) . . . . . 65
4.10 By getting the coronal slice of the 3D image, the effect of respiratory motion on image quality and visibility of the distal RCA can be shown (top row). The middle coronal slice of the reference data (A) was compared with the simulated scans without motion correction (B), with $CC_{upr}$ (C) and with $CF_{mean}$ (D). The image difference between the reference slice and simulated slice without correction (E), with $CC_{upr}$ (F) and with $CF_{mean}$ (G) are also shown. 66

4.11 Contrast-to-noise ratio (CNR) measurements for the simulation and acquired clinical scans. The CNR was measured for both the upper and lower part of the heart. The trend of the CNR measurements were consistent for both the simulation and actual scan. The scan acquired using the mean correction factor ($CF = 0.51$) gave the highest average CNR between upper and lower heart CNR values while the standard correction factor ($CF = 0.60$), which is higher than the measured upper ($CF = 0.46$) and lower ($CF = 0.56$) factors, gave the lowest. . . . . 68
4.12 The vessel edge definition measurements for the simulation and actual clinical scans. The trends show a high correlation between the simulated and actual results ($P = 0.038$). . . . . 69

5.1 The difference in magnitude of water diffusion in a high (A) and low (B) cell concentration environment. The water molecules (black circles with arrows) within extracellular space, intracellular space and intravascular space all contribute to the measured MR signal. In the less cellular environment, the relative increase in extracellular space allows freer water diffusion than in a more compact environment. Defective cell membranes (B) also allow movement of water molecules between extracellular and intracellular spaces. 75
5.2 An example of a diffusion-weighted MR images containing liver metastasis. The images are obtained at different b values show large heterogeneous metastasis within right lobe of liver. Necrotic center of metastasis (squares) shows attenuation of signal intensity with increasing b values, indicating less restricted diffusion. By comparison, rim of tumor (rectangles) is more cellular and shows little signal attenuation with increasing b value [2]. . . . . 76
5.3 The abdominal T2, DWI $b_0$ and $b_1000$ images for subject 3 (top) and subject 5 (bottom). The DWI images are distorted, especially the images where b = 1000 s/mm$^2$ (b1000). There are spatial distortion with the b0 images as indicated by the presence of the curved spinal column (arrows). . . . . 79

5.4 Partitioning of the series of input (moving) and reference histograms into sets. The joint histograms were derived from the image pair of T2 and DWI images and have a total of 66 each for the input and reference. The 66 joints histogram is divided into $n$ number of partitions (e.g. $n = 3$) and all the histograms in the partition are added together. . . . . 80
5.5 The reference (A) and input (B) probability density function (pdf) of the summation of histograms using six partitions. These pdfs belong to the fourth partition (summation of joint histograms 34-44). 83
5.6 The graph shows the relative distance between the reference and current histograms with respect to the number of standardization partitions used in the intensity standardization. The optimal number of partitions (i.e. one with least difference) are 3 and 6. This means the use of 3-6 partitions offer the most similarity between input and reference pdf after image registration. . . . . 84

# List of Tables

2.1 Correction factors relating the SI motion of the heart and the diaphragm . . . . . 21

3.1 The measured motion correlation coefficients ($CC$) for the upper and lower heart using automatic and manual motion tracking. . . 42
3.2 Average image difference for 1D translation and affine motion model 44

4.1 Correlation coefficients used to transform the reference dataset. . 55
4.2 The average CNR values for the each correction factor used in the simulation and actual scans. The values for $CF_{upr}$, $CF_{mean}$ and $CF_{lwr}$ are 0.46, 0.51 and 0.56, respectively. . . . . 66

# List of Abbreviations

| | |
|---|---|
| **MRI** | Magnetic Resonance Imaging |
| **CMRA** | Coronary Magnetic Resonance Angiography |
| **CT** | Computed Tomography |
| **CAD** | Coronary Artery Disease |
| **ECG/EKG** | Electrocardiogram |
| **RCA** | Right Coronary Artery |
| **LAD** | Left Anterior Descending Artery |
| **LCX** | Left Circumflex Artery |
| **SI** | Superior-Inferior |
| **AP** | Anterior-Posterior |
| **ROI** | Region of Interest |
| **SNR** | Signal-to-Noise Ratio |
| **CNR** | Contrast-to-Noise Ratio |
| ***CF*** | Correction Factor |
| ***CC*** | (Motion) Correlation Coefficient |
| **DWI** | Diffusion-Weighted MR Imaging |
| **EPI** | Echo Planar Imaging |

# Chapter 1

# Introduction

> Where the spirit does not work
> with the hand, there is no art.
>
> Leonardo da Vinci

## 1.1. Background and Motivation

Coronary artery disease (CAD), a condition in which plaque builds up inside the coronary arteries, has been one of the leading causes of death in the world. It has been responsible for million deaths worldwide every year. The gold standard for determining the extent, location and severity of the disease is conventional x-ray angiography. However, this procedure is considered invasive and causes a modest amount of discomfort since a thin flexible tube called a catheter is inserted into the artery. It also involves the use of contrast agents, which may exclude certain patients from getting a scan and can cause serious side effects [3, 4]. This, together with the fact that a substantial minority of patients referred for diagnostic x-ray angiography are found to be without clinically significant coronary stenoses (defined as a luminal diameter reduction of at least 50%), highlights the need for better improved alternatives.

The most common alternatives for coronary artery imaging are X-ray angiography (XA), stress echocardiography, Computed Tomography (CT), and Coronary Magnetic Resonance Angiography (CMRA). XA is done by injecting a radio-

opaque contrast agent into the arteries and imaging using X-ray based techniques. During stress echocardiography, the sound waves of ultrasound are used to produce images of the heart at rest and at the peak of exercise. If a segment of the left ventricle does not receive optimal blood flow during exercise, that segment will demonstrate reduced contractions of heart muscle relative to the rest of the heart, thus indicating the presence of a blocked artery. This type of diagnostic, however, cannot image coronary artery directly and differentiate plaques. CT with bolus injections can detect blockage in arteries but it is intrusive and involves exposure to radiation during scan.

CMRA on the other hand, is a noninvasive and non-exercise diagnostic tool that can visualize plaque progression in the coronary arteries. The main advantage of this technique is the lack of exposure to ionizing radiation or ionated contrast media. In addition, the high tissue contrasts of the images allow for the detection and quantification of plaques and fats in the coronary vessels [5]. Coronary MRA can also be used with other magnetic resonance imaging (MRI) techniques for the assessment of cardiac structure, blood flow and viability [6]. However, image quality has been hampered by motion related artifacts and has not reached sufficient quality for widespread diagnostic application yet.

Images of the heart should be acquired rapidly and with high temporal resolution to reduce the motion artifacts. Unlike angiographic images acquired with catheter and contrast agents, CMRA scans take a long time to acquire. It takes minutes instead of seconds so the data acquisition has to account for both cardiac and respiratory motion. The scan has to have both good cardiac cycle and respiratory gating to avoid image blurring, ghosting, and low vessel visibility (Figure 1.1).

The motion of the heart during CMRA scan is composed of three components: motion resulting from voluntary or involuntary patient movement, motion due to cardiac cycle, and motion caused by respiration. The patient motion component is usually addressed by patient cooperation or by sedation or anesthesia in pediatric and other difficult cases. Cardiac-induced motion is commonly addressed by cardiac triggering using electrocardiogram (ECG/EKG). The goal is to acquire coronary MR images during the period of the cardiac cycle when the arteries are relatively stationary.

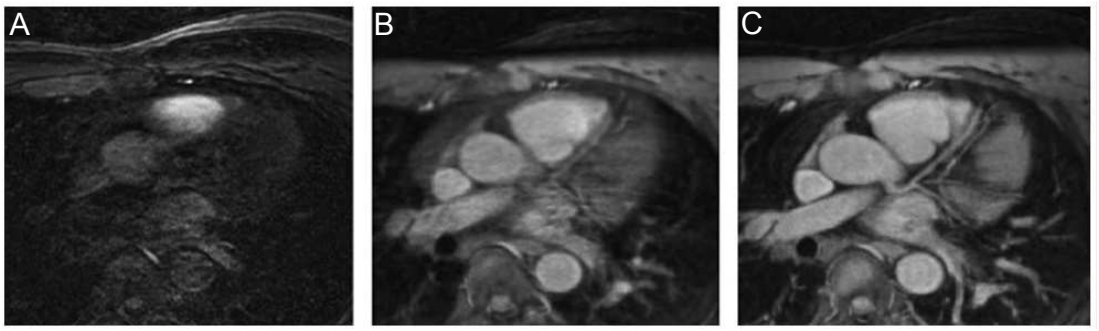


Figure 1.1: The resulting transverse scan with (A) without motion compensation, (B) cardiac motion compensation and (C) cardiac and respiratory motion compensation.

To control the patients respiratory motion during data acquisition, correction is typically done by asking the subject to perform breath-holds [7] or the position of the diaphragm is tracked using a respiratory navigator typically placed on the diaphragm [8]. Breath-hold techniques, which are limited to a 10 - 20 s window, suffer from scan time constraints and sometimes not feasible for patients with poor steady breath-holding capability. Navigator-based gating techniques meanwhile allow for free breathing [9], but suffer from a lower scan efficiency of roughly 30% - 50%, which results in scanning times of 10-15 minutes for conventional 3D coronary scan [10]. More sophisticated gating strategies using $k$-space reordering and weighting [11, 12] have been proposed and have potential to improve image quality and enable shorter scanning times.

A number of respiratory motion correction techniques are already published but there is a dearth of ways to compare the effectiveness of these approaches. This can be attributed to the variables involved in cardiac MR imaging aside from respiratory motion. In addition, evaluation of these respiratory motion correction methods requires *in vivo* examinations that requires a number of subjects or patients. MR scans *in vivo* also suffer from motion artifacts other than that from respiration, and includes cardiac cycle motion and magnetic inhomogeneities in scanners.

A simulation platform can address these limitations and allow for a comparison of different respiratory motion correction techniques. The main advantage of using simulations to model respiratory correction or gating is that it eliminates

other sources of artifacts like cardiac cycle, which varies during scan and contributes considerable image quality degradation during CMRA. Simulation allows a controlled environment where only respiratory motion affects image quality. In addition, simulation can also allow for evaluating different motion parameters to find the subject-specific parameters that can best correct for respiratory motion artifacts.

## 1.2. Research Aim and Approach

The main motivation for this dissertation is to improve respiratory motion correction for coronary MR angiography and to provide a simulation platform to evaluate and compare different navigator-motion correction techniques. The proposed platform would also includes the estimation of appropriate motion correction parameters that can be used to correction respiratory motion during CMRA scans.

Respiratory motion has been one of the major hindrances in obtaining higher quality coronary MR scans. We are interested in developing motion correction algorithms to improve on the quality and reliability in the images. In MR coronary angiography, motion compensation is vital since not only high resolution data needs to be acquired, it has to be acquired during a small rest period of the cardiac cycle. The small cardiac gating window further increases the need for efficient respiratory gating. This puts limitations in the temporal resolution of the scan and how long it takes to image the whole heart. Typical coronary imaging times are in the minutes and suffer from robustness and repeatability issues due to the motion variability in patients during scans.

Studies have shown that the largest component of the respiratory-induced motion of the heart is in the superior-inferior (SI) direction and with the large standard deviations suggesting high intersubject variability [13]. Although there are also other motion components due to the nonrigid motion of the heart during respiration, the current technology in navigator-guided scanners only allow for an SI correction factor as input parameter. The standard practice of using the fixed one-dimensional (1D) SI correction factor of 0.6 suggested by Wang et al [14] to correlate the heart motion with diaphragm displacement during respiratory

motion compensation does not consider the motion differences between patients. To overcome this limitation, we proposed a subject-specific approach to track the coronary artery by getting the optimal motion correction factor from the cine images and respiratory-gating simulation. To get the subject-specific correction factor, we implemented three different approaches that correlate the motion of the diaphragm and the heart from the cine scan (pre-scan). The first method correlates the SI motion of the right hemidiaphragm and a region of interest (ROI) in the lower part of the heart, below the right ventricle. The second method tracks the diaphragm, the lower right part of the heart, and the upper left heart near the aorta. The motion correlation between the diaphragm and the lower and upper heart are then computed to get the lower and upper heart correction factor, respectively. The average of the two correction factors served as the subject-specific mean SI correction factor. The third method also tracks the SI motion and scaling of the heart but adds the right-left (RL) motion displacement and rotation to get the two-dimensional (2D) affine motion parameters. Once the affine parameters are determined, the SI correction factor is estimated from the affine motion model.

In order to get the optimal one-dimensional SI motion correction factor, we need to compare the two correction factors that we computed from the two methods mentioned above. It may also be of benefit to compare the results of the two correction factor to that of the standard 0.6 factor. Initially, there is no way to know which method will give the better correction factor and results may also differ from patient to patient. However, it would be very time-consuming to get two or three coronary MR angiography scans and see which correction factor will give clearer images. Therefore, we proposed a simulation platform to compare and evaluate different SI motion correction factors.

The respiratory motion simulation platform takes the estimated affine motion parameters as inputs. These 2D affine motion parameters are computed from initial scout scan of the subject so they characterize the nonrigid motion heart better than just using 1D rigid translation. The motion parameters are then used to deform a reference three-dimensional (3D) scan to simulate the respiratory motion of the heart and a volumetric data set for each arbitrary diaphragm position. These data sets are then used to simulate motion correction with the

different SI correction factors as inputs. Each correction factor results to a motion corrected 3D scan. Finally, these scans are compared with each other so the quantitative image quality comparisons may be able to give the optimal subject-specific SI correction factor to be used in the actual scan.

## 1.3. Thesis Layout

The introduction and motivation for this dissertation are presented in Chapter 1. Chapter 2 gives a brief overview of the related literature that concerns the rest of the thesis. It gives an introduction about coronary artery disease and common imaging modalities used in its diagnosis. The next part details coronary MR angiography and its role as a non-invasive alternative to X-ray angiography. The later parts discuss the respiratory motion of the heart and its effects on coronary MR imaging as well as the published methods for respiratory motion correction.

Chapter 3 discusses the contribution in the area of respiratory gating. We have demonstrated that there is a major difference in the motion of the upper heart and lower heart during respiration. The lower heart moves to a greater extent during respiration due to its proximity to the diaphragm. On the other hand, the upper part of the heart experiences less motion since it is restricted in motion by the aorta and pulmonary artery. This difference in motion has a substantial effect on the value of the correction factor and subsequently, on the image quality of the coronary MR scans. This is theorized to be more apparent since current navigator techniques use the fixed correction factor of 0.6 or in the case of subject-specific rigid motion correction, only the correction factor for the lower heart.

We tracked both the upper and the lower heart motion with respect to the diaphragm movement in cine scans and computed for the SI correction factor of each. To account for both motion using a single correction factor, we got the average of the two correction factors. This means the SI correction allows for motion correction without overemphasizing the motion artifact in either upper or lower heart.

The second part of chapter 3 also elaborates the estimation of the affine motion parameters from the tracked diaphragm and five regions of interests in the

heart. From this affine parameters, another SI motion correction factor was also computed and this, together with the rigid body correction factor and mean SI correction factor were used in the respiratory gating simulation conducted in the next chapter.

Chapter 4 presents the main part of the paper, which is the simulation platform for evaluating respiratory motion compensation techniques without undergoing an actual scan. Here, we proposed an approach for simulating prospective respiratory gating. Since it is impossible to get the effect of a respiratory gating alone on the scan, a simulation can be an ideal option to compare these techniques. An actual scan will have different contributing factors to image quality, like differences between MRI scanners, motion of the four chambers of the heart during cardiac cycle, and magnetic inhomogeneities in the machine. The simulation model provides a platform to get the image artifact contribution of respiratory gating alone on the scan. This allows for the comparison of different techniques and different motion correction factors without the motion effects from other variables.

Additionally, the possible quantitative assessment measures of different coronary MR angiography scans were demonstrated. A combination of six image quality measures was used to assess the image quality of the resulting scan, whether actual or simulated. The combined assessment of coronary MRA includes absolute image difference, peak signal-to-noise ratio (PSNR), signal-to-noise ratio (SNR) contrast-to-noise ratio (CNR), vessel length and vessel-edge definition. In contrast to subjective evaluation of images by reviewers, the objective analysis allows for specific evaluation of respiratory gating techniques in terms of different imaging parameters. The method to get the optimal subject-specific motion correction factor from the different motion models was presented in the last part of the chapter. The resulting correction parameter that gives the highest image quality in the simulation may be used for a subject-specific respiratory motion correction in the actual CMRA scan.

In chapter 5, we discuss an intensity standardization method to be used in standardizing the intensity levels of different cine scans to facilitate more accurate detection of edges in the ROI. Joint histogram registration was done for the cine scan of all subjects to achieve more uniform gray level intensity of tissues like

the epicardium and endocardium. This allows for more accurate tracking of the diaphragm and heart wall since the intensity level is the same for every subject. The last chapter gives out the conclusions and recommendation for future work.

# Chapter 2

# Literature Review: Magnetic Resonance Imaging of the Heart and Coronary Arteries

This chapter outlines the background to the main fields involved in the rest of the thesis. Section 2.1 is dedicated to discussing cardiac and coronary morphology. Section 2.2 is about coronary artery disease and the importance of non-invasive screening tools for its detection. An overview of the imaging modalities used in the diagnostics of coronary artery disease is discussed in Section 2.3 while 2.4 introduces CMRA and the basic MRI image acquisition. The issues related to respiratory motion and its effects on coronary MR angiography are presented in Section 2.5. Finally, the large body of work in relation to respiratory motion correction methods and a discussion on how these studies relate to this research are summarized in Section 2.6.

## 2.1. Cardiac and Coronary Artery Morphology

The human heart is a four chamber pump that circulates blood via the time coordinated contraction of each chamber. Each side consists of an atrium and a ventricle. The atrium is the receiving area that pumps blood into the ventricle, the discharging chamber. The blood vessels that supply oxygenated blood to the heart and allow it to function are the coronary arteries. There are two main

coronary arteries - the left and the right coronary arteries. The right coronary artery supplies blood to the right atrium, while the left supplies the left atrium. Both vessels deliver blood to the ventricles and the partition between chambers.

The left main coronary artery (LM) originates from the posterior aortic sinus and branches into the left anterior descending coronary artery (LAD) and left circumflex coronary artery (LCX). The LAD courses in the anterior wall of the left ventricle and is divided into proximal, mid and distal segments. The LCX runs in the left atrium and gives origin to marginal branches. The right coronary artery (RCA) originates from the right coronary originates from the anterior aortic sinus and is divided in proximal, mid and distal segments (Fig. 2.1).

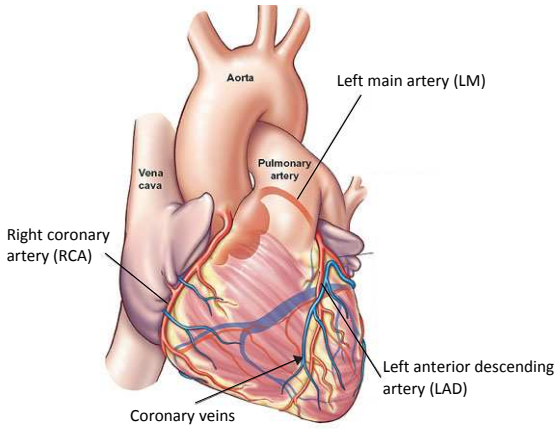


Figure 2.1: A view of the coronary artery system. The arteries supplying the posterior part of the heart are shown in a lighter shade.

## 2.2. Coronary Artery Disease

Coronary artery disease (CAD) is a pathology characterized by the buildup of plaques inside the arteries that supply blood to the heart (Fig. 2.2). This disease, also called atherosclerosis, develops through a gradual deposition of lipids, macrophages, lymphocytes and proliferation of smooth muscle cells in the artery walls [15]. Plaques may occupy nearly 40% of the internal elastic lamina of a coronary artery before the lumen begins to narrow [16]. Decreased blood flow and oxygenation to the heart muscles may go unnoticed for years, or may present

clinically as angina or chest pain in some severe cases. Advanced plaques often have a heterogeneous composition, containing extensive regions of fibrous tissue, calcium, and intraplaque hemorrhage [17]. The varying proportions of these components in different plaques gives rise to a spectrum of lesions from "low-risk" to "high-risk" (or vulnerable) plaques. Vulnerable plaques can undergo acute changes, including the rapture of the plaque's thin fibrous cap, causing a thrombosis-mediated stenosis of the lumen, occluding the artery and resulting to heart attack [18]. However, only 20% of coronary attacks are preceded by long standing angina [19].

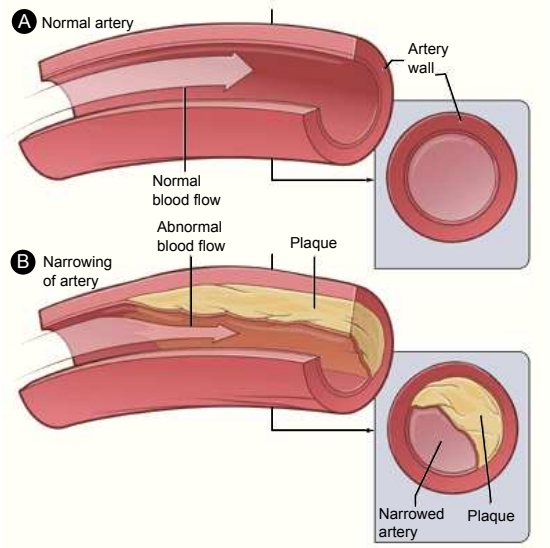


Figure 2.2: The cause of coronary artery disease. (A) shows a normal artery with normal blood flow while (B) shows an artery with plaque buildup. The inserts show the cross-section of the artery (US National Institute of Health).

CAD is the single largest killer in the world. A study made by the World Health Organization [20] in 2004 showed that the disease is responsible for approximately 7.2 million deaths worldwide every year (Fig. 2.3). This figure is around 12.2% of the total deaths and especially higher in percentage for the most developed countries (16.3%). The development of non-invasive screening tool for CAD could be valuable in characterizing atherosclerotic plaque *in vivo*. Biochemical characterization and earlier detection of unstable plaques could initiate the delivery of stabilization therapy to reduce future acute coronary events [21].

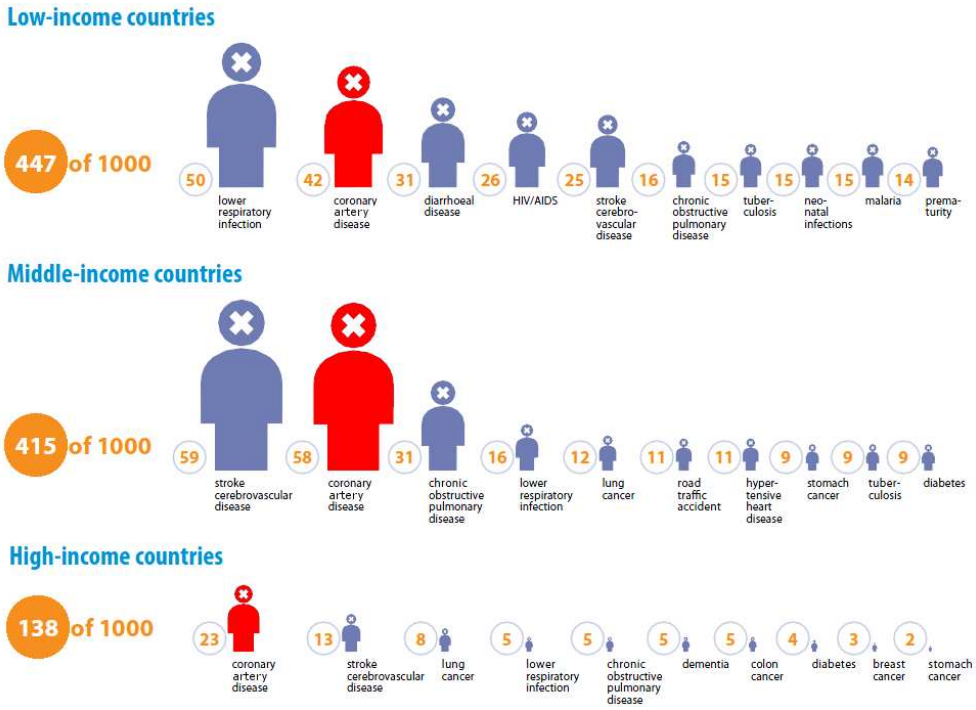


Figure 2.3: The graph illustrates the top 10 causes of death for low-, middle-, and high-income countries (World Health Organization).

## 2.3. Imaging of Coronary Arteries

There are different modalities being used to image the coronary artery tree and screen for atherosclerotic disease. These include XA, intravascular ultrasound (IVUS), angioscopy, and ultrafast CT. Coronary XA is the clinical gold standard for defining coronary anatomy and degree of lumenal obstruction of the coronary arteries [22]. The procedure involves the injection of a contrast medium into the atrial muscle, ventricles or vessels of the heart by means of a cardiac catheter. After introducing the medium, a recording of the chambers or the vessels of the heart is made. The recording is made by using a rapid-sequence digital subtraction technique. In this technique, one image of the heart is acquired before the contrast medium is added and one after the injection of the medium. Then, the first image is subtracted from the contrast-enhanced image allowing the anatomy of the blood vessels and the blood supply of an organ to be viewed with high temporal (1530 frames/second) and high spatial (0.1 mm) resolution.

An example of coronary angiography is shown in Fig. 2.4. This procedure, however, is considered invasive and has a 0.23% risk of death, myocardial infarct, or stroke [23]. It also causes a modest amount of discomfort since a thin flexible tube called a catheter is inserted into the artery, usually though the groin. The use of contrast agents may also exclude certain patients from getting a scan and can cause serious side effects such as cardiac arrhythmia. Because XA images the coronary lumen, only advanced plaques which affect the lumen diameter are detectable. In certain cases though, a substantial minority of patients referred for diagnostic x-ray angiography are found to be without clinically significant coronary stenoses (defined as a luminal diameter reduction of at least 50% [24]), highlighting the need for better and non-invasive alternatives.

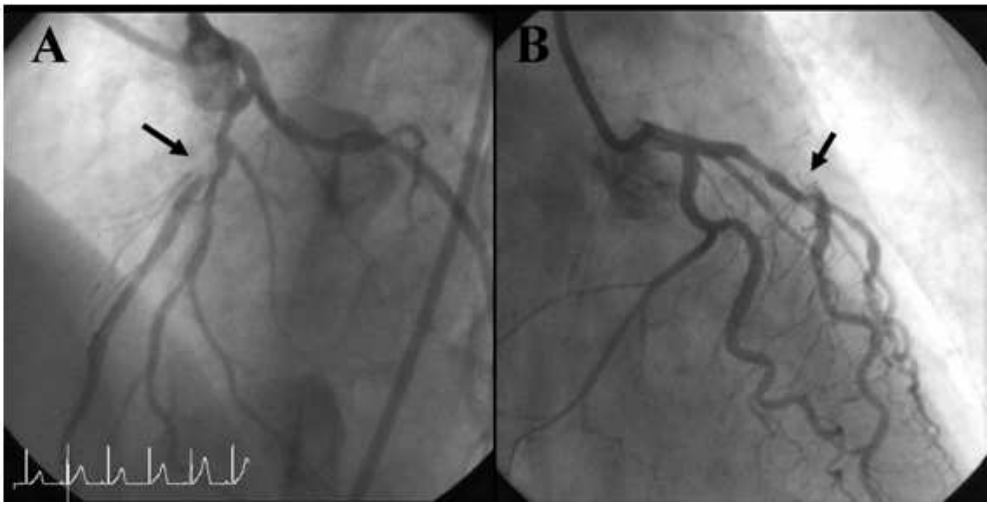


Figure 2.4: An coronary X-ray angiography of a patient with significant coronary occlusion. (A, B) The coronary angiography showed significant stenosis in mid-LAD (Image from [1]).

IVUS is a new approach for visualizing the artery wall with resolution between 100-250 m using a catheter-based probe with a miniature ultrasound transducer. Nissen et al. [25] demonstrated the ability to categorize plaques into calcified tissue, fibrosis, or thrombotic tissue. Invasive optical visualization of the arterial wall using fiber optic angioscope to see the artery lumen is called angioscopy. Uchida et al [26] demonstrated a correlation between the color and glistening characteristics of plaques, and the occurrence of acute coronary syndromes in a

12-month follow-up period. These procedures, however, are more invasive than XA, in that the catheter must be advanced to the site of plaques. Moreover, IVUS can cause transient coronary spasms for some patients [27] and coronary blood flow must be interrupted for angioscopy.

Multidetector CT (MDCT) is a relatively new imaging technology and has spurred interest in CT coronary angiography. A new generation of scanner with 64 detector channels (64 MDCT) is now available with a 330  350 ms gantry rotation time, which means improved temporal (42 - 82.5 ms) and spatial (0.4 mm) resolution , achieving near isotropic imaging and faster scan times [28, 29]. Increasing the temporal resolution to reduce motion artifacts requires longer scan times, which will necessitate improved respiratory motion gating and correction methods. A clinical study of 230 patients concluded that the sensitivity and specificity of MDCT angiography for detecting focal coronary stenoses (occlusion = 70%) were 83% and 83%, respectively [30]. These systems also have the ability to quantify the amount of calcium, but the usefulness of this measurement is still being debated [31, 32]. Ultimately, coronary imaging with MSCT exposes the patient to contrast and x-ray radiation. Administration of $\beta$ blockers or other negative chronotropic drugs may be required to stabilize and reduce the heart rate for reduction of motion artifacts [33].

## 2.4. Coronary Magnetic Resonance Angiography

Coronary magnetic resonance angiography allows for the noninvasive visualization of the major epicardial coronary arteries. In recent years, it has undergone technological advances that lead to enhanced spatial resolution and the possibility of imaging while the patient is breathing freely. The main advantage of this technique is the lack of exposure to ionizing radiation or ionated contrast media. In addition, the high tissue contrasts of the images allow for the detection and quantification of plaques and fats in the coronary vessels and can be used with other MR protocols to assess blood flow and viability [5, 6]. Figure 2.6 shows the images of the heart and coronary arteries using CMRA. The images taken are that of a normal heart, thus, no plaques are visible.

### 2.4.1 MRI Image Acquisition

An MRI scan works by using a powerful magnet, radio waves and a computer to create detailed images. The acquisition of MR images such as that of coronary arteries in CMRA can be generally divided into the following steps:

1. Put the subject in a strong magnetic field.
2. Transmit radio frequency (RF) waves into the subject.
3. Receive the echo RF waves from the subject.
4. Store the measured RF waves and repeat from Step 2 until enough data are gathered.
5. Process raw data to reconstruct images.

The body is made up of millions of hydrogen atoms due to its water composition. These hydrogen atoms are magnetic, thus, when the body is placed in a strong magnetic field (Step 1), they align with the field. An RF wave "knocks down" the atoms and disrupts their polarity. The sensor detects the RF wave echo and measures the it takes for the atoms to return to their original alignment.

In order to spatially encode the measured signals coming from the subject, magnetic field gradients are applied. These gradients, namely, frequency encode, phase encode and slice select, are spatially varying magnetic fields so that the atoms at different locations precess at frequencies unique to their location. These allow for the reconstruction of 2D or 3D images. Figure 2.5 shows a representation of these gradients.

### 2.4.2 Motion during CMRA Image Acquisition

Despite major advances in magnetic resonance angiography and its emergence as the main replacement for X-ray angiography, it is still an area of active research [34, 35, 36]. Improved visualization of the lumen and arterial wall, with a reduction of flow artifacts, was demonstrated with black blood imaging techniques. Fayad et al. [37] measured a difference in coronary wall thickness between volunteers ($0.75 \pm 0.17$ mm) and CAD patients ($4.38 \pm 0.71$ mm) with breath-hold

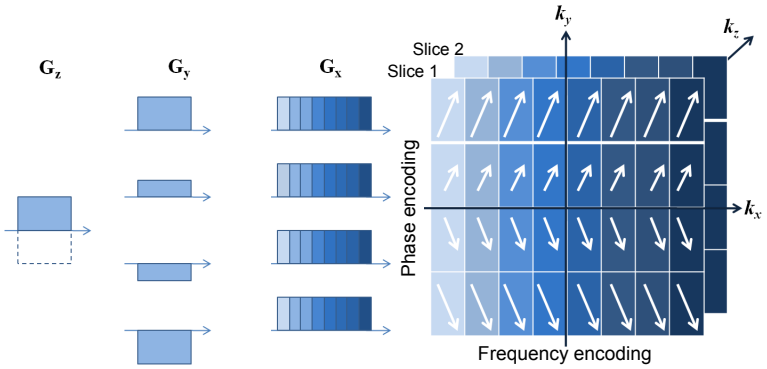


Figure 2.5: To create the actual MR image, the received signals are encoded into the three Cartesian coordinate directions. For an axial image, the frequency encoding gradient, phase encoding gradient and slice select gradient are in the $x$-, $y$-, and $z$-direction, respectively.

2D black blood, fat saturated images transverse to the axis of the right coronary artery (RCA) and left anterior descending (LAD). Stuber et al. [38] combined black blood imaging with navigator echoes, which are fast 1D images used to measure the motion of internal organs, to acquire images during free breathing. The superior-inferior motion of the diaphragm, as measured by the navigator echo, is used to translate the position of the imaging frame during the acquisition. Using this technique, Botnar et al. [39] demonstrated increased vessel wall thickness ($1.5 \pm 0.2$ versus $1.0 \pm 0.2$ mm) and reduced lumen area ($7.0 \pm 2.3$ mm$^2$ versus $9.3 \pm 1.9$ mm$^2$) in the proximal RCA of patients with known CAD.

The major challenges for MRCA includes spatial resolution and coverage, cardiac and respiratory motion, and signal-to-noise limitations. These shortcomings were addressed by the use of nearly isotropic fast three-dimensional (3D) techniques. Some of the advantages of 3D imaging techniques are the acquisition of thinner slices, superior signal-to-noise ratio (SNR) and the complete coverage of the coronary artery tree [40, 41]. However, image quality has been hampered by motion related artifacts and has not reached sufficient quality for widespread diagnostic application yet. Better motion compensation is needed to further increase image resolution and SNR, and in turn make MRCA a more reliable clinical modality.

The motion that affects the heart during CMRA scan is a vector sum of three

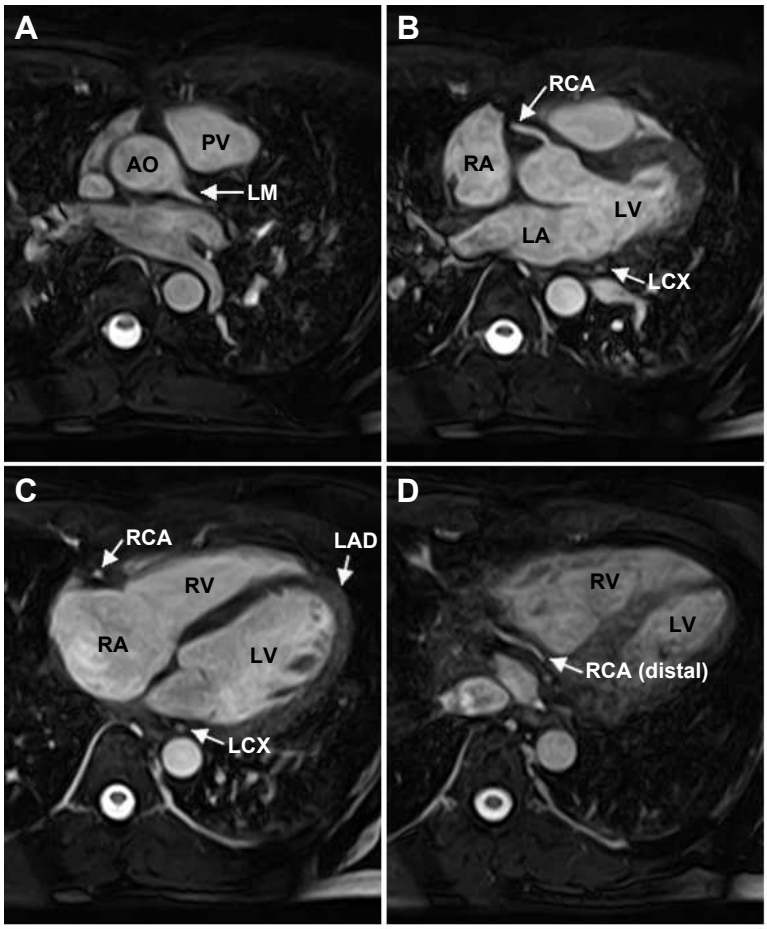


Figure 2.6: Anatomical images of the heart and coronaries arteries gathered using coronary magnetic resonance angiography. The images are the coronal slice of the heart from the base of the aorta (A) to the lower part of the heart (D); AO, aorta; PV, pulmonary vein; RA, right atrium; RV, right ventricle; LA, left atrium; LV, left ventricle; LM, left main artery; RCA, right coronary artery; LCX, left circumflex artery; LAD, left anterior descending artery.

components: motion of the pumping of the four chambers during cardiac cycle, motion caused by respiration, and motion resulting from voluntary or involuntary patient movement. The latter component is managed by patient cooperation or by sedation or anesthesia in pediatric and other difficult cases. Cardiac-induced motion is commonly addressed using cardiac triggering using electrocardiogram (ECG/EKG). The goal is to acquire coronary MR images during the period of

the cardiac cycle when the arteries are relatively stationary. This stationary or rest period has been established as approximately 750 ms after the R wave of the ECG [42].

## 2.5. Respiratory Motion

The main driver in respiratory motion is the movement of the diaphragm, a large musculomembranous dome that separates the thorax and the abdomen. It contracts during inhalation, letting air enter the lungs and then relaxes during exhalation allowing air to get out. The diaphragm is fixed to the surrounding structures, including the ribs and the lumbar verterbrae, where its motion is limited. The superior-inferior (SI) or cranio-caudal translation of the diaphragm ranges from 10-20 mm for normal respiration but more than that when measured during deep breathing or breath-holding [14, 43]. The other process causing an increase in lung volume is the motion of the chest wall. The rib cage moves diagonally upwards, allowing the lungs to expand [44] and increasing air volume. Its contribution in the lung volume increase is significant although less than that of the diaphragm contraction [45].

One complete respiratory cycle is typically around 5 seconds [46], although it varies across the population and depends on exercise levels. The respiratory cycle consists of two phases – inspiration and expiration (Fig. 2.7). During inspiration, the diaphragm contracts and allows the thoracic cavity to increase in volume and inflate the lungs. In expiration, the diaphragm relaxes, curving up towards the lungs and decreasing its volume. The form of the cycle approximates a sine wave but has a portion which experiences minimal motion, often observed around end-exhalation. In addition, variations in both the depth of respiration and period of respiratory cycle are frequently observed [47] even during the relevant timeframe for clinical imaging. These variations result in complex respiratory-induced motion of organs like the heart and liver, which are continually changing in amplitude, and possibly direction over time.

During the respiratory cycle, the amount of air that enters or exits the lungs is called tidal volume, which averages around 0.5 liters (L). The additional amount of air that can be forcefully inhaled beyond tidal inspiration is called inspiratory

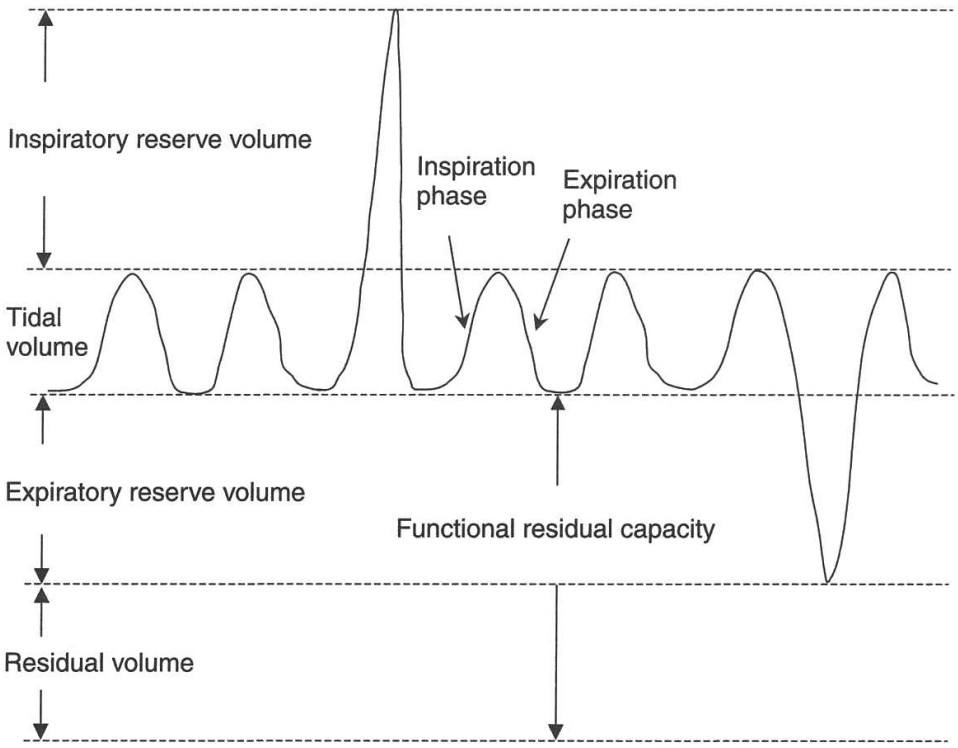


Figure 2.7: A schematic plot of respiratory waveform showing inspiration and expiration. Top portions correspond to end-expiration, where the relatively flat area is the functional residual capacity (Bernstein2004, 475).

reserve volume ($\approx$ 3.1 L). Correspondingly, the extra amount of air that can be maximally exhaled after tidal expiration is called the expiratory reserve volume ($\approx$ 1.2 L). Even at the maximal expiration, there is residual air in the lungs, referred to as residual volume ($\approx$ 1.2 L). The combination of the reserve and residual volume constitutes the functional residual capacity or FRC ($\approx$ 2.4 L). As described later in this section, respiratory gating typically occurs when the lung volume corresponds to FRC [48].

### 2.5.1 Respiratory Motion of the Heart

The contraction and relaxation of the diaphragm during respiration not only affects the lung volume but also moves the heart, where the motion is mainly in the SI direction. During inspiration, the diaphragm presses the liver downward

and the heart, which generally lies over the diaphragm, moves in the inferior direction. This motion is influenced by the physiology of the heart in which the lower part of the heart pericardium is attached to the diaphragm [49]. Every time the diaphragm moves in the inferior direction during inspiration, it pulls the pericardium along with the heart. In turn, the diaphragm pushes the heart upwards in the superior direction during expiration. While the displacement of the lower heart is influenced by the diaphragm motion, the movement of the upper heart is comparatively restricted since it is attached to the aorta and the major pulmonary veins. This, along with the fact that the pericardium surrounding the heart is also attached to the posterior part of the sternum, limits the heart movement.

Furthermore, the motion of the heart is influenced by that of the chest wall, though to a lesser extent than that of the diaphragm. Due to the expansion of the chest wall during inhalation, the heart moves in the anterior direction [50]. The superior-inferior motion of the diaphragm and the anterior-posterior (AP) motion of the chest wall makes up the respiratory motion of the heart. The SI translation is the most dominant component of motion, with a small translations in the anterior-posterior and right-left directions as well as rotations, which vary in amplitude and direction [51, 50].

The relationship between the motion of the heart and the superior-inferior motion of the diaphragm is approximately linear [14, 52] but highly subject-specific [53]. This may account for the inconsistencies in average correction factors ($CF$) between studies (Table 2.1). The correction factor is a one-dimensional motion coefficient that relates the one-dimensional (SI direction) motion of the heart with respect to the diaphragm. This multiplier is used in most MR scanners to correct for respiratory motion. It has a set value of 0.6 in most scanners, which indicates that for every 1 mm motion SI motion of the diaphragm the heart moves 0.6 mm in the same direction.

The standard $CF$ value was based mostly on the studies made by Danias et al [43], who found a mean heart to liver motion ratio of 0.6 (range 0.17 to 0.93 over 12 patients). Other studies also recorded different values like McLeish et al. [13], who recorded a mean value of 0.45 (0.28 to 0.73 over 8 volunteers and 8 patients). Table 2.1 shows the results from some of these studies.

Table 2.1: Correction factors relating the SI motion of the heart and the diaphragm

| **Study** | **Correction Factor** | | | **Tracked Location** |
|---|---|---|---|---|
| | SI | AP | RL | |
| Wang et al [14] | 0.57 | 0.09 | NR | RCA Root |
| | 0.70 | 0.85 | NR | Proximal LAD |
| | 0.81 | 0.07 | NR | Apex |
| Danias et al [43] | 0.60 | NR | NR | Left MCA |
| Taylor et al [53] | 0.49 | NR | NR | Proximal RCA |
| | 0.59 | NR | NR | Proximal LCA |
| Nagel et al | 0.62 | NR | NR | Inferior LV wall |
| | 0.27 | NR | NR | LCA |
| Keegan et al [51] | 0.25 | 0.04 | 0.12 | RCA Root |
| Fischer et al | 0.38 | NR | NR | Proximal RCA |
| | 0.59 | NR | NR | Distal RCA |
| Jahnke et al | 0.45 | 0.01 | 0.02 | Whole heart |

The respiratory motion of the heart has been found to be approximately rigid-body in nature [54, 55]; it experiences translations and rotations with little deformation. Nonrigid motion has been observed in more recent studies. McLeish et al [13] measured deformations of 3 - 4 mm in the left ventricle wall when imaging using 3D MR scans at multiple breath-hold positions. These deformations though may vary between patients and would be less pronounced during free breathing. This results to a heart shape that slightly varies over the respiratory cycle. Taylor et al [56] also recorded the end-inspiratory and end-expiratory dwell times during free breathing as 0.4 $\pm$ 0.2 s and 1.1 $\pm$ 1.6 s, respectively, with a respiratory period of 4.3 $\pm$ 1.1 s, and diaphragmatic amplitudes of 14.1 $\pm$ 4.8 mm. The brief pause after the expiration, before the next cycle begins, is the typical period covered by the respiratory gating window during cardiac imaging.

### 2.5.2 Effects of Respiratory during CMRA Imaging

The occurrences of respiratory motion during a CMRA scan is unavoidable due to the relatively long duration of free-breathing scans (5 - 10 minutes). The effects of motion during a MRCA are two-fold. Firstly, motion artifacts introduced during the scan will result in a blurring of the image(Fig. 2.8B). As the length of the length of the scan increases, so is the possibility that respiratory motion affects the image quality and causes noticeable image degradation.

Blurring due to motion artifacts can make it difficult to interpret coronary MR scans. Differentiation between arteries and veins can be problematic, especially between the left anterior descending (LAD) and left circumflex artery (LCX) from the great vein in the distal segments [57]. The pericardial sac can appear as a linear structure with medium to high signal intensity similar to a coronary artery. Furthermore, fluid in the superior pericardial recess, may show as a coronary artery-like structure, making it appear as a continuation of the vessel itself.

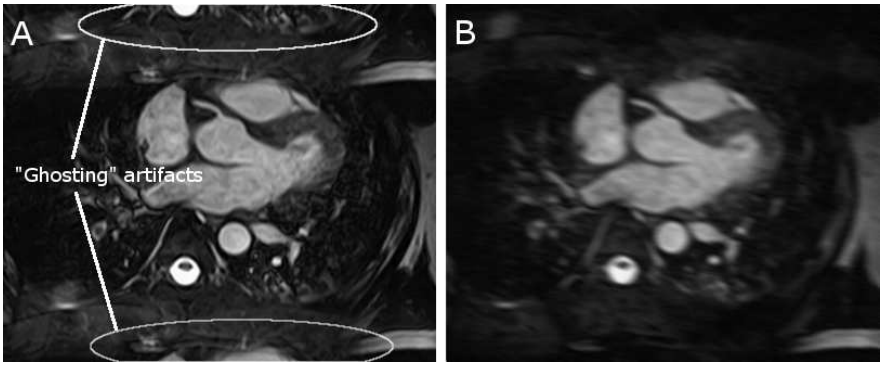


Figure 2.8: Axial steady state free precession (SSFP) images with ghosting (A) and blurring (B) artifacts due to respiratory motion.

Aside from blurring, the periodic movement of the heart during data acquisition can cause ghosting in the phase-encoding direction [58]. Ghost-like replicas of the moving structure are super-imposed on other structures, obscuring those structures (Fig. 2.8A). There is a constant spacing in pixels between consecutive ghosts, which is equal to the number of cycles of motion that occurred during the acquisition of data. The intensity of ghosts depends on the intensity of the moving structure and the number of pixels over which the motion occurred [59].

## 2.6. Respiratory Motion Correction

During the acquisition of MR images, a Fourier space or $k$-space is filled and then Fourier transformed to create the image. Since each part of the $k$-space contributes to the image reconstruction, any inconsistencies between (inter-view), or within (intra-view) $k$-space lines can lead to blurring and ghosting artifacts [60, 61]. Fast hardware has provided short read-out times, thus leaving the inter-view motion as the most common source of motion artifacts. Respiratory motion can be corrected retrospectively as post-processing of image data or prospectively during the data acquisition. Retrospective correction in $k$-space requires high computational cost due to data void and overlapped regions in $k$-space. Thus prospective motion correction can be deemed to be simpler and faster.

### 2.6.1 Respiratory Gating in CMRA

A variety of approaches have been implemented to reduce respiratory motion artifacts like $k$-space reordering [62], signal averaging [60], and gating [63]. $K$-space reordering technique relies on the fact that movement during the acquisition of the outer $k$-space lines has less adverse effects on image quality compared to the same movement during the acquisition of the central lines. Most methods using $k$-space reordering acquire the central region during end-expiration, when the movement of the diaphragm is minimal [64, 65]. Signal averaging is the use of multiple image acquisitions to improve the signal-to-noise ratio (SNR) of the image. The number of averages is also referred to as the number of excitations (NEX), and doubling the number of excitations will increase the SNR by the 2. Gating can provide the best image quality and contrast, at the expense of longer imaging times. Data is acquired during short temporal window in which the object is assumed to be motionless. This method allows data for an image to be acquired at the same motion phase during multiple cycles of respiration. In general, to get a desired image resolution and contrast, one must balance the inversely related temporal width and data acquisition window.

Nevertheless, navigator gating in the SI direction is one of the most commonly used motion correction technique in CMRA protocols. The method utilizes a fixed correction factor between the diaphragm and cardiac motion [14] in tandem

with a small gating window of 5 mm [10] to correct for respiratory motion of the heart. Several techniques improve respiratory efficiency by correcting motion using a larger acquisition or gating window. The retrospective technique suggested by Ehman and Felmlee [63] applies a phase shift to the measured data that is dependent on the navigator-measure diaphragm position. A more recent study by Wang and Ehman [66] use a similar retrospective technique with linear interpolation of the respiratory signal between and pre- and post-imaging segment navigators to correct 3D coronary image data.

These motion correction methods consider the motion of the heart during respiration as rigid body motion. However, physiologic motion of the heart can rarely be described by rigid body transformation. Haacke and Patrick described the effect of spatial scaling on $k$-space, and proposed a linear expansion correction method [64]. They demonstrated improvement of abdominal imaging during free breathing by monitoring the movement of the abdominal wall, and by changing the imaging gradients prospectively to compensate for anterior-posterior expansion and compression of the abdomen. Atalar and Onural extended this concept, and presented a retrospective correction method for removing artifacts caused by 2D in-plane translation and scaling [67].

Motion correction methods with more degrees of freedom need to be explored. By increasing the amount of motion that can be corrected, the imaging duty cycle can be increased and total scan time reduced. There is also the difference in respiratory motion between subjects or patients. Correcting individually for subjects can increase the efficiency of the respiratory gating.

### 2.6.2 Summary

With regards to prospective motion correction, one major task is to find the appropriate correction that is able to describe the respiratory motion sufficiently. That motion model should consider not only the motion during the respiratory cycle but the subject-specific variabilities as well. This study is meant to evaluate the capability of different motion models to describe the respiratory-induced motion of the heart and coronary arteries. This was done using a platform that simulates respiratory motion of the heart and motion correction and described in the succeeding chapters.

# Chapter 3

# Subject-Specific Respiratory Motion Gating

Respiratory motion is one of the major limiting factors in coronary MR imaging and may cause image degradation if motion correction is omitted. Cardiac structures like the coronary arteries undergo complex motion induced by respiration. And this motion during MR scan affects the resulting image quality by introducing ghosting artifacts, blur and reducing image contrast.

There are several types of motion that corrupt coronary MR images. For most pulse sequences, the prospective rigid body motion is assumed and can be subdivided into inter-view motion (through-plane translation), intra-view motion (in-plane translation) and rotation. Correction of intra-view translation is achieved by updating the measurement frequency and phase offset for each profile, while inter-view translation is corrected by updating the transmit radio frequency (RF) [68]. Rotational motion can be corrected by rotating the gradient matrix [69].

However, studies have shown that the motion of the heart during respiration is nonrigid and there is variability in respiratory motion cycles within and across patients, making it difficult to measure and predict the motion of cardiac structures. The respiratory motion of the heart contains not only motion in the SI direction but in the RL and AP directions as well. These can be described by an appropriate motion model but the variability between patients may mean different suitable models for each patient. This chapter relates the variability of

motion that affects respiratory gating and evaluates a number of motion models to address this problem.

The first section shows a brief overview of the basics of the navigator technique and prospective gating used in MR imaging. It also elaborates the imaging parameters of the scout scans. The second section reviews the motion models used to correct for respiratory motion of the heart. This includes the rigid body translation model, nonrigid motion with translation and scaling and the affine transformation model. The later parts give the evaluation results and discuss its implications in the subject-specific navigator guided respiratory gating.

## 3.1. Prospective Navigator-guided Gating

Early cardiovascular MR examinations used breath holding for respiratory motion compensation. The first scanner technologies and designs allowed studies to be completed within a single breath hold [70]. The breath is usually suspended at end-expiration, which is more stable and reproducible and blood flow is more similar to that during free breathing [71]. However, studies with sufficient signal-to-noise ratio (SNR) cannot be completed within the short comfortable period of 20-30 seconds for healthy volunteers and with an even shorter time for patients. Multiple breath-holds can be used [72] and acquire parts of the $k$-space in each breath-hold but poor breath-hold reproducibility may lead to misregistration artifacts. In addition, all breath-holding techniques require patient cooperation, which can be problematic and may allow image degradation due to respiratory drift during the respiratory period [73].

In order to allow respiratory motion correction during free breathing for patients, various methods for monitoring respiration have been suggested along with the ways of gating, triggering, or compensating for the detected motion. Systems for monitoring chest wall movement including belts [74], bellows [14], or optical compression devices [75] were used. There are also methods to measure inhaled and exhaled air volume like capnography or nasal cannulas [74]. These methods though, have their own limitations specifically with respect to low patient tolerance and the different assumptions made about the relationship between the output signal and the motion of the heart. To overcome most of these limitations,

methods to monitor the diaphragm were suggested to allow respiratory motion correction without breath-holding and intrusive external monitoring devices. One of these methods uses navigators to monitor the diaphragm motion. The next section discusses the navigator gating and how it is currently used for prospective motion correction during cardiac MR.

### 3.1.1 Navigators

Methods in which MR data are used to monitor the diaphragm (or a section of the heart) in order to correct for motion are generally known as navigator techniques. The most common forms involve a column of tissue excited by a section-selective 90 RF pulse followed by a non-coplanar 180 pulse (Ehman, Rad1989). The position of the diaphragm, clearly delineated by the liver-lung interface on the right hemidiaphragm can be extracted from the reconstructed navigator profiles.

A navigator acquires a partial set of *k*-space data that is processed to track one or more effects of patient motion. In the case of coronary MR imaging, the method is used to determine the diaphragm or heart position. The navigator echoes are interleaved within the normal acquisition of the image data. A key assumption is that the motion that transpires between the navigator and acquired views is negligible.

The navigator data are used either retrospectively or prospectively. Retrospective navigator data are used to correct the image or raw data after the scan is completed. Retrospective motion correction in *k*–space is not straightforward and requires high computational cost due to data void and overlapped regions in *k*-space. On the other hand, in prospective correction, the navigator data are employed to modify the subsequent imaging acquisition to prevent artifacts. In prospective motion correction, the navigator may be used to perform section tracking to further improve image quality in the respiratory gating window [68]. This study is focused on prospective motion correction so techniques on retrospective motion correction will not be discussed further.

Navigators can use 1D, 2D, or 3D *k*-space trajectories (Fig. 3.1). The simplest navigator is a 1D or linear navigator, which gets one line of data passing through the origin of *k*-space, usually along the $k_x$, $k_y$, $k_z$ axis. For respiratory motion correction, the navigator is placed along the coronal view to track the diaphragm

motion. The Fourier transformation of the navigator data is a projection orthogonal to the navigator readout gradient direction. A linear navigator allows object translation in the navigator readout direction to be monitored during scan.

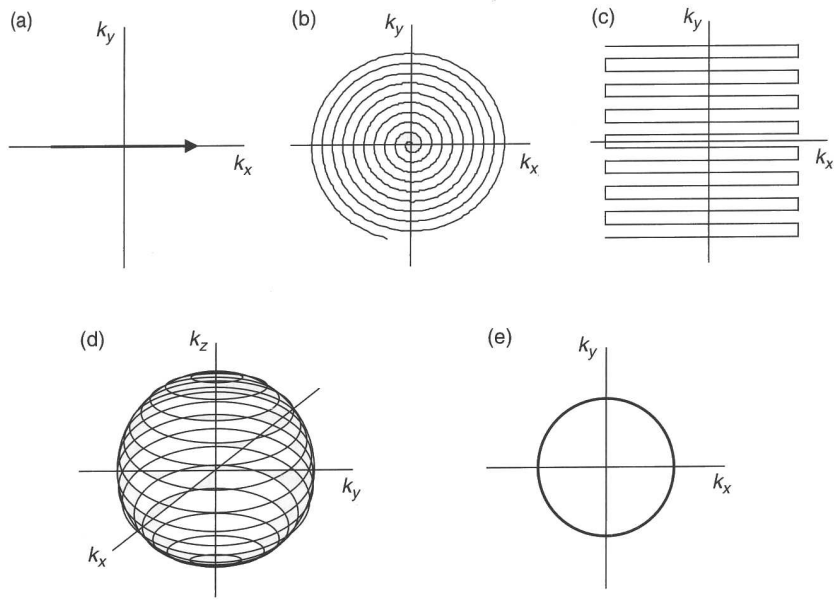


Figure 3.1: $k$-space trajectories for (a) linear, (b) 2D spiral, (c) 2D EPI, (d) 3D spherical, and (e) 2D orbital navigators.

There are several ways to process a linear navigator data to determine the object translation. The most common methods are correlation and least-squares fitting. In the correlation method, the object displacement $d$ is computed by maximizing

$$c(d) = \sum_j |P_n(x_j - d)||P_r(x_j)|, \tag{3.1}$$

where $P_n(x_j)$ is the complex navigator projection (Fourier transform of the navigator raw data) for the current view and $P_r(x_j)$ is the projection of a reference navigator, usually acquired at the beginning of the scan. The sum is the taken over a subset of the projection containing the highest desired edges (i.e. the diaphragm).

In the least-squares method the estimated object displacement $d$ minimizes

$$l(d) = \sum_j (|P_n(x_j - d)| - |P_r(x_j)|)^2, \tag{3.2}$$

where the sum is taken over an appropriate subset of the projection again. Least-squares fitting is preferable if the navigator SNR is low [76] due to short TR for example.

The navigator RF excitation is usually spatially selective and can be read out using a gradient or spin echo. In many cases however, the transverse magnetization excited by the imaging RF pulse is used instead of a separate RF excitation.

Calculations in prospective navigators can lead to delays of subsequent data acquisition. The complexity of the calculations increases as 2D and 3D $k$-space navigator trajectories are used. This and with the adverse effects on image quality of areas near the navigator pulses, makes the 1D navigator as an ideal choice for cardiac imaging.

### 3.1.2 Prospective Gating

In prospective motion correction, the navigator is used so that the scan volume is fixed with respect to the magnet and it gates the acquisition to achieve consistent anatomical location with respect to the scan volume. In contrast to retrospective gating, where correction is made after the scan is already completed, prospective respiratory gating monitors and corrects the monitored motion while the image or volume data is being acquired.

For cardiac imaging, diaphragm location data can be used prospectively in several ways. The simplest is to acquire data only when the respiratory phase is within the predefined gating or acceptance window. A window location near the end-expiration phase is usually chosen because it is held longer and found to be the most linear with respect to heart motion over time than other phases. The acceptance window width, which is typically 2-5 mm, and window location are determined from navigator data acquired over a period of free-breathing prior to the gated scan. An acceptance window that is too wide results to image degradation. On the other hand, a smaller acceptance window gives better image quality but scan efficiency is reduce, resulting to longer scan times. It is assumed that during respiration, the anatomy moves smoothly and periodically through the scan volume. Here slice tracking is used with periodic motion and moves the scan volume to lie at approximately the same location with respect to the patient anatomy on each acquisition.

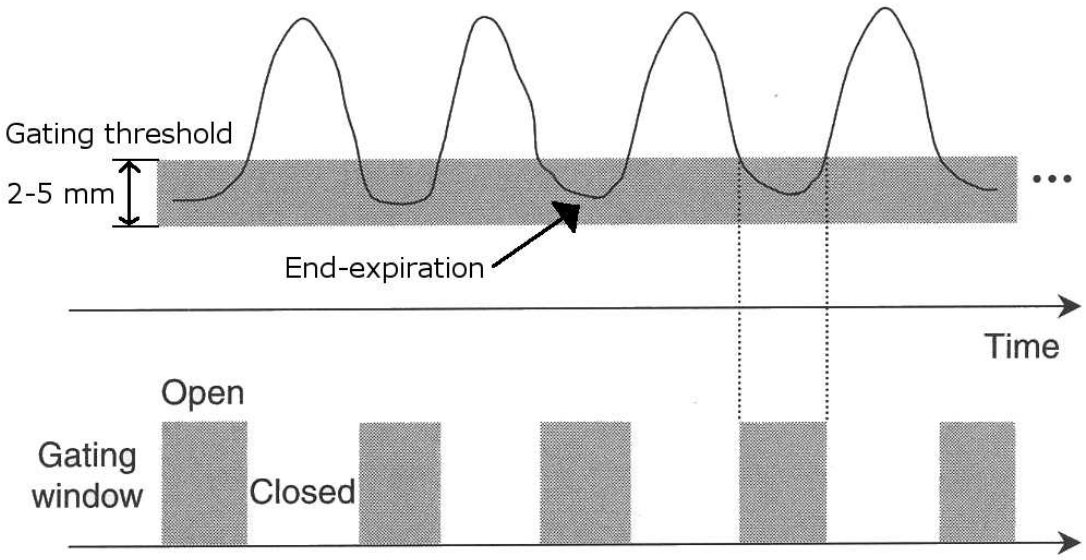


Figure 3.2: Respiratory motion correction using a gating window. The diagrams show the selection of gating open/close points. The distance between the upper and lower threshold determines the size of the gating window, which is around 2-5 mm in cardiac MR scans

To correct for cardiac respiratory motion, the data acquisition volume is moved to track the heart as it moves with the diaphragm during respiration. A key assumption is that the coronary arteries move in the SI and AP directions by roughly 60% and 20% of the diaphragm displacement, respectively [14]. RL displacement is usually negligible but can be observed in some subjects or patients. The scan volume is moved in the SI and AP direction by a fraction of the diaphragm motion referred to as the correction factor ($CF$), in this case 0.6 and 0.2, respectively. Hence, the 0.6 value has been used for 1D motion correction in the SI direction in most CMRA scans. This correction factor, however, is an oversimplifications since there is a wide variation in respiratory-induced motion between patients.

## 3.2. Motion Models in Subject-specific Respiratory Motion Correction

There are many factors to consider in respiratory motion correction during coronary MRA. When using a navigator gating method, one of the most important variable is the type of motion to consider. The standard used today in CMRA protocols is the fixed correction factor (0.6) but this does not consider subject-specific respiratory motion of the heart. And although the majority of the motion is in the SI translation, scaling, rotation, and RL and AP translation may also occur. Whatever motion model is used, the correction factor should be distinct for the subject or patient. Different motion models may also be needed for different subjects so a method to compute the correction factor for each model and compare their individual efficiency when it comes to motion correction is needed. The different motion correction factors should also be tested specifically for the individual patient or subject involved.

In this study, three methods representing different motion models were proposed to correct for subject-specific respiratory motion correction. The first model assumes rigid body motion of the heart with SI translation as the lone parameter. The second model compensates for both the translation and scaling in the SI direction. It assumes a nonrigid transformation and although only two degrees of freedom are allowed, it addresses the two main sources of motion. The last motion model involves the 2D nonrigid affine motion correction.

### 3.2.1 Rigid Body Translation

In most cases, the motion of the heart during coronary MR imaging is modeled as a rigid body motion, consisting of a translation plus rotation. According to the Fourier shift theorem, a displacement of the object by vector distance $\boldsymbol{T}$ results to a motion-corrupted raw data $S_m(k)$ given by

$$S_m(k) = S_s(k)e^{i2\pi k \cdot T}, \tag{3.3}$$

where $S_s(k)$ is the data for a stationary object. Interview translation therefore results to a $k$-space data that has a linear phase shift that is proportional to the object translation distance.

Consider a rotation whose axis passes through the center of the imaging volume. Interview rotation of the tracked region rotates the $k$-space data about the same rotation axis and by the same rotation angle as this region. In a 2D acquisition, the rotation and translation-corrupted $k$-space data $S_m(k,\theta)$ are expressed in polar coordinates by

$$S_m(k,\theta) = S_s(k,\theta-\alpha)e^{i2\pi k(x_0\cos\theta+y_0\sin\theta)}, \tag{3.4}$$

where $\alpha$ is the rotation angle and $(x_0, y_0)$ are the coordinates of any translation that might have occurred [77]. The magnitude of the $k$-space data is thus only affected by rotation, whereas the phase is affected by both rotation and translation [48].

In the case rigid body motion correction using navigator, a quick MR prepulse is applied in the moving structure of interest. This type of navigator may be placed directly on the heart, chest wall, or in most cases, the dome of the hemidiaphragm. The boundary of the diaphragm can be tracked since it is clearly delineated by the liver-lung interface on the right hemidiaphragm. It can be detected using either edge detection [78], correlation, or sum of squared distances (SSD). In this study, we used SSD to detect the liver-lung interface since it is more robust in the presence of profile deformation compared to edge detection and less computationally demanding than correlation [76].

In relating the rigid body motion of the heart with respect to the right hemidiaphragm, many early studies showed inconsistencies in the measured average SI motion correction factors [14, 53, 43, 51]. These studies also reported large standard deviations, suggesting high intersubject variability. The variability of respiratory-induced motion between subjects can be partly solved by calculating a subject-specific correction factor in the SI direction [79, 80]. This SI translation correction factor is the sole parameter used in this model.

In this study, the estimation of the SI correction factor involved tracking both the diaphragm and heart location for all scout images. The value of $CF$ was computed from motion coefficients describing the correlation between the motion of the diaphragm with each tracked part of the heart. To track the movement of the diaphragm, a rectangular region of interest (ROI) with dimensions of $30 \times 10$ pixel was placed in the dome of right hemidiaphragm (Fig. 4.2). This ROI tracked the movement of the lung-liver interface in each slice of the scout scans. Another

ROI of 25 × 10 pixel dimension was also placed in the lower part of the heart, near bottom of the right ventricle. The longer ROI for the diaphragm is due to the fact that its displacement is generally larger than that of the heart.

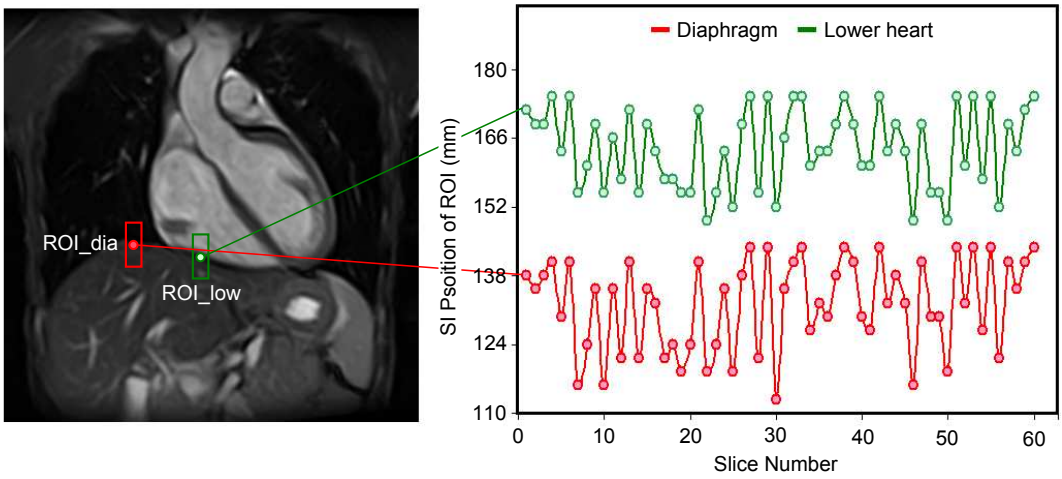


Figure 3.3: Rigid motion model ROI for diaphragm and heart. The right side shows the tracked location of the diaphragm and the heart ROI for all images in the cine scout scan.

Once the location of the diaphragm and heart in each ROI was known, a scatter plot was used to get the correlation coefficient ($CC$) between the two variables (Fig. 3.4). The horizontal axis serves as the independent variable and holds the tracked positions of the diaphragm. In the vertical axis lies the tracked locations of the heart. All 60 points represent the diaphragm and heart positions for each coronal image in the scout scan. An equation for the correlation between the two variables was determined using linear regression. The linear regression formula takes the form

$$y_{dia} = bx_{lr} + a \tag{3.5}$$

where $y_{dia}$ and $x_{lr}$ are the diaphragm and lower right heart locations, respectively. $b$ is the slope and $a$ is y-intercept of the regression line. The slope describes the rate of change in the heart location for each unit displacement of the diaphragm and designated as the SI correlation coefficient ($CC_{lr}$) of the lower right heart.

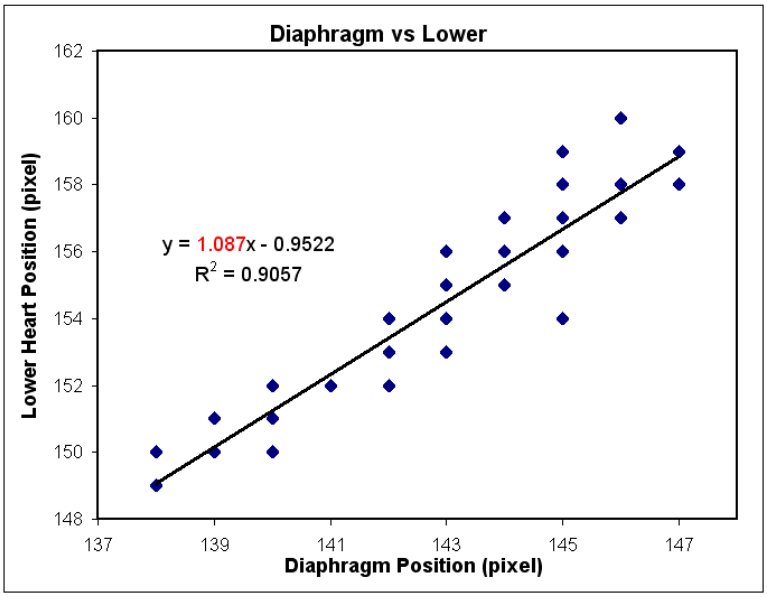


Figure 3.4: A scatter plot showing diaphragm and lower heart locations. The slope of the fitted linear regression lines, shown in the formula of the line, was designated as the SI translation correction factor. The R value is the Pearson product moment correlation coefficient and is a measure of the correlation between the diaphragm and the heart motion.

### 3.2.2 Non-Rigid Motion with Translation and Scaling

Besides the intersubject variability of the linear correction factor, the motion of the heart during respiration has been found to be nonrigid [52]. This can be shown by a noticeable scaling or stretching of the heart in the SI direction during respiration. Fischer et al [81] showed that the basal and apical motion of the heart is not uniform. They measured a large difference in the correction factor for the proximal and distal right coronary artery (RCA), which are 0.38 and 0.59, respectively. Another study done by Shechter et al [50] showed apparent differences in which they reported the mean SI displacement during tidal breathing of the RCA origin and distal RCA as 4.1 $\pm$ 1.6 mm and 5.9 $\pm$ 3.1 mm, respectively. That is around 30-35% difference in the motion of the proximal and distal portions of the RCA, a significant value to make a difference in the computation of an optimal correction factor. The lower degree of motion experienced by the proximal RCA shows that its location, the upper part of the heart, moves in a

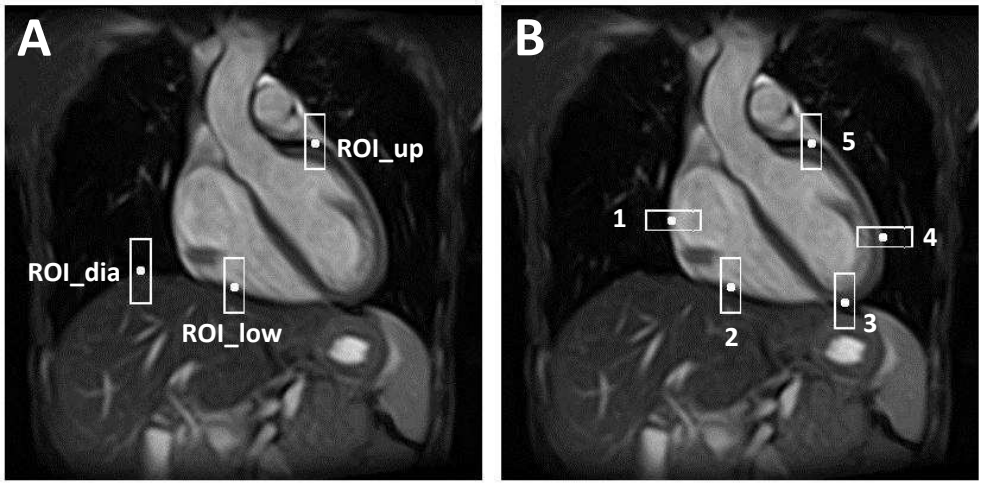


Figure 3.5: Coronal 2D SSFP MR images indicate the regions of interest (ROI) used for the nonrigid motion with SI translation and scaling (A), and affine motion model (B). The five ROIs in (B) were placed in the right (1), lower right (2), lower left (3), left (4), and upper (5) part of the heart.

lesser degree compared to the lower part, where the distal RCA can be found.

In addition to the SI translation and scaling, heart motion in the RL and AP direction, as well as rotation and shearing can also be observed [82]. One approach to handle all these motion parameters is to use affine transformation model. Although, a key challenge with this approach is the real-time update of the 12 degrees of freedom that describe the model. A calibration approached based on multiple navigators was implemented by Mahnke et al to reduce the model complexity [82]. However, the additional navigators affect its compatibility with inhomogeneous RF coil sensitivities. These navigators might interfere with parallel imaging techniques which use arrays of tiny sensitive coils. Also, even though studies reported significant values in other motion parameters, AP and RL translation may not be prominent respiratory motions in some cases. Jahnke et al [83] reported their measured mean correction factors of for the anterior-posterior and left-right directions were nearly zero. Rotational motion was also shown to be minimal in most cases [84].

The motion model described in this section uses two parameters to characterize the motion of the heart during respiration, namely, SI translation and scaling.

SI translation is where the majority of the motion lies. The SI scaling was used to compensate for the difference in the displacement of the upper and lower part of the heart. In order to compute for these parameters, three regions of interests were tracked in the scout scans. This includes the upper part of the heart in addition to the right hemidiaphragm and lower part of the heart (Fig. 3.5). For each image in the cine scan, the SI position of the tracked interfaces was recorded and correlated with the diaphragm motion.

In addition to the lower heart correlation coefficient $CC_{lwr}$ described in the previous section, the upper heart coefficient ($CC_{upr}$) was computed by correlating the upper heart displacement with the motion of the diaphragm. Finally, the mean value of the two correlation coefficients was used to compensate for the difference in upper and lower heart motion. This was done to create an averaging of the motion correction rather than correcting for either one of the upper or lower heart motion only. Using the upper coefficient might underestimate the motion of the lower heart and introduce motion artifacts in the distal parts of the coronary arteries. The opposite might also be possible if the lower correction factor is used and blurring in the proximal part arises. We theorized that the mean value of the two correlation coefficients given by

$$CF_{mean} = \frac{CC_{lwr} + CC_{upr}}{2}, \tag{3.6}$$

would offer a better alternative as the SI motion navigator correction factor.

### 3.2.3 Affine Transformation

The affine motion model, which includes linear scale, shear, and rotation in addition to 2D translation can also be used to compute for the correction factor. To compute for the correction factor, additional ROIs were needed and placed around the edges of the heart. These were used to record the motion of the bottom part of the left ventricle, right part of the heart in the right atrium and the left side of the left ventricle.

The tracking of the edges inside the placed ROIs were used to estimate the correction factor of each part. This is similar to the method used in the previous section for getting the correlation coefficient of the upper and lower heart. The ROIs were placed such that the center point of each ROI lies at the edge of the

heart wall and tracks it during respiration, as the heart moves in each slice in the cine scan. These five sets of points served as basis for correlating the diaphragm motion with the motion of the heart. Consequently, each tracked ROI produces a correction factor and these correction factors were used for the estimation of the affine parameters.

In 2D Cartesian coordinates, the affine transformation matrix, $T$, maps each point $\mathbf{r} = [x\ y]^\intercal$ to a new position $\mathbf{r}' = [x'\ y']^\intercal$ according to the formula

$$T = Ar + v = \begin{bmatrix} s_x \cos\theta & -s_y \sin\theta \\ s_x \sin\theta & s_y \cos\theta \end{bmatrix} \begin{bmatrix} x \\ y \end{bmatrix} + \begin{bmatrix} d_x \\ d_y \end{bmatrix}, \tag{3.7}$$

where $A$ is the linear transformation and $v$ is the translation vector. The coefficients $s_x$, $s_y$ are the scaling parameters in the $x$ and $y$ direction and $\theta$ is the corresponding rotation angle.

There are several approaches published on how to estimate the affine motion parameters between images [85, 86]. However, these approaches have several limitations in terms of robustness, uniqueness, and computational complexity [87]. The last of which is of particular importance for coronary MR since scan time overhead needs to be minimized during imaging. The estimation of affine parameters should be fast enough without compromising the accuracy of the respiratory motion correction.

There were five ROIs used to estimate for the affine motion parameters (Fig. 3.5B). Each heart ROI was tracked and correlated with diaphragm motion to estimate for its correlation coefficient. The regions of the heart covered were both left and right edges of the lower heart ($CC_{lwl}$ and $CC_{lwr}$), left and right side ($CC_l$ and $CC_r$) and the upper part of the heart ($CC_{upr}$).

For the modelling of affine transformation, only translation and scaling parameters were considered and rotation was assumed to be negligible ($\theta = 0$). To compute for the translation parameters $d_y$ and $d_x$, the average between the coefficients of the right and left heart and between the upper and lower heart were used, respectively. Given the motion coefficient for the lower right ($CC_{lwr}$), lower left ($CC_{lwl}$), and upper ($CC_{upr}$) part of the heart, the translation parameter in the SI direction is

$$d_y = \frac{\frac{CC_{lwr}+CC_{lwl}}{2} + CC_{upr}}{2}, \tag{3.8}$$

while the RL translation is computed from $CC_r$ and $CC_l$ using

$$d_x = \frac{CC_r + CC_l}{2}. \tag{3.9}$$

The scaling factors $s_x$, $s_y$ were estimated such that they reflect the displacement difference between the upper and lower heart and between the right and left heart, respectively. To do this, the width and height of the heart were approximated from the center points of the ROIs and used to normalize the scale factors. The scaling factors can be expressed by the following equations:

$$s_y = 1 + \frac{\frac{CC_{lwr}+CC_{lwl}}{2} - CC_{upr}}{h}, \tag{3.10}$$

$$s_x = 1 + \frac{CC_r + CC_l}{w}, \tag{3.11}$$

where $h$ and $w$ corresponds to the height and width of the heart, respectively. The height was computed by getting the SI distance between the edge of the lower right (2) and upper (5) heart while the width came from the RL distance of the right (1) and left (4) edge of the heart (Fig. 3.5B).

## 3.3. Method

Seven healthy adult volunteers (5 males and 2 females, age range, 19-24 years; mean age, 22 ± 2), whose heart were in sinus rhythm and who did not have contraindications to MR imaging were examined during free breathing. All participants gave their written informed consent and the study was approved by the Institutional Review Board of the Kyoto University Hospital.

A cine scan of 60 2D coronal images for each of the subjects was used to get the motion of the heart and its surrounding tissues and organs during free breathing. Images were obtained using steady-state free precession (SSFP) sequence with TR = 3.2 ms, TE = 1.6 ms, slice thickness = 8 mm, acquisition matrix 160 × 128, reconstructed matrix size = 320 × 256, field of view (FOV) = 375 × 300 mm, and 1.1719 mm pixel spacing using a 1.5 Tesla (1.5T) MRI scanner (Excelart Vantage, Toshiba Medical Systems, Tochigi, Japan).

The upper and lower heart motion correlation coefficients were measured for all subjects. The coefficients were both measured using automatic motion tracking and manual tracking for comparison. The correlation coefficients measured

from automatic tracking are then used to compute for the motion parameters used for the different motion models.

To evaluate the effectiveness of the respiratory motion models, simulated scans were generated and compared to the original scout cine scan. The first slice in the scout scan was used as the reference image in simulating the 2D respiratory motion. It was transformed using the three different models to predict the location and orientation of the heart given the diaphragm location. The reference image also served as the first slice in all the simulated scans. There were 60 slices in the original dataset, each with a tracked diaphragm location, so the models needed to simulate 59 images by transforming the reference image. Each succeeding slice was computed by multiplying the measured diaphragm displacement in that slice with the transformation matrix and applying the transformation to the reference image. This was done by assuming that the diaphragm location in the reference slice is the starting position, no matter which phase of the respiratory cycle it is in. No gating window was applied during the transformation of the reference image which means that all diaphragm locations were used and the gating efficiency is 100%.

The transformation matrix for each model differs in the number of parameters used. The rigid body translation model used only the SI translation parameter ($d_y$). The lower right heart coefficient ($CC_{lwr}$) was used since it is the one usually measured in studies using the subject-specific navigator gating. For the second model, SI translation and scaling parameters were used. The affine correction model utilized all 2D motion parameters except rotation.

After the affine motion corrected scans were generated, the resulting transformed images were then compared to the original acquired dataset using peak signal-to-noise ratio (PSNR) and absolute image difference as image quality measures. To avoid the motion effects of the background and surrounding tissues that does not move with the heart, only the region of interest containing the heart was used for evaluation. This way, only the heart ROI of the heart was tracked and compared even though the transformation was applied to the whole image.The simulation and image comparison was done for all subjects in the study.

## 3.4. Results

All examinations were completed in all participants without any complications. For Subject 1, the resulting locations of the diaphragm, upper heart and lower heart edges inside the respective ROIs are shown in Fig. 3.6. Each point in the horizontal axis corresponds to a slice in the SSFP scan. The vertical axis shows the measured edge in terms of pixel location, where the first pixel starts from the superior direction of the image. The edge locations were also monitored through visual inspection to estimate the motion coefficients and there are no statistically significant differences between its values and the values acquired using automatic ROI tracking.

End-inspiration states are shown as the peaks of the right hemidiaphragm. The measured diaphragm locations does not show all the peaks during the whole duration of the scan since there are not enough samples per respiratory cycle. The temporal resolution of the scan only allowed for about three to four slices per cycle. The measured diaphragm locations in Subject 1 has a displacement of 10.6 mm (9 pixels) from end-inspiration to end-expiration. This value varies between subjects, with the smallest displacement measured at 9.4 mm and largest at 18.8 mm.

An example scatter plot showing the correlation of the diaphragm motion with that of the upper and lower heart was already shown in Fig. 3.4. The value of the Pearson product moment correlation coefficient for the lower heart (R2 = 0.91) indicates that the diaphragm position is well correlated with the respiratory motion of that part of the heart. The value of the coefficient for the upper heart (R2 = 0.58), however, is significantly lower and this is true for all the examined cases.

In tracking the motion of the upper and lower heart for the translation and scaling model, we computed for the correlation coefficient of the two heart ROIs. The estimated $CC_{upr}$ and $CC_{lwr}$ values for all the subjects are summarized in Table 4.1. The estimated $CC$ values using an automatic motion tracking were compared with the values gathered using manual tracking. The values gathered using the method correlate with that of the manual method with some exceptions. This may be due to the subjective nature of manually looking for diaphragm and heart edges for the manual tracking.

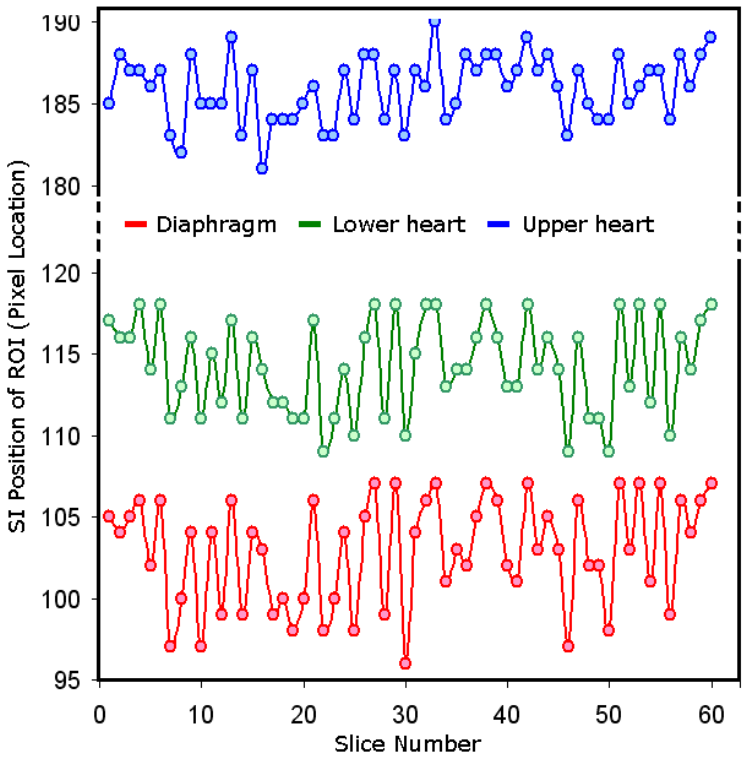


Figure 3.6: Tracked locations of the upper and lower heart and diaphragm edges inside the regions of interests.

Both the automatic and manual values showed that there is a wide variation in the the upper and lower heart coefficient for each subject. The value of the lower heart coefficient is always larger than that of the upper part and the difference between the two values ranges from 28% to 61%. This study observed a high variability between the upper and lower heart motion over the volunteer population. In all subject population observed, the value of $CC_{upr}$ varies from 0.14 to 0.53 with a mean value of 0.34. The coefficient $CC_{lwr}$, on the other hand, ranges from 0.36 to 1.09 with a mean value of 0.6.

A typical result of the comparison between the acquired and simulated cine images is shown in Fig. 3.7. The left column shows the acquired 2D coronal slices while the middle column has the simulated slices. Since the generated slices are just the transform of the reference slice (slice 1), the image difference with the acquired scan varies for every slice. The variations in the blood intensity levels

Table 3.1: The measured motion correlation coefficients ($CC$) for the upper and lower heart using automatic and manual motion tracking.

| Subject | Automatic tracking | | Manual tracking | |
|---|---|---|---|---|
| | Lower heart | Upper heart | Lower heart | Upper heart |
| 1 | 1.09 | 0.53 | 1.05 | 0.68 |
| 2 | 0.59 | 0.44 | 0.74 | 0.55 |
| 3 | 0.65 | 0.42 | 0.63 | 0.49 |
| 4 | 0.36 | 0.14 | 0.29 | 0.24 |
| 5 | 0.36 | 0.26 | 0.39 | 0.26 |
| 6 | 0.63 | 0.30 | 0.46 | 0.31 |
| 7 | 0.53 | 0.30 | 0.50 | 0.23 |

and uniformity inside the heart also contribute to the slice dependency of the resulting binary image difference.

The transformed image using the subject-specific motion models showed less image difference with respect to the original in-vivo scans compared to the transformation using a fixed 1D SI translation correction factor. In Table 3.2, the average values of the image intensity difference for all subjects are shown. There is less image difference in almost all slices in the dataset when using affine motion model as compared to 1D translation model. In average, this method allowed for 7% improvement in the accuracy of describing the respiratory-induced cardiac motion compared to motion tracking using 1D translation. The improvement reached 17% for one of the subject data and can increase more if only the shape and edges of the heart is considered. A simple T-test applied to the image difference data proved that the results are statistically relevant ($p<0.001$). It indicates that better tracking of the heart motion was achieved using affine motion model as shown by the lower image difference.

## 3.5. Discussion

As shown in the Fig. 3.4, there is high correlation of the diaphragm motion with the lower part movement of the heart in the SI direction. In all subjects, the

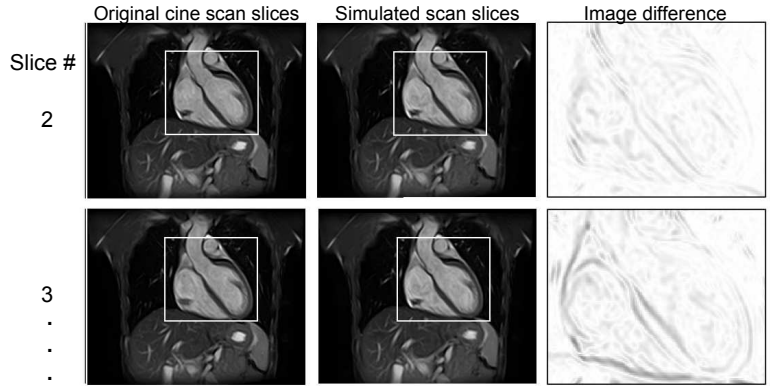


Figure 3.7: Comparison of simulated with the original acquired cine scan. The left column shows the original cine scout scan, the middle column the simulated slices using affine motion model and the right column is the image difference between a cine scan slice and a simulated scan slice.

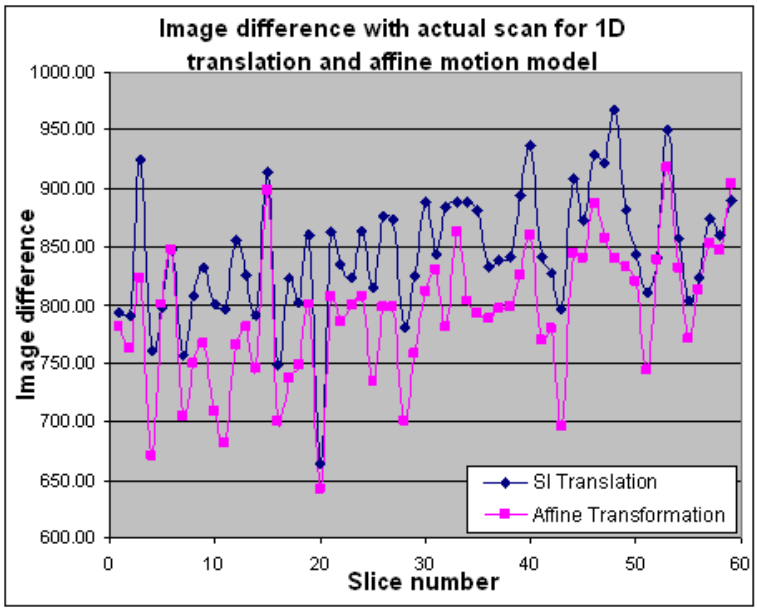


Figure 3.8: The average computed image difference of the SI translation and affine motion model with respect to the original 2D dataset for all subjects. The 2D affine transformation consistently gave lower image difference with respect to the original scan.

Table 3.2: Average image difference for 1D translation and affine motion model

| | Average Image Difference | | |
|---|---|---|---|
| Subject | SI Translation | Affine Transformation | % Difference |
| 1 | 839 | 696 | 17.04% |
| 2 | 1232 | 1151 | 6.57% |
| 3 | 1040 | 1041 | -0.10% |
| 4 | 544 | 500 | 8.09% |
| 5 | 735 | 683 | 7.07% |
| 6 | 972 | 912 | 6.17% |
| 7 | 401 | 380 | 5.24% |

Pearson product-moment correlation coefficient or the R value ranges from 0.3 to 0.9 with the highest possible value of 1 for total dependence of heart motion to diaphragm movement. Part of the reason why there are low R values for some subjects can be explained by hysteresis, where diaphragm drifts during the duration of the scan and the movement of the heart differs during inspiration and expiration.

The values derived from the slope of the fitted lines suggest that the upper and lower heart correction factors are not uniform and offer evidence of the dissimilarities in the respiratory-induced cardiac motion between subjects. These results confirm the earlier reported studies indicating the intersubject variability of correction factors [53, 79]. Additionally, the intrasubject difference of the upper heart and lower heart correction factor indicates the nonrigid motion of the heart in the SI direction. This means that the motion of the heart experiences not only SI translation but SI scaling as well.

The results show that the lower part of the heart experiences more SI displacement than the upper part during free breathing. With a 1 mm movement of the top of the hemidiaphragm, the motion of the lower heart ranges from more than 0.3 mm to 1 mm while its only 0.1 to 0.5 mm for the upper heart. This can be attributed to the physiology of the heart where the lower part is located in the pericardium, which is attached to the middle of the diaphragm. Every time the diaphragm moves in the inferior direction during inspiration, it pulls the peri-

cardium along with the heart. This, together with the gravity pull on the heart makes up the majority of the SI translation in the inferior direction. However, on the duration of the expiration, the upper heart's motion is restricted by the physiology around it. The upper part of the heart is anchored to the aorta and the major pulmonary veins. These connections restrict the upper heart motion during respiration. The pericardium surrounding the heart is also attached to the posterior part of the sternum and further limits its movement.

Tracking of the different heart ROIs in free-breathing scout cine scans allowed for the estimation of affine motion parameters like translation and scaling (SI and RL). The estimation of the affine parameters was done without further image processing or segmentation, therefore, it did not require a long calculation time. The resulting affine motion model showed better accuracy in predicting the heart motion in 2D as compared to the 1D SI motion model.

Furthermore, the proposed estimation of affine motion parameters has several advantages compared to previous implementations of affine motion correction. First, it does not require an iterative search and large matrix multiplications, which can lead to high computational costs. In addition, it takes into account the difference in displacement of the upper and lower heart during respiration. The lower part of the heart experiences more motion than the upper part during free-breathing. The estimation of the scaling parameters compensates for this difference in displacement, thus giving a more accurate heart deformation model as compared to rigid transformation.

The image difference of the transformed 2D images and the original acquired cine images vary from slice to slice due to the blood intensity variations from turbulent flow effects and the cardiac gating during the scout scans. Changes in the shape of the heart, however, still reflected the effects of diaphragm motion and were predicted by both the SI motion with scaling and affine transformation model.

# Chapter 4

# Respiratory Motion Correction Simulation Platform

Coronary Magnetic Resonance Angiography has been increasingly used in the clinical imaging of coronary arteries. It offers sharp contrast between the blood and the arterial wall and enables a more accurate diagnostic of lesions and arterial blockage. Since it is a form of MRI, it does not expose patients to radiation, unlike CT or positron emission tomography (PET). However, CMRA can be adversely affected by patient motion, more specifically by cardiac cycle and respiratory motion. Cardiac cycle motion is usually addressed using ECG triggering.

Many studies have been done to compensate for respiratory motion and avoid image degradation in CMRA. The more common methods are under the *prospective* motion correction type, which predict and correct for respiratory motion during the duration of the scan. These include the navigator-guided, 1D translation correction [53]. This method tracks the motion of the diaphragm in the SI direction and uses the fixed correction factor value of 0.6, which indicates the displacement of the heart, in mm, for every 1 mm movement of the diaphragm. The method is commonly used in CMRA scanners because it is simple and easy to implement. However, it treats the heart as a rigid object and does not entirely describe the respiratory heart motion. Other more recent studies try to correct for two- and three-dimensional motion [81], [88]. The increase in motion approximation accuracy consequently increases the complexity of implementing the method in the MR scanner. More complex methods are not easily implemented in

scanners because of their proprietary nature. In addition, the more complex the correction becomes, the more it can add to the possibility of prolonging CMRA scans, which already take around 20 to 30 minutes for each patient.

In addition, the acquisition of a high quality 3D coronary data depends on the patient or subject under study. The respiratory motion of the heart is highly subject-specific. The previous chapter also indicates that there are significant variability in the motion of the upper and lower heart. These present a problem during acquisition since the tailoring of correction for each patient can add to acquisition time. It adds a factor for CMRA clinicians and radiologists to consider in deciding which is the appropriate and practical correction method for them.

The number of these respiratory motion studies and the complexity of their implementation make it impractical to test and evaluate them for multiple subjects. A quantitative comparison of these proposed methods is also not available because these studies used different types of scanners and different subjects. To clinically evaluate these methods using the same scanner and subjects would be impractical and time-consuming. Furthermore, the use of clinical scans would result in other sources of artifacts that affect the image quality of the resulting scan like cardiac cycle motion and magnetic inhomogeneities in the machine [89]. A quantitative comparison should be able to measure the effectiveness of a motion correction study while eliminating the effects of other sources of motion. With this, we propose a method to quantitatively compare different respiratory motion correction techniques, independent of other sources of motion and image artifacts.

We designed and implemented a CMRA simulation platform that clinicians can use to compare different respiratory motion correction methods. The simulation software can run in general-purpose computers, so the clinicians does not have to implement the different methods under evaluation in the actual scanner. In addition, it can be used to standardize the evaluation of correction methods. The platform utilizes a patient-based voxelized model with the capacity to recreate the patient-specific respiratory motion derived from cardiac MR scout scans.

In terms of using the navigator-guided 1D translation correction, we used the platform to evaluate different *CF* candidates to determine which *CF* can best

predict a subject's respiratory motion. We evaluated this method because it is readily available in most clinical scanners, including the one we used in this study.

## 4.1. Method

The proposed simulation platform for comparing respiratory motion correction methods is composed of two major parts, namely, respiratory motion model and CMRA motion correction simulator. The respiratory motion model recreates the subject-specific cardiac motion as a function of diaphragm motion. The respiratory motion modelling involves tracking and correlating the diaphragm and heart motion from real 2-D scout scans. The CMRA motion simulator virtually implements motion correction methods to correct the simulated respiratory-induced motion artifacts on a CMRA scan. The simulation method uses the $k$-space formalism to introduce and correct motion in a reference 3D scan. In addition, the motion correction simulator includes the quantitative image quality comparison of the generated scans from different correction methods.

### 4.1.1 Simulation Platform Algorithm

This section describes the inputs and outputs of the proposed simulation platform as well as the steps to generate the outputs. Given a set of 2-D MRI scout scans $\boldsymbol{R} = \{R_1, R_2, \ldots, R_M\}$, where $M$ is number of 2D image slices, and a reference 3D Coronary MRA image $\boldsymbol{Q}_{Ref}$, the goal of the simulation platform is to find the motion correction method $c_p$ from $C = (c_1, c_2, \ldots, c_Z)$ that can best predict the respiratory-induced motion of the heart during the CMRA scan. The simulation platform process can be described with the following algorithm:

1. Estimate the respiratory motion correlation coefficients from a set of 2D MRI scout scans.

2. Generate a discrete respiratory waveform with $K$ translation levels from a randomly-generated sinusoidal wave.

3. Apply spatial transformation to a reference 3D Coronary MRA image,

$\boldsymbol{Q}_{Ref}$, for each translation level $y_k \in Y = \{y_1, y_2, \ldots, y_K\}$ using the estimated correlation coefficients.

4. Acquire the uncorrected $k$-space data, $\boldsymbol{\mathcal{Q}}_{nc}$, using *in-vivo* MRI $k$-space acquisition simulation and by sampling the respiratory waveform.

5. Apply motion correction to the uncorrected $k$-space data $\boldsymbol{\mathcal{Q}}_{nc}$ for each of the correction methods in $C = (c_1, c_2, \ldots, c_Z)$.

6. Transform all the motion-corrected $k$-space data into 3D CMRA image data.

7. Assess the effectiveness of each method in $C$ by comparing the resulting 3D CMRA images using some commonly-used image quality measures.

Steps $1 - 3$ of the algorithm above belong to the respiratory motion model part, while steps $4 - 7$ belong to the CMRA motion simulator part.

As an example implementation of the proposed system, we used the comparison of using different values of the correction factor in respiratory motion correction. It assumes that a single *CF* is used to correct for respiratory motion during CMRA scan, which is the technique commonly utilized in many scanners today. The values of *CF* are estimated from the *correlation coefficient* values between the diaphragm and heart motion. These values are derived from the set of time-series 2D coronal scout scans $\boldsymbol{R}$. The final product of the simulation is the correction factor $CF = c_p$ which gives the 3D data with the highest image quality in terms of SNR, CNR, vessel length and vessel edge definition.

The following subsections give a more detailed description of the steps in the algorithm. Subsection 4.1.2 elaborates on how the *CC*s are estimated. Subsections 4.1.2 and 4.1.2 describe how the respiratory waveform is generated and the reference scan is transformed, respectively. In addition, the last part of the Method section details the motion correction simulator, which includes the simulation of MR $k$-space data acquisition and motion correction.

### 4.1.2 Modeling Respiratory Motion

The respiratory motion of the heart involve the contribution of diaphragm, chest wall, and the physiology of the heart itself. When the diaphragm contracts, if

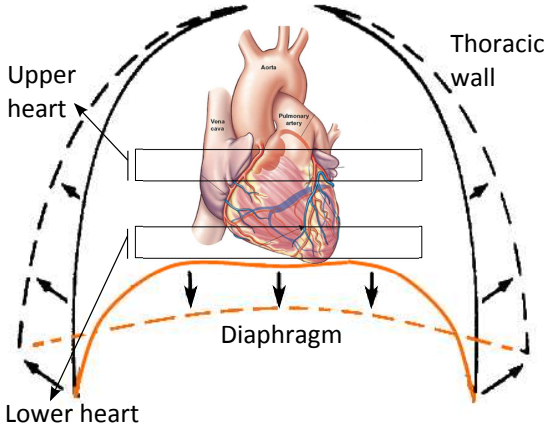


Figure 4.1: Motion of the diaphragm and the thoracic cage during respiration. During inspiration, the diaphragm contracts forcing the abdominal contents including the heart to move downward. During expiration, the diaphragm relaxes, pushing the heart upwards.

forces the abdominal contents downward and increases the volume of the thorax. When the diaphragm relaxes, the abdominal contents move upward and the volume of the thorax decreases with its inward motion (Fig. 4.1). The level of the diaphragm can move up and down from 10-100 mm during breathing. However, the diaphragm moves only around 10 mm during tidal breathing [90]. During this cycle, the heart moves upward and downward together with the diaphragm. The chest wall also moves upwards and downwards, increasing and decreasing both the transverse and anteroposterior diameters of the thorax but 180 degrees out of phase with the diaphragm and heart motion.

### Motion Parameter Estimation

The first step in simulating respiratory motion correction is to model the subject-specific respiratory-induced motion of the heart. This involved tracking the heart as it moves with the diaphragm during respiration and measuring its correlation coefficients. The tracking was done on a cine scout scan, which is a two-dimensional, time-series image data showing the heart in the coronal plane. In order to get the $CC$ values of the heart, six regions of interest (ROI) were tracked for each image in the cine scan. Diaphragm motion was tracked using a rectan-

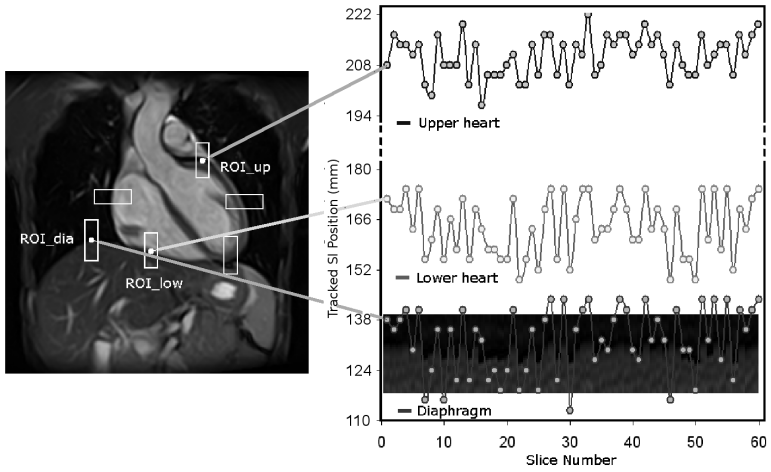


Figure 4.2: Region-of-interest (ROI) motion tracking model for the diaphragm and heart. The right side shows the tracked location of the diaphragm and the heart ROI for all images in the scout scan. The tracked locations are used to compute the correlation coefficient ($CC$) values.

gular ROI with dimensions of 30 $\times$ 10 pixel, placed in the dome of right hemidiaphragm (Fig. 4.2). The remaining ROIs were placed along the edges of the heart to track the superior-inferior (SI) and right-left (RL) cardiac motion. To measure the displacement, the SI location of the horizontal edge was subtracted from a fixed reference location. The edge location is detected by computing for the gradient magnitude of each horizontal line in the ROI and then searching for the local maxima of the gradient.

Least-squares method was used to determine the edge displacements inside the ROIs. The measured displacements for each image are then correlated with the corresponding displacements of the diaphragm. The slope of the linear regression lines in the correlation graph (*i.e.* diaphragm vs. heart ROI) was assigned as the $CC$ value for that region of the heart. The $CC$ estimation part of the algorithm (Step 1) for the upper ($CC_{upr}$) and lower ($CC_{lwr}$) heart can be summarized as shown in Algorithm 4.0.1.

**Algorithm 4.0.1:** Estimation of motion parameters.

**Data**: $\boldsymbol{R} = \{R_1, R_2, \ldots, R_M\}$.

**Result**: correlation coefficient $cc_{upr}$ and $cc_{lwr}$.

**for** $m \leftarrow 1$ **to** $M$ **do**

  place regions of interest (ROIs) in $R_i$

  diaph_loc$[m] \leftarrow$ `measureDiaphragmLocation`$(R_m)$

  heUpr_loc$[m] \leftarrow$ `measureUpperHeartLocation`$(R_m)$

  heLwr_loc$[m] \leftarrow$ `measureLowerHeartLocation`$(R_m)$

$CC_{upr} \leftarrow$ `calcCorrelCoef`(diaph_loc, heUpr_loc)

$CC_{lwr} \leftarrow$ `calcCorrelCoef`(diaph_loc, heLwr_loc)

$C \leftarrow$ `assignCorrectionFactors`$(CC_{upr}, CC_{lwr})$

### Respiratory Waveform Generation

The time varying parameters in the model were chosen to fit a diaphragm motion curve for normal tidal breathing (Fig. 4.3). The average respiratory rate for adults is usually given at 12 breaths per minute or a period of 5 seconds but lies in the range of 12-20 breaths per minute [91]. For a period of 5 seconds, 2 seconds of that is inspiration while the remaining 3 is expiration. The amplitude of the motion curve was set to 10 mm, which indicates the maximum displacement of the diaphragm during free breathing. The zero level or reference position, where the diaphragm displacement is equal to zero corresponds to the end-expiration phase.

To simulate the rhythmic motion of the diaphragm during tidal breathing, we created an arbitrary sinusoidal waveform with a randomly varying frequency. The frequency range was set at 0.33 to 0.2 Hz to reflect the average range of respiratory rate for adults, which is around 12 to 20 breaths per minute. We used a sinusoidal wave so that we can easily randomize the frequency of respiration. Consequently, a real data of diaphragm motion (*e.g.* from respiratory bellows) can also be used to provide a more realistic waveform shape and frequency variation. The generated diaphragm waveform is described by the following continuous equation:

$$diaph(t) = 0.5\cos(\frac{\pi}{P_r})t + 0.5 \text{ cm}, \quad 0.20 \leq \frac{1}{P_r} \leq 0.33Hz, \tag{4.1}$$

where $P_r$ denotes the random respiration period (3 – 5 s) and $t$ is the time in

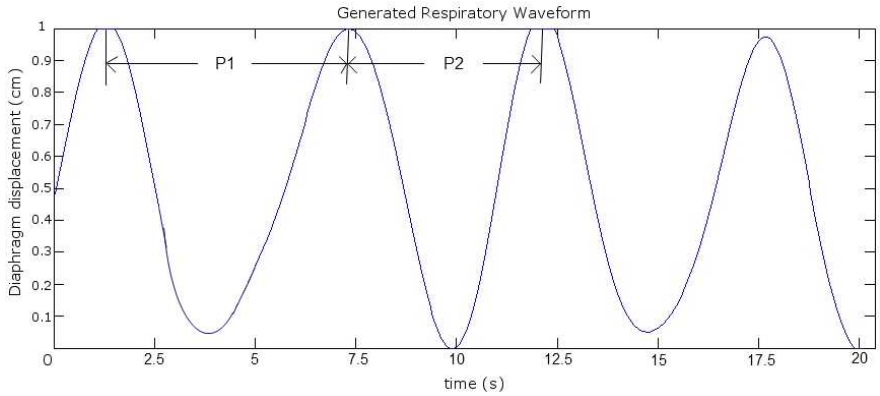


Figure 4.3: The motion curve of the diaphragm. The curve resembles that of a sinusoidal wave with a varying period $P_r = 4 - 5s$ (12–15 breathes per minute).

**Algorithm 4.0.2:** Generation of the discrete respiratory waveform.

**Data**: diaphragm trans levels $Y = \{y_1, y_2, \ldots, y_K\}$.

**Result**: discrete respiratory waveform $diaph[]$.

generate continuous respiratory waveform $diaph(t)$

assign $N$ as number of discrete samples

**for** $n \leftarrow 1$ **to** $N$ *seconds* **do**

$\lfloor diaph[n] \leftarrow$ `sampleResWave`$(n, diaph(t))$, where $diaph[n] \in Y$

seconds. The waveform oscillates in the $[0, 1]$ amplitude range, which is set as the displacement range of the diaphragm from end-expiration to end-inspiration (in cm). The amplitude range is divided into $K$ discrete levels or positions with each level having the value of $y_k$, where $k = 1$ to $K$. The amplitude of 1 cm is the default maximum displacement of the diaphragm in the simulation platform but this can easily be changed into any value, depending on the measured diaphragm movement of the subject. The discrete respiratory waveform generation procedure (Step 2) can be summarized in Algorithm 4.0.2.

### Spatial Transformation of Reference Image

Since most of the induced motion in the coronary arteries is in the SI direction and most MR scanners only allows for an SI correction factor, the simulation

**Algorithm 4.0.3:** Transformation of the reference image for every translation level $y_k$.

**Data**: high-quality 3D CMRA reference scan $\boldsymbol{Q}_{Ref}$ and correlation coefficients $CC_{upr}$ and $CC_{lwr}$.

**Result**: transformed dataset $\boldsymbol{Q}[]$.

$A(s_x, s_y) \leftarrow$ `calcScalingParams`$(CC_{upr},\ CC_{lwr})$

$v(d_x, d_y) \leftarrow$ `calcTranslationParams`$(CC_{upr},\ CC_{lwr})$

**for** $k \leftarrow 1$ **to** $K$ **do**

  $T_k \leftarrow$ `createTransformMatrix`$(y_k, A, v)$

  $\boldsymbol{Q}[k] \leftarrow$ `applyTransformation`$(\boldsymbol{Q}_{Ref}, T_k)$

only considered motion in the z-direction. In addition to translation, SI scaling was included in order to get the effect of different motions in the upper and lower part of the heart. The affine transformation matrix used to transform the 3D model has only two parameters, the translation and scaling parameter in the SI direction while the rest are set to zero.

The translation and scaling parameters were based on the results gathered in Chapter 3 about the motion of the upper and lower heart, specifically the correction factors $CC_{upr}$ and $CC_{lwr}$. In addition to some corrections factors gathered measured in previous studies, this research also took into account the possible extreme values of these correction factors as correlation coefficient (Table 4.1). This ensures that the simulation considered a wider range of motion that the average correlation coefficient. In one example, the motion of the lower heart was set at 1:1 ratio with diaphragm movement and the upper heart at 0.5:1. This means that for every 1 mm movement of the diaphragm, the lower heart moves 1 mm ($CC_{lwr} = 1$) and the upper heart takes a displacement of 0.5 mm ($CC_{upr} = 0.5$).

To simulate heart displacement during respiration, the reference dataset is first assigned as an undeformed heart located in end-expiration. The simulated diaphragm motion range is set to the default value of 10 mm, from end-expiration to end-inspiration. The spatial resolution of the diaphragm movement is 0.5 mm, which gives a total of 20 diaphragm positions $(y_1, y_2, \ldots, y_{20})$ for the whole range of motion, excluding the end-expiration position. For each level $y_k$, the reference

Table 4.1: Correlation coefficients used to transform the reference dataset.

| **Upper heart** $CC$ | **Lower heart** $CC$ |
|---|---|
| 0.20 | 0.3 |
| 0.26 | 0.36 |
| 0.30 | 0.5 |
| 0.30 | 0.6 |
| 0.30 | 0.8 |
| 0.40 | 0.65 |
| 0.40 | 0.7 |
| 0.50 | 0.9 |
| 0.50 | 1.0 |
| 0.70 | 2.0 |
| 0.80 | 1.2 |

image $\boldsymbol{Q}_{Ref}$ undergoes spatial transformation to generate the transformed 3D image $\boldsymbol{Q}[k]$. The transformation is done by multiplying each voxel in the reference image by the transformation matrix $T_k$. The process of generating the transformed images for each diaphragm translation level (Step 3) can be summarized in Algorithm 4.0.3.

### 4.1.3 CMRA Motion Correction Simulator

#### Acquisition of Uncorrected *k*-space Data

After each transformation, the the transformed 3D image $\boldsymbol{Q}[k]$ is converted to $k$-space data $\boldsymbol{\mathcal{Q}}[k]$ using 3D Fast Fourier Transform (FFT). Each of these data in the $k$-space dataset is used for simulating the MR acquisition of the uncorrected data $\boldsymbol{\mathcal{Q}_{nc}}$.

MR image acquisition involves the filling of $k$-space data. The $k$-space represents the spatial frequency information in two or three dimensions of an object. In an actual MRI scanner, the phase and frequency encoding data is structured in this $k$-space grid, which is filled one line (or multiple lines) at a time until the image is complete (Fig. 4.4). Each point in the sampled waveform corresponds to a diaphragm position and the simulated 3D dataset was created by getting the

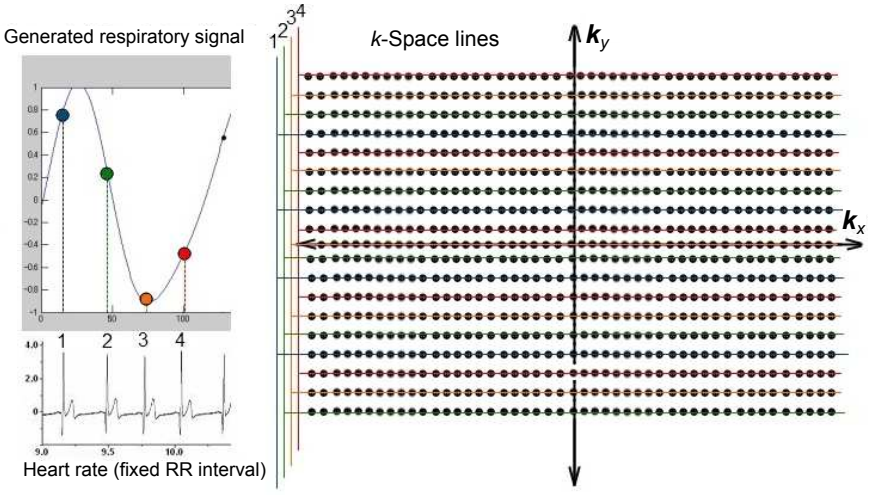


Figure 4.4: $k$-Space filling using segmented rectilinear sampling. A set of $k$-space lines was filled every heart beat with the $k$-space data from the sampled diaphragm position in the respiratory waveform.

$k$-space data in each of these positions. A complete dataset was generated when all the $k$-space lines in the volume were filled.

The $k$-space data is in Fourier space and contains all the necessary information to reconstruct an image. It is related to the image data through the Fourier transformation. Sampling of the acquired signal in MRI is arranged such that low-frequency signals are at the center of the acquired data and the high-frequency signals are placed around this center. The rightmost column of Fig. 4.5 shows examples of a typical uniformly sampled $k$-space data.

To acquire MRI data in the simulation platform, $k$-space data acquisition is performed during each sampled point in the generated respiratory waveform $diaph(t)$. Figure 4.5 shows that a $k$-space equivalent $\boldsymbol{\mathcal{Q}}[k]$ is acquired for each transformed image $\boldsymbol{Q}[k]$. Each point in the sampled waveform corresponds to a diaphragm position where the $k$-space line(s) will be acquired. The procedure mimics an *interleaved* acquisition in actual MRI, where a set of $k$-space lines is acquired in one cardiac cycle using segmented rectilinear encoding. A complete dataset is created when all the $k$-space lines in the volume are filled. The acquisition of the 3D $k$-space data without motion correction (Step 4) can be summarized in Algorithm 4.0.4.

**Algorithm 4.0.4:** Acquisition of Uncorrected 3D $k$-space.

**Data**: transformed dataset $\boldsymbol{Q}[]$ and discrete resp waveform $diaph[]$.

**Result**: uncorrected 3D $k$-space data $\boldsymbol{\mathcal{Q}}_{nc}$.

**for** $k \leftarrow 1$ **to** $K$ **do**
  $\boldsymbol{\mathcal{Q}}[k] \leftarrow$ `imageToKspace`$(\boldsymbol{Q}[k])$
$\boldsymbol{\mathcal{Q}}_{nc} \leftarrow$ `sampleKspaceData`$(\boldsymbol{\mathcal{Q}}, diaph[])$

### Motion Correction Simulation

Once the uncorrected $k$-space data is generated, a motion correction can be applied using a correction method and the data on diaphragm displacement positions used to acquire the uncorrected data.

The platform was used to compare the effect of different correction factors on the image quality of the resulting simulated scans. First, the motion coefficients to be used for the simulations were measured for one of the volunteer scans. A pair of motion coefficients of 0.46 and 0.56 for the upper and lower heart, respectively, were used for the simulations. Once the motion coefficients were determined, five different CMRA simulations were generated. A 3D volume data was acquired for each of the following methods:

1. Acquisition without motion compensation ($\boldsymbol{\mathcal{Q}_{nc}}$).
2. Using the standard correction factor ($CF = 0.6$).
3. Using $CC_{upr}$ as correction factor ($CF_{upr}$).
4. Using $CC_{lwr}$ as correction factor ($CF_{lwr}$).
5. Using the mean correction factor ($CF_{mean}$), the average of $CF_{upr}$ and $CF_{lwr}$.

To complete the simulation, the 3D images were reconstructed from the $k$-space data using inverse-FFT. Lastly, each 3D image was evaluated and compared to the original scan using a number of image-quality measures.

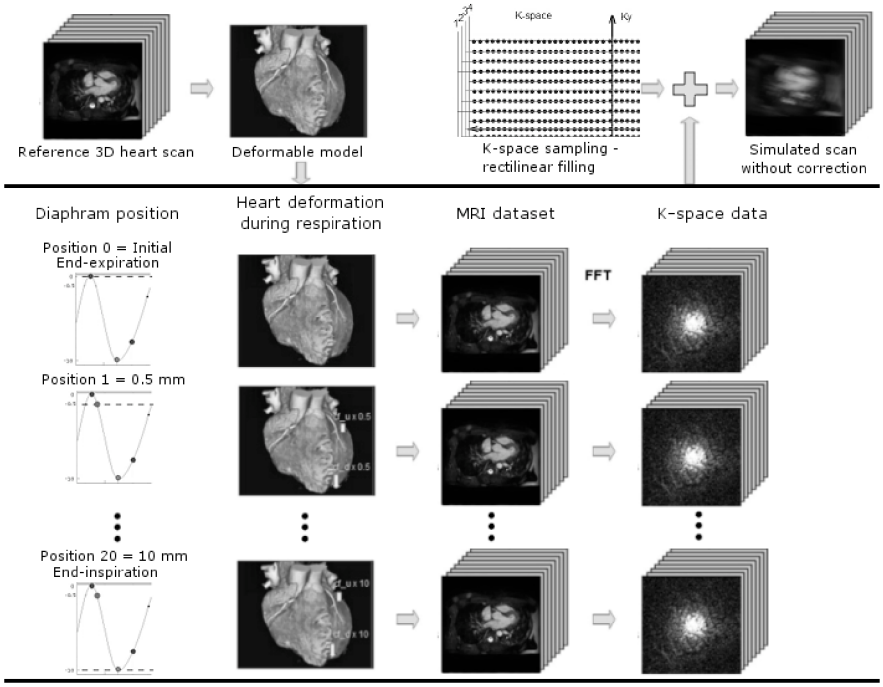


Figure 4.5: Method for generating the $k$-space dataset of the deformed cardiac model for each respiratory diaphragm position. The range of the respiratory waveform is divided into $k$ discrete levels or positions and in each level a transformed reference image is produced. The transformed 3D images are then converted to $k$-space data using FFT. The generated $k$-space data for each diaphragm displacement level are used to create the simulated CMRA acquisitions.

## 4.2. Experiments

To measure the correlation coefficients from actual subjects, eight healthy adult volunteers (5 males and 2 females, age 19 to 35 years) who did not have contraindications to MR imaging were enrolled for scout scan imaging. A total of 60 ECG-gated, time-series 2D coronal chest images were acquired per subject during free-breathing. Images were obtained during the measured cardiac rest period at end-diastole. All images were taken using steady-state free precession (SSFP) sequence in free breathing, acquired using a 1.5T MRI scanner (Excelart Vantage, Toshiba Medical Systems, Tochigi, Japan). The study was approved by the Institutional Review Board of the Kyoto University Hospital and all subjects

gave their informed written consent prior to enrolment in the study.

The reference scan used in the simulation was derived from a high-quality 3D coronary MR angiography dataset [92]. The 3D axial volume was acquired using SSFP sequence and consists of 140 slices acquired with TR = 4.3 ms, TE = 2.2 ms, slice thickness = 1.5 mm that was reconstructed as 0.75 mm thickness, acquisition matrix 256 × 168 and reconstructed matrix size = 512 × 496. The dataset was cropped to remove the background and the neighbouring organs, resulting to a reduced matrix size of 256 × 168. The segmented heart serves as the reference image ($\boldsymbol{Q}_{Ref}$) for the respiration-induced deformation and respiratory gating simulation.

### 4.2.1 Image Quality Assessment

There were two sets of methods used to assess the quality of the simulated 3D volume acquired using different correction methods. One measure was done by getting the absolute image difference between the middle coronal reformatted slice of the simulated scans and the original 3D reference scan. The SI motion of the heart as well as the image degradation induced by that motion can be seen in the coronal plane.

The other evaluation used was introduced by Dirksen et al [41]. They suggested four image quality measures as basis for standardized quantitative assessment of coronary MR angiography images. This approach required the measurement and tracing of the right coronary artery (RCA) from the aortic root up to its distal end and the acquisition of the MPR. The image quality of the reconstructed image was assessed using these measures: signal-to-noise ratio (SNR), contrast-to-noise ratio (CNR), vessel length, and vessel-edge definition or sharpness. The first three are well defined image quality measurements [93, 94, 95] while vessel edge definition has been defined as how well the borders of a particular vessel are circumscribed. For this study, the quantitative assessment was conducted on images acquired using a multiplanar reconstruction (MPR) tool in an Aze Virtual Place workstation (Aze Inc., Tokyo, Japan).

SNR is one of the important image quality measures of the performance of a magnetic resonance imaging system. It basically describe the relative contribution random superimposed signals or background noise to the detected image.

Although there is an intrinsic SNR for a particular combination magnetic field strength, spatial resolution, and the electrical properties of the subject or patient being image, it can also be affected by motion artifacts.

To measure the SNR, record the mean signal intensity value and standard deviation of a small ROI in the most homogeneous area of a tissue or organ being measured. In vessel image quality, it is a measure that quantifies the signal intensity of the studied vessel as compared with its noise and calculated using the formula SNR = $Signal_{blood}/Noise_{blood}$. Blood signal was defined as the mean value of the vessel ROI while noise as the standard deviation (SD).

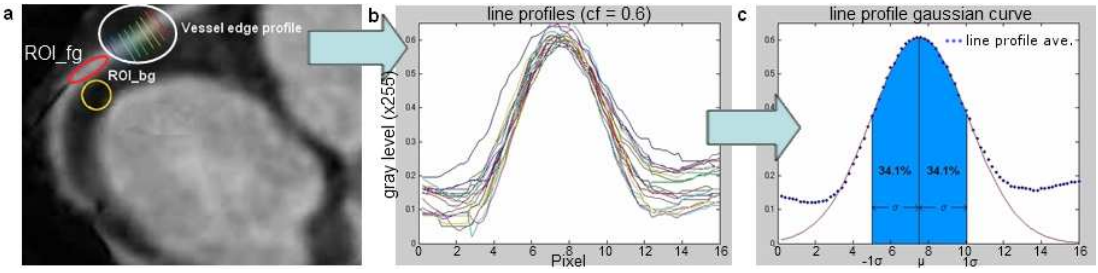


Figure 4.6: Curved MPR view of the right coronary artery near its origin in the aortic root (a). $ROI_{fg}$ was used for SNR calculations, whereas $ROI_{fg}$ and $ROI_{bg}$ were used for CNR calculations. (b) The plot shows the multiple intensity line profiles (b), which are used to compute for sigma of the fitted Gaussian curve (c). The value of sigma was used to compute for the vessel edge definition.

CNR reflects the visibility of the vessel as compared to its background or surrounding tissues. It was measured by placing a region-of-interest on a proximal coronary artery and another on the adjacent perivascular tissues in the myocardium (Fig. 4.6) and using the following equation:

$$CNR = \frac{2(Signal_{blood} - Signal_{myocardium})}{SD_{blood} - SD_{myocardium}} \tag{4.2}$$

where $SD_{blood}$ and $SD_{myocardium}$ are the standard deviation of the arterial blood and myocardium, respectively.

Vessel-edge definition quantifies how well the borders of a particular vessel are defined. A low vessel-edge definition potentially results in less accurate diagnosis of significant lesions. It is based on the calculation of signal gradients across the

borders of the coronary artery. To measure its value, 20 line profiles were placed perpendicularly at the proximal part of the RCA (Fig. 4.6). The line profiles traverses the coronary artery and its two edges. The profile curve represents the gray level intensities, where the highest values corresponds to the bright blood inside the arteries.

Analysis was performed by using Matlab 2007b on a Dell Precision T3400 workstation. Computation of the vessel edge definition here, however, is distinct from the one proposed by Dirksen et al [41]. Instead of using the down- and upslope of the line profile set, a Gaussian curve was fitted into the average of the line profiles for edge calculation. The average value of all the curves was fitted with a Gaussian bell curve and the normal distribution parameters were computed. The end variable which signifies the vessel-edge definition was calculated as 1/s, where s is equal to the standard deviation of the fitted Gaussian distribution curve. A small value of sigma corresponds to a steeper slope in the average signal intensity line profile, thus better vessel-edge definition. A large value means that the line profile and Gaussian curve has a wide distribution and the vessel edge is less defined.

The measurements for SNR, CNR, vessel length and vessel edge definition were presented as mean  SD. Comparisons between correction methods were made with two-tailed paired Students t-test with significance level of 0.05.

## 4.3. Results

The time-series coronal images acquired during the cardiac rest period under free-breathing enabled tracking of the upper and lower heart during respiration. There are wide variations in the measured $CC$ values between subjects observed during the tracking of the scout scans. There was also a wide variation between the upper and lower heart motion. Lower heart correction factor ranges from 0.36 to 1.0, while upper heart has values of 0.14 to 0.53. Figure 4.7 shows the measured correlation coefficient values for all the scanned volunteers.

In the simulation experiments, image artifacts such as ghosting and image blurring occurred when data was acquired without motion correction. Consequently, significant reductions in motion artifacts were observed when the cor-

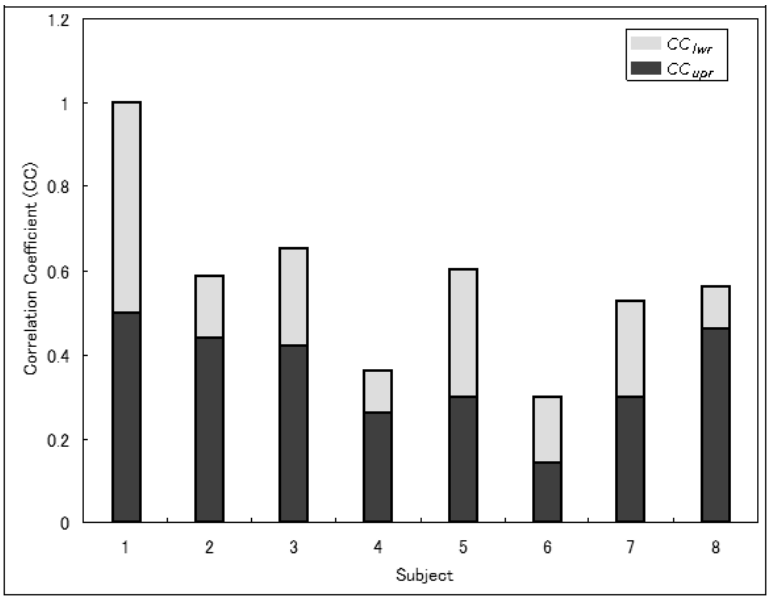


Figure 4.7: The measured correlation coefficient ($CC$) values for all the volunteer scans. $CC_{upr}$ and $CC_{lwr}$ indicates the translation of the upper and lower heart, respectively, for every 1 unit translation of the diaphragm. While $CC_{mean}$ refers to the average of the two aforementioned values.

rection methods were employed. The simulation results also showed significant variations in image quality from the different motion compensation methods used.

### 4.3.1 Coronary Artery Visualization

In Fig. 4.8, the proximal and distal cross-sections of the right coronary artery in show the effects of the different correction methods in the visual quality of the RCA. The figure shows the RCA cross-sections for both the simulated and clinical scans to validate the result of the simulations with that of an actual scan, with $CC_{upr} = 0.46$ and $CC_{lwr} = 0.56$. The proximal cross-section was taken near the root of the RCA in the aorta while the distal cross-section was acquired from the main RCA vessel in the posterior region of the right ventricle. The columns (left to right) indicate the motion correction method used; namely, no motion correction, $CF_{upr}$, $CF_{mean}$, $CF_{lwr}$, and standard correction factor ($CF = 0.6$).

The first column of Fig. 4.8 shows that the visibility of the coronary cross-

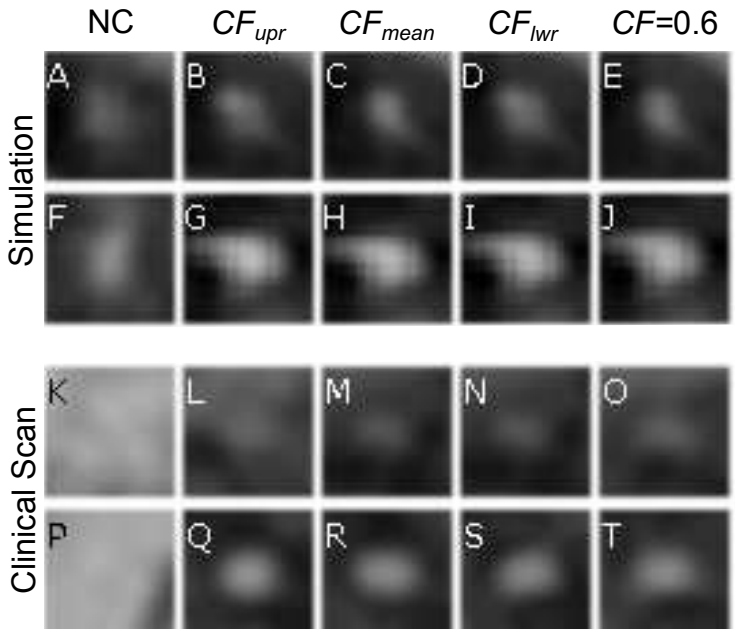


Figure 4.8: Shown are the cross-sections of the right coronary artery from the simulated (upper two rows) and clinical scans (bottom two rows). The first row of the simulated and clinical scan corresponds to the distal cross-section of the artery while the second row of each scan shows the proximal cross-section. The columns lists the motion correction methods used in the scans; namely, no motion correction (A, F, K, P), $CF_{upr}$ (B, G, L, Q), $CF_{mean}$ (C, H, M, R), $CF_{lwr}$ (D, I, N, S), and standard correction factor (E, J, O, T).

section is almost zero if there is no correction used. The use of the upper heart correction factor ($CF_{upr}$) results to a good vessel definition of the proximal RCA (Fig. 4.8(G, Q)) but gives a barely visible distal cross-section (Fig. 4.8(B, L)). On the other hand, employing the lower heart correction factor ($CF_{lwr}$) gives a relatively better image quality in the distal part (Fig. 4.8(D, N)) and but worse in the proximal cross-section (Fig. 4.8(I, S)). The image quality of the coronary cross sections resulting from $CF_{mean}$ is between that of the $CF_{upr}$ and $CF_{lwr}$. Of the four correction factors used, the standard correction factor generally gives the worst image quality, especially with respect to the proximal RCA (Fig. 4.8(J, T)). This is because its value is relatively far from the value of the actual $CC_{upr}$ (0.46). The results also show that the relative effects of the different correction

methods are consistent for both the simulation and actual clinical scan.

The results of the simulated scan image quality assessment for four selected sets of *motion coefficients* are shown in Fig. 4.9. The four sets of coefficients ($CC_{upr}/CC_{lwr}$) shown are 0.7/2.0, 0.5/1.0, 0.3/0.6, and 0.26/0.36. The five columns for each set of *motion coefficients* are the methods used in the simulation studies. The trend shows that the amount of image artifacts gets higher as the respiratory-induced cardiac motion increases (i.e. correlation coefficient values increase). The highest set of values for correlation coefficients used, which are $CC_{upr} = 0.7$ and $CC_{upr} = 2.0$, yielded the lowest image quality. Generally, the mean correction factor ($CC_{mean}$) gave the highest image quality regardless of coefficients used.

### 4.3.2 Simulation vs. Reference Scan

In order to compare the effect of motion across one slice, the image differences between the middle coronal slice of the reference scan and the simulated scans for correlation coefficient pair of 0.5/1.0 ($CC_{upr}$ / $CC_{lwr}$) are shown in Fig. 4.10. It shows the effects of using different correction factors on the image quality at different areas of the heart. Compared with the reference image slice (Fig. 4.10A), the image without motion correction (Fig. 4.10B) experienced the most difference (*i.e.* image distortion). In Fig. 4.10F, the bulk of the image difference and thus the residual motion artifact between the simulated slice and using the standard correction factor was highlighted. Since the correlation coefficient values used to transform these images are 0.5 and 1.0 for the upper and lower heart, respectively, the standard $CF$ mostly corrected for motion in the upper heart since its value is closer to $CC_{upr}$. Using $CF = CC_{lwr}$ results in residual motion artifacts around the upper region of the heart. In contrast, motion artifacts were not concentrated on any part of the heart when using the mean correction factor $CF_{mean}$. The mean correction factor gives the smallest difference from the reference image. This is confirmed by the results of the paired $t$-tests done between the results of using the mean correction factor and the other compensation methods, where the P value ranges from $8.2 \times 10^{-7}$ (no correction) to $4.0 \times 10^{-5}$ (using $CF_{lwr}$).

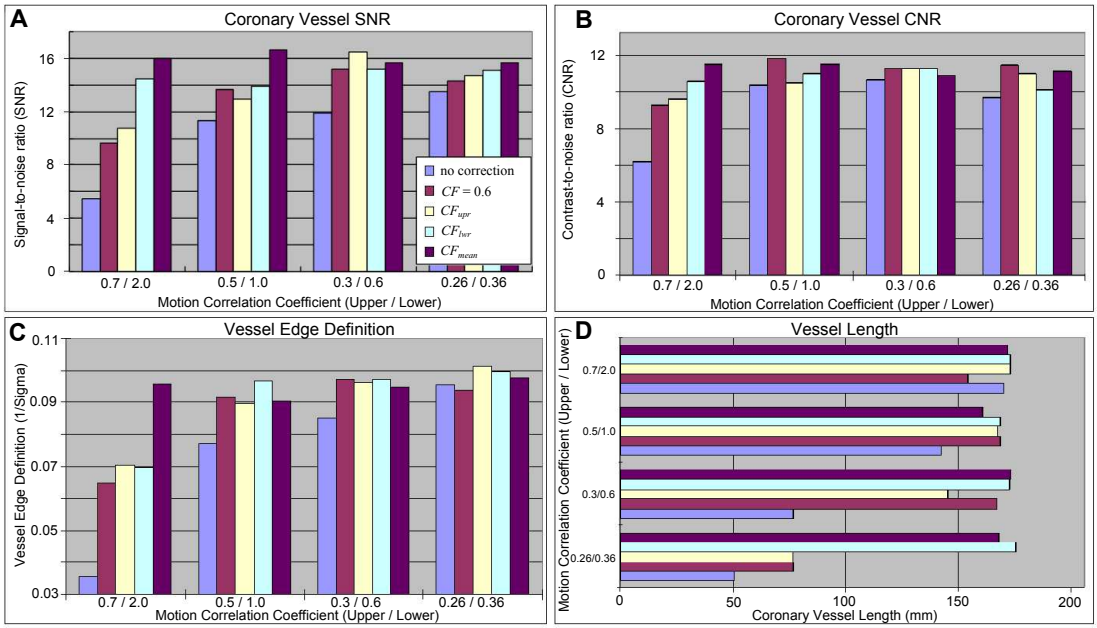


Figure 4.9: The measured image quality in terms of signal-to-noise ratio (A), contrast-to-noise ratio (B), vessel edge definition (C) and vessel length (D) for a number of simulations using different combinations of upper and lower heart correlation coefficients. The set of columns labelled 0.7 / 2.0 means that the simulation values for the upper heart ($CC_{upr}$) and lower heart coefficient ($CC_{lwr}$) are 0.7 and 2.0, respectively. The five individual columns for each set correspond to the methods used in the respiratory motion correction, namely, no motion correction, using $CF_{upr}$, $CF_{mean}$, $CF_{lwr}$, and standard correction factor ($CF = 0.6$)

### 4.3.3 Simulation vs. Clinical Scan

Validation of the simulation results was done by comparing the image quality of the simulated images with those of the actual clinical scans acquired using the same correction factors. Figure 4.11 shows the measured CNR values for the proximal (upper) and distal (lower) portions of the coronary artery for all the motion correction factors used. The measured upper and lower heart motion coefficient for the subject are 0.46 and 0.56, respectively. Results indicated that the proximal coronary artery image has a comparatively poor CNR when the lower heart correction factor is used and vice versa. The factor $CF_{mean}$, on average, gave the best CNR for all the factors used while the use of the standard

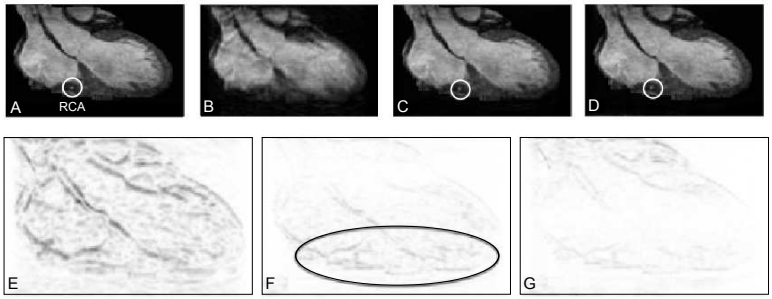


Figure 4.10: By getting the coronal slice of the 3D image, the effect of respiratory motion on image quality and visibility of the distal RCA can be shown (top row). The middle coronal slice of the reference data (A) was compared with the simulated scans without motion correction (B), with $CC_{upr}$ (C) and with $CF_{mean}$ (D). The image difference between the reference slice and simulated slice without correction (E), with $CC_{upr}$ (F) and with $CF_{mean}$ (G) are also shown.

Table 4.2: The average CNR values for the each correction factor used in the simulation and actual scans. The values for $CF_{upr}$, $CF_{mean}$ and $CF_{lwr}$ are 0.46, 0.51 and 0.56, respectively.

| | **Correction Factor** | | | |
|---|---|---|---|---|
| **Measure** | $CF_{upr}$ | $CF_{mean}$ | $CF_{lwr}$ | 0.6 |
| Simulation | 299.22 | 340.24 | 293.11 | 192.46 |
| Clinical | 191.22 | 191.86 | 155.80 | 130.90 |

correction factor (0.6) gave the worst. This trend is consistent for both the simulation and the actual scans as shown in Fig. 4.11b. Table 4.2 summarizes the mean CNR values for the four different correction methods used. Acquisitions using the mean correction factor showed the highest CNR for both the simulation (340.22) and the actual scan (191.86).

The same observation is applicable to the results of the vessel edge definition measurements (Fig. 4.12. The trend in the simulation scan showed high correlation with that of the clinical scans ($P = 0.038$).

## 4.4. Discussion

A critical aspect of choosing a respiratory motion correction method or motion parameter is its impact on the resulting MR image quality. This is evident especially in the case of coronary imaging like CMRA where a small difference in the respiratory gating can have adverse effects in the detection of lesions or blockages. However, the comparative effectiveness of the available correction methods is difficult to evaluate using actual MR scans. This is due to the difficulty in obtaining a ground truth, an assessment not effected by other sources of artifacts like cardiac cycle or magnetic field noise. Thus, we proposed an alternative, to use simulation as a tool and realistically recreate the data acquisition process during an MRI scan. The results of the experiments demonstrated that the simulation platform can be used to induce respiratory motion in the image and simulate the application of different motion correction methods.

The image-quality measures showed the effects on image quality of the respiratory motion correction factors used. These factors are translation coefficients simulating the use of the subject-specific navigator-guided techniques, which are prevalent in clinical CMRA scans. If the SI motion of the heart due to diaphragm motion is significantly less than 0.6, using the standard correction factor overestimates the motion, thus increasing the induced motion and decreasing image quality. This poses a significant drawback of using the same correction factor for all patients since in cases of minimal respiratory motion, it adds rather than correct motion. Additionally, the increase from the uncorrected data in terms of SNR (P=0.0091), CNR (P=0.0009) and vessel edge definition (P=0.0087) is highest when using the mean correction factor.

Aside from the dominant SI motion during respiration, displacement in other directions was also observed. However, the measured values from the volunteer scans were very small compared to SI motion. The measured right-left (RL) $CC$ also have low correlation with diaphragm motion (average $R^2$<0.4). This may be due to the fact that our tracking method is not robust enough to locate the specific ROI edge as it moves in the SI direction. Unlike the case for the tracking the horizontal edge in the SI direction, tracking the vertical edge as it moves in the RL direction presents more challenges because of the dominant SI movement. We plan to improve on the robustness of our tracking method in order to provide

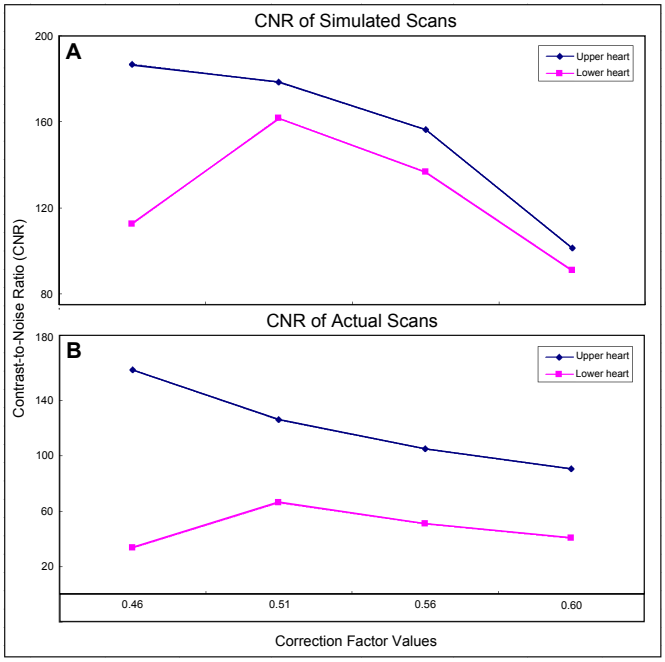


Figure 4.11: Contrast-to-noise ratio (CNR) measurements for the simulation and acquired clinical scans. The CNR was measured for both the upper and lower part of the heart. The trend of the CNR measurements were consistent for both the simulation and actual scan. The scan acquired using the mean correction factor ($CF = 0.51$) gave the highest average CNR between upper and lower heart CNR values while the standard correction factor ($CF = 0.60$), which is higher than the measured upper ($CF = 0.46$) and lower ($CF = 0.56$) factors, gave the lowest.

a more accurate estimation of correlation coefficients.

Using the platform for CMRA scans with the prospective 1D respiratory motion correction method may help in improving output image quality. A clinician can test different $CF$ values in the simulator and determine which one would be the most suitable for a certain subject or patient. This subject-specific $CF$ can then be used to replace the standard correction factor to acquire a better-quality CMRA image.

The current modelling of respiratory motion involves the tracking of 2D motion only. Tracking the 3D motion is also possible although it would present challenges because two planes has to be tracked (coronal and sagittal). The 3D compensation may also be impractical to implement in most scanners.

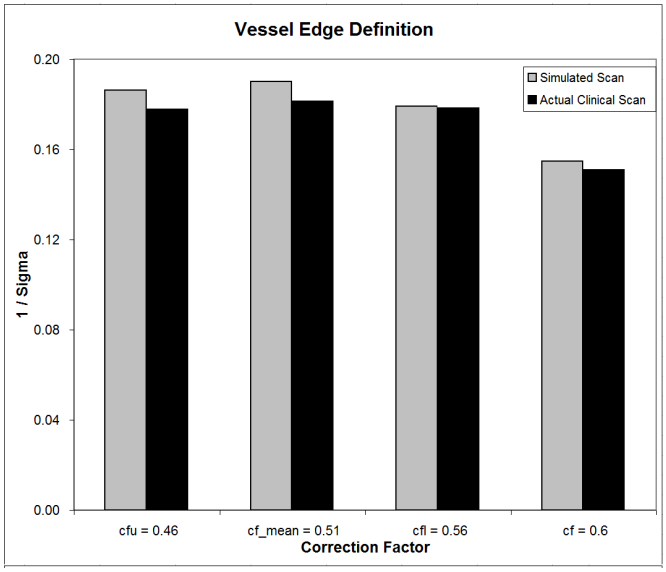


Figure 4.12: The vessel edge definition measurements for the simulation and actual clinical scans. The trends show a high correlation between the simulated and actual results ($P = 0.038$).

The hardware capability of MR scanners is still one of the main restrictions in the implementation of respiratory correction methods. Different models from different manufacturers offer varying technical challenges in addressing motion artifacts from respiration. For this reason, self-gating methods using image-based tracking are gaining acceptance since it can be applied to most MR scanners without significant hardware changes. Future work will include the evaluation of these self-gating approaches and also further validation using additional clinical MR scans.

## 4.5. Conclusion

This study demonstrated an overview of a simulation platform for MR respiratory motion correction. The model can be used to evaluate different motion correction techniques without the need to perform actual scans, which are subject to other sources of image artifacts aside from respiratory motion. The results of the simulation experiments showed high correlation with those of the actual scan.

This reflects the capability of the simulation platform to recreate the effects of respiratory motion in CMRA scans. The system also allows the flexibility to test different parameter estimation algorithms and MR $k$-space image reconstruction methods.

The simulation platform can be used to generate simulated scans for different respiratory motion parameters. The resulting scans can then be compared using a quantitative approach to measure their image quality and the visibility of coronary arteries. The subject-specific parameter that gives the highest image quality may be used in an actual CMRA scan to give a good-quality image of the coronary artery.

Although the simulator functions well in its current state, several issues remain to be addressed. Additional parameter estimation and more advanced $k$-space reconstruction techniques would be useful. Furthermore, there are many possible improvements that could help improve the overall realism of the output. With more features, we are confident that this simulator can be modified to evaluate a wide variety of cardiac motion correction algorithms.

# Chapter 5

# Intensity Standardization

## 5.1. Introduction

The acquisition of scout cine scans is important in determining the subject-specific motion of the heart during respiration. In the method discussed in the previous sections, the respiratory motion of the heart is determined by tracking the edge of the diaphragm and the endocardium. This requires a consistent contrast between the liver and air for the diaphragm and blood and endocardial wall in the heart to have a good approximation of the heart motion. If the contrasts in the cine images are not consistent, it might have adverse effects on the estimation of the correction factor.

Unlike CT scan, MRI does not have a predefined intensity ranges for different anatomical regions. There are no defined intensities for the myocardium, epicardium or the blood inside the heart chambers. Different scanners may result to different intensities for the same region of the heart. In the case of acquiring scout scans for CMRA, cardiac and respiratory motion can also affect image intensity distributions. These differences in the intensities between image slices for the same anatomical is referred to as intensity variations.

To address the problem of intensity variations in the MR scans, we proposed a method to standardize the intensity distributions for all the slices in the acquired scan. The following sections give the details of the intensity standardization. We used diffusion-weighted MR imaging (DWI) for the test images since it is one of the imaging techniques that is highly susceptible to intensity variations. Intensity

variations are more observable in DWI than in SSFP scans, which is used for the motion tracking.

### 5.1.1 Intensity Standardization

The visualization and analysis methods of MR images requires the use of certain parameters. The one possible exception would be if the assessment is done by manual method wherein the human knowledge can be thought of as parameters. However, manual assessment such as the segmentation results of two physicians can differ significantly because of factors like differences in their training or their analysis. Observer bias is impossible to remove when using manual observation. It is also time-consuming and less feasible when it is used to evaluate a large number of scans. Setting the values of the parameters for an automated method, on the other hand, becomes difficult without the same protocol-specific intensity meaning. There is a need for the intensities to be the same for each tissue class during automated visualization and analysis to ensure efficiency and this can be achieved using intensity standardization.

Intensity standardization has very important applications in a variety of medical imaging applications such as disease diagnosis, image segmentation, registration, and quantification [96, 97, 98]. It is especially crucial in studying MR data since MR image intensities do not possess a specific tissue assigned to it even in images acquired for the same subject, on the same scanner, for the same body region, and using the same pulse sequence [99]. It can also improve the analysis of data affected by motion such as cardiac imaging, where signal intensity variations can arise from respiratory motion or residual cardiac wall motion. In the study of myocardial infarct in patients, Fisher et al [100] observed that there are variations of signal intensity across the myocardium that is not indicative of a damaged myocardium. This problem may pose restrictions in the evaluation of cardiac wall and viability since quantitative image analysis of the heart such as segmentation and registration depends mostly on uniform intensity values for normal and infarcted tissues.

Previous attempts have been made to calibrate MR signal characteristics during acquisition using phantoms [101, 102]. The real-time calibration though, entails additional acquisition requirements that can complicate the imaging and

increase scan time. Therefore, an alternative that uses post-processing can be more attractive because such methods would not only make acquiring images simpler but also make it possible to process the already acquired data. A number of algorithms were developed to deal with bias field correction after data acquisition [103, 104]. However, these methods do not solve the problem of assigning specific meaning to image intensity values. Thus, a certain intensity value of the same or different patient cannot be associated to a specific anatomical meaning and standard presets cannot be used to visualize certain organs or tissues. These reasons lead to other studies that deal with inter-scan intensity standardization.

Some of the first published intensity standardization methods made use of 1D histograms [105]. The basic idea is to find a mapping of landmarks that deforms the intensity histogram of an input image so that it matches that of a reference histogram. First, they detected landmarks based on percentiles on the input and reference histograms. Then a continuous intensity mapping was created by doing linear interpolation between respective landmark points. Another histogram-based method was proposed by Hellier [106], where a mixture of Gaussians was estimated to get the histogram. The fitting was done by aligning the mean intensities of the tissues. This approach, however, is only applicable to the head region and highly dependent on the Gaussian fit.

Jager et al [107] introduced the use of joint histograms for intensity standardization. The normalization was achieved by finding a deformation of the joint histograms between two sets of images while minimizing a distance measure. Each of these histograms is at least two-dimensional and contains the information of two or more MRI sequences. The method treated the process similar to a nonrigid image registration, where the joint histograms serve as the input and reference images. However, this approach was only done on T1- and T2-weighted sequences, which almost has the same spatial features. The study has not also been conducted on a pair of sequences with a large difference in spatial features and the number of gray values such as the one between diffusion-weighted and T2-weighted images.

### 5.1.2 Diffusion-weighted MR Imaging

Magnetic resonance imaging offers some major advantages compared to other modalities. One of this is its ability to discriminate between tissues using their physical and biochemical properties. Diffusion-weighted MR imaging adds to conventional MRI the capability to probe the tissue structure at a microscopic scale through the movement of water molecules. The motion of the water molecules are influenced by the physical orientation of tissue structures and the concentration of cells in which they are part of. Figure 5.1 shows how the concentration of cells affects the magnitude of water diffusion. Consequently, in tissues with large number of fibers such as cardiac and brain matter, the water diffusion moves fastest along the fiber length orientation and slowest in the direction perpendicular to it. In tissues with few fibers, water moves nearly isotropically. The capability of DWI to image how water diffuses in tissues provides an intricate 3D representation of tissue composition, architecture, and organization. Additionally, changes in these tissue properties can be attributed with processes that occur in their development, degeneration, disease and aging [108, 109]. Gupta et al [110] used DWI to search and quantify the extent of lesions seen on the T2 and fluid-attenuation inversion recovery (FLAIR) images in patients with chronic traumatic brain injury with and without epilepsy. It has also been shown that DWI can help determine the malignancy of tumors [111]. Koh et al [2] demonstrated the use of whole-body DWI for tumor detection and characterization and for the monitoring of response to treatment. They have also shown its ability to predict treatment response to chemotherapy and radiation treatment.

The diffusion of water molecules in tissues over time interval $t$ can be described by a probability density function $p_t(\mathbf{r})$, which gives the probability of water diffusing by r. Since $p_t(\mathbf{r})$ is largest in the direction of least resistance and smaller in other directions, the information about the density function reveals the fiber orientation of the tissues.

The DWI echo signal $s(\mathbf{q})$ can be computed from the density function $p_t(\mathbf{r})$ through Fourier transformation (FT) with respect to the sensitizing gradient $\mathbf{q}$ by

$$s(\mathbf{q}) = s_0 \int p_t(\mathbf{r}) e^{-i\mathbf{q}\cdot\mathbf{r}} d\mathbf{r}, \tag{5.1}$$

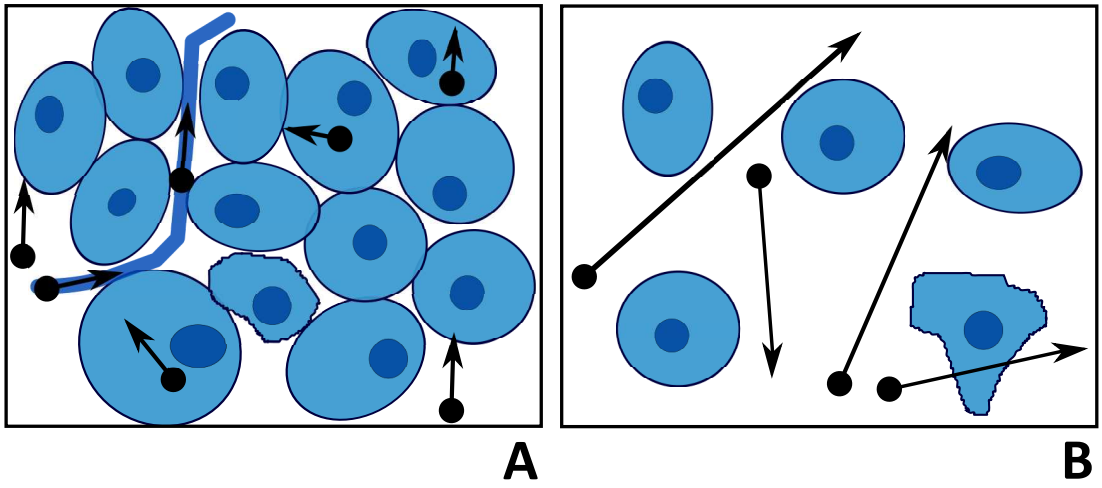


Figure 5.1: The difference in magnitude of water diffusion in a high (A) and low (B) cell concentration environment. The water molecules (black circles with arrows) within extracellular space, intracellular space and intravascular space all contribute to the measured MR signal. In the less cellular environment, the relative increase in extracellular space allows freer water diffusion than in a more compact environment. Defective cell membranes (B) also allow movement of water molecules between extracellular and intracellular spaces.

where $s_0$ is the MR signal in the absence of any gradient. Therefore, $p_t(\mathbf{r})$ can be estimated from the inverse FT of $s(\mathbf{q})/s_0$.

The sensitivity of the DWI sequence to water molecule motion can be varied by changing the gradient amplitude, the duration of the applied gradient, and time interval between paired gradients. On clinical scanners, the diffusion sensitivity can easily be changed by modifying the parameter known as the b value, which is closely related to the gradient amplitude. Water molecules with a large degree of motion or a large diffusion distance will show signal attenuation with small b values (e.g. b = 50-100 s/mm$^2$). By contrast, large b values (e.g. b = 1000 s/mm$^2$) are usually required to image slow-moving molecules or small diffusion distance since these show more gradual signal attenuation with increasing b values.

DWI is typically performed using at least two b values (with $b_0$ = 0 s/mm$^2$ and other b values from 1 to 1000 s/mm$^2$) to enable meaningful interpretation. The attenuation of signal intensity on images obtained at different b values gives

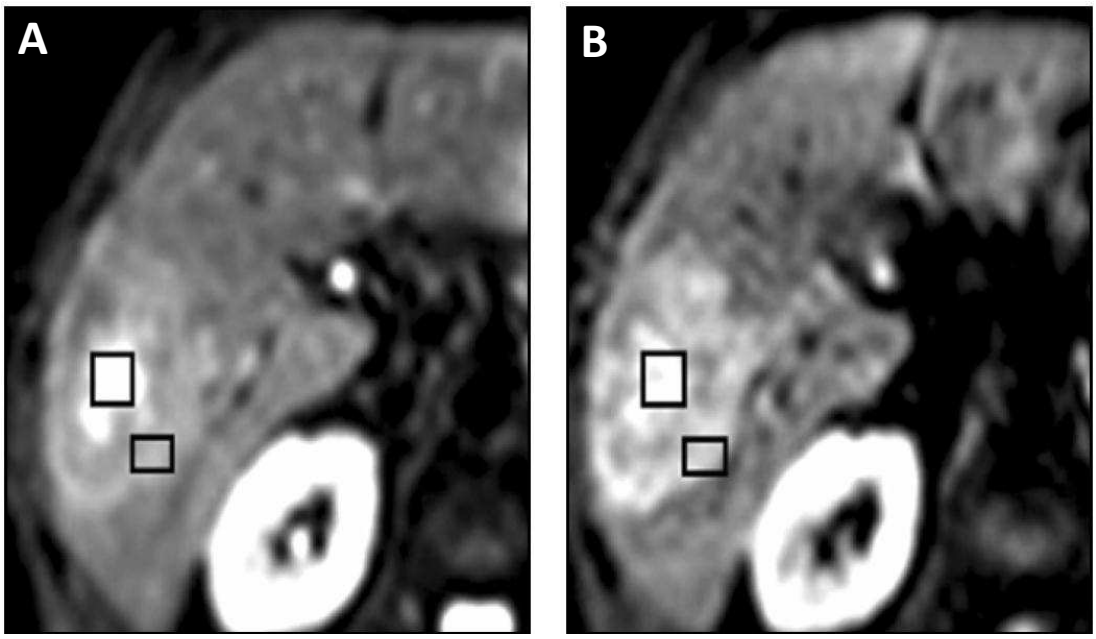


Figure 5.2: An example of a diffusion-weighted MR images containing liver metastasis. The images are obtained at different b values show large heterogeneous metastasis within right lobe of liver. Necrotic center of metastasis (squares) shows attenuation of signal intensity with increasing b values, indicating less restricted diffusion. By comparison, rim of tumor (rectangles) is more cellular and shows little signal attenuation with increasing b value [2].

the characterization of tissue water diffusion. For instance, in a heterogenous tumor, the more necrotic fraction of the tumor will show more signal attenuation on high b-value images because water diffusion is less restricted. Conversely, the more solid tumor areas will show relatively high signal intensity (Fig. 5.2).

One of the pitfalls of using DWI, as with other MR protocols, is that it suffers from severe magnetic inhomogeneities that result to intra-scan intensity variations for the same tissues. This is apparently more so when imaging the abdomen using single shot echo planar imaging (EPI) sequence, which gives images with low signal-to-noise-ratio. The EPI technique allows the DWI of the abdomen with fast imaging times minimizing the effect of gross physiologic motion from respiration and cardiac cycle. However, EPI images has the limitations of low resolution in addition to susceptibility artifacts from field inhomogeneities. This

makes the image intensity corrections even more difficult for DWI images acquired using EPI.

The contribution of this paper is the standardization of DWI images using joint histograms. The joint histogram is composed of DWI and T2 image. The method is the only approach that deals with abdominal DWI scans. In addition, even though T2 images were used jointly with DWI images, other protocols can also be used. The introduced method is independent of the region of interest and can further be applied to whole body DWI.

The standardization of the DWI images are done as an initial step in the registration of DWI and T2-weighted abdominal images. The acquisition of abdominal DWI is limited by the motion artifacts contributed by the respiratory and cardiac cycle. The ultra-fast EPI acquisition itself cannot account for the very sensitive nature of gradient sensitivity that the intensity standardization after the acquisition of DWI images is crucial in overcoming the low signal-to-noise ratios.

## 5.2. Method

The intensity standardization involves the mapping of the intensities of a set of paired current images $U = (U_{T2}, U_{DW})$, where the paired images are acquired using T2-weighted and diffusion-weighted imaging, respectively. This set of input images is mapped into a reference pair $R = (R_{T2}, R_{DW})$ so that a same tissue class in both sets will have the same intensity value. The mapping can be achieved by the minimization of the distance between the probability density function (pdf) of the joint histogram of the two pairs of images [107]. Since DWI images suffer from low signal-to-noise ratio and cover a fewer number of gray values compared to other MR protocols (e.g. T2), no complete registration of the joint histogram pdfs is possible (i.e. the difference can not be zero). This is also true because the volume and anatomical information of tissues differ for interpatient as well as intrapatient measurements. When the joint histograms are treated as images, the process can be treated as a non-rigid image registration. Ideally, we are looking for a transformation $u$: $\mathbf{R}^d \rightarrow \mathbf{R}^d$ such that the reference image $p_R$ and input image $p_U$ are similar regarding a certain distance measure $D$.

### 5.2.1 Data Acquisition and Joint Histogram Computation

Two sets of 3D coronal abdominal scans were acquired using T2-weighted imaging and DWI for six subjects. Both of the scans has an FOV of 50 cm × 34 cm (RL × SI) with 66 slices of 3.5 mm thickness. The matrix size for the T2 data is 192 × 320 and 144 × 98 for DWI, which were interpolated into 472 × 320 and 144 × 98, respectively. This means that the interpolated dataset for T2 images has a slice thickness of 1.1 mm while the DWI retains its 3.5 mm thickness. The volumes were acquired in interleaved mode with odd and even slices. The T2 images were automatically reordered and unified as a single volume while the DWI images were stored separately for odd and even folders. In terms of spatial location, the first and second slice of the T2 volume dataset corresponds to the first slice of the odd and first slice of the even DTI volume, respectively.

The T2 images were obtained using Fast Spin Echo (FSE) sequence in free breathing with TR = 4200 ms, TE = 90 ms, and parallel factor of 2. The DWI images were acquired using DSE-EPI with TR = 5000 ms and TE = 75 ms, and parallel factor of 2. For the DWI data, volumes were acquired for b = 0 s/mm$^2$ ($b_0$) and b = 1000 s/mm$^2$ ($b_1000$). The T2 and DWI sequences were done in a 1.5T Excelart Vantage$^{TM}$ MRI scanner (Toshiba Medical Systems, Tochigi, Japan).

As seen in the images in Fig. 5.3, the distortion of the $b_0$ and $b_{1000}$ is severe compared to the T2 images. The distortion is brought by two main factors, namely, the EPI acquisition and the diffusion weighting of b = 1000 s/mm$^2$. The majority of the distortion though comes from EPI. There is not much tissue data in the $b_0$ and the noise in $b_{1000}$ overlaps with the detected tissue diffusion. This prompted us to use only the $b_0$ together with the T2 images for the intensity standardization.

Once the data volumes were acquired, an arbitrary patient data was chosen as a reference and the rest were assigned as the input datasets that need to be intensity standardized to the reference. The joint histogram $H(a, b)$, where entry is the number of times an intensity a in one image corresponds to intensity b in the other, was computed for the reference pair and the input pairs. For the reference histogram, $H(R_{T2}(i), R_{DW}(j))$ denotes the number of occurrences when the reference T2 pixel is gray level $i$ and the corresponding DWI pixel is $j$.

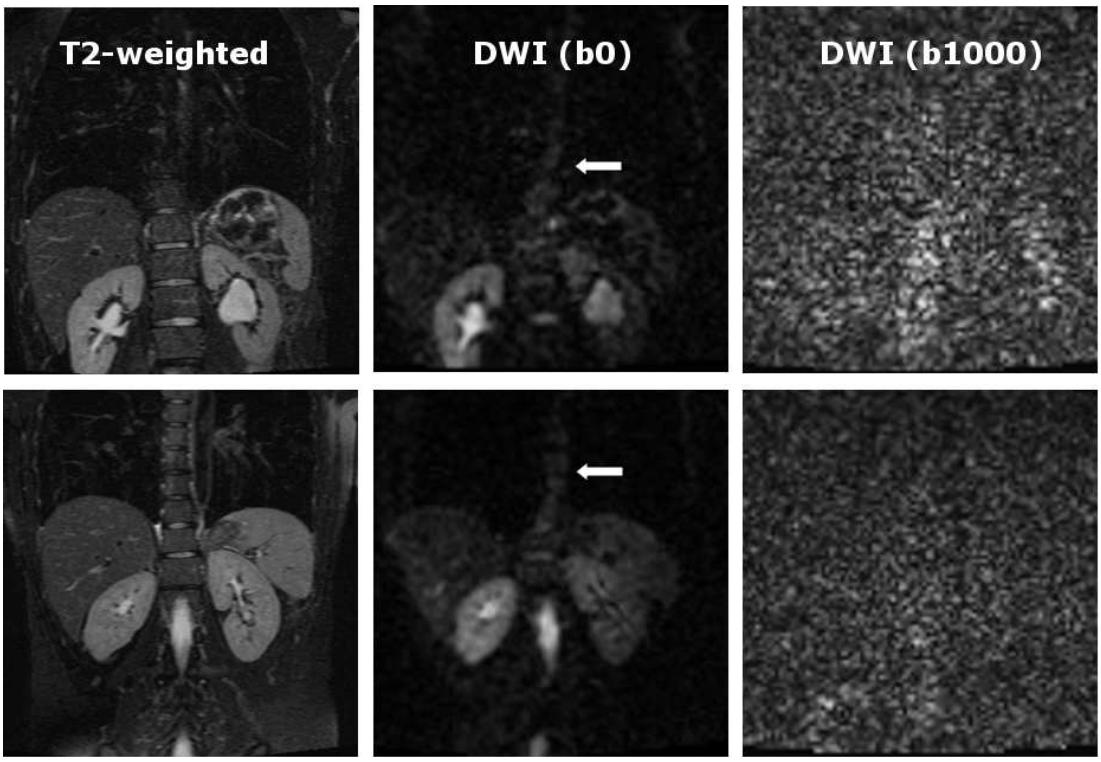


Figure 5.3: The abdominal T2, DWI $b_0$ and $b_1000$ images for subject 3 (top) and subject 5 (bottom). The DWI images are distorted, especially the images where b = 1000 s/mm$^2$ (b1000). There are spatial distortion with the b0 images as indicated by the presence of the curved spinal column (arrows).

Therefore, the reference joint histogram density function $p_R(i,j)$ can be solved by

$$p_R(i,j) = \frac{H(R_{T2}(i), R_{DW}(j))}{n \times m} \quad 0 \leq i < K \mid 0 \leq j < L \tag{5.2}$$

where n $\times$ m is the total number of pixels, K and L are the total number of gray levels in the T2 and DWI image, respectively. A similar computation was done to get the density function $p_U$ of the input images.

Prior to registration, pre-processing of the images and joint histograms was done to improve the results of standardization. The image intensities were scaled due to the large difference in the number of gray values between T2 and DWI images. Combinations of background pixels in which both gray values in the joint histogram bin are less than 10 ($i, j < 10$) were also removed by applying

a threshold to the joint histogram range. Finally, outliers were removed that resulted to about 98% of histogram points being used.

To make the method independent from anatomical and histogram shape differences, the whole joint histogram volume was divided into partitions. Each partition has equal number of joint histograms, which were added together to form one histogram. The sum was then divided by the total number of histogram points to get the joint histogram average of each partition. Figure 5.4 illustrates the partitioning done on the joint histogram data.

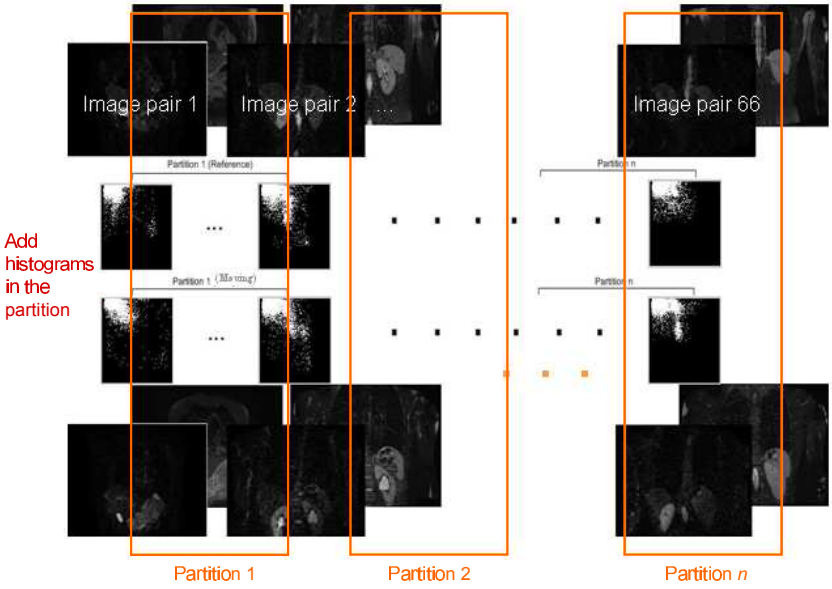


Figure 5.4: Partitioning of the series of input (moving) and reference histograms into sets. The joint histograms were derived from the image pair of T2 and DWI images and have a total of 66 each for the input and reference. The 66 joints histogram is divided into $n$ number of partitions (e.g. $n = 3$) and all the histograms in the partition are added together.

All experiments were conducted on the Matlab 7.4 environment on a Dell Precision T3400 workstation. For the curvature-based registration, the Matlab classes from Flexible Algorithms for Image Registration (FAIR) were used.

### 5.2.2 Intensity Standardization

The search for gray scale value mapping during intensity standardization can be treated as an image registration. Image registration can be summarized as the problem of finding an optimal geometric transformation between a reference image $A$ and input image $B$ so that the transformed input image is similar to the reference with respect to a distance measure $D$. Here, we assigned the reference image $A$ to the pdf $p_R$ representing the two-dimensional density function of $R$ and similarly $B = p_U$, the density of $U$.

For the distance measure, sum of squared distances (SSD) is sufficient enough to be used in this paper since the function values of both pdfs have equal meaning. The registration problem can be solved using the approach introduced by J. Modersitzki [112] and formulated as

$$T[p_R, p_U; u] = D[p_R, p_U; u] + \alpha S[u], \tag{5.3}$$

where $S$ represents the smoother and the factor $\alpha$ defines the influence of the smoother on the objective function. The smoother used in this paper is a curvature-based regularizer, also introduced in [112]. The distance measure based on SSD can be computed by

$$D^{SSD}[p_R, p_U; u] = \frac{1}{2} \int_{\Omega} (p_U(i) - p_R(i))^2 di. \tag{5.4}$$

It calculates the distance between the functions relative to their function values at a position $i$, with $\Omega = [0, 1]^n$ representing the image domain.

The curvature-based smoother is defined by Neumann boundary conditions and can be expressed by

$$S^{curv}[u] = \frac{1}{2} \sum_{l=1}^{n} \int_{\Omega} (\Delta_{ul})^2 dx, \tag{5.5}$$

with $\Delta$ as the Laplacian operator. A Gateaux derivative has to be applied to the objective function $T$, which is a first-order variational problem. The optimization problem can then be solved using Euler-Lagrange resulting to

$$dS^{curv}[u] - f^{SSD}(i, u(i)) = 0 \quad \text{for all} \quad i \in \Omega. \tag{5.6}$$

The desired result of the optimization problem is the deformation function $u$: $\mathbf{R}^d \rightarrow \mathbf{R}^d$. Likewise, the technique used is multi-level, matrix-free image registration. The whole method can be summarized by the following steps:

**Input**: Given two pairs of T2 and DWI images, $U_{T2}$ and $U_{DW}$ for input pair and $R_{T2}$ and $R_{DW}$ as reference.

**Output**: The deformation or mapping function $u$ between the input images or a lookup table (LUT) that stores the standardizer $\tau_P$.

1. Compute the joint histogram $H_U$ and $H_R$.
2. Separate the series of joint histograms into a number of partitions to normalize and reduce the number of registrations.
3. Determine the intensity density function $p_U$ and $p_R$ from the joint histograms.
4. Calculate the distance measure $D^{SSD}$.
5. Register $p_U$ to $p_R$ while minimizing $T[p_R; p_U; u] + \alpha S(u)$.
6. Map the intensity value of every pixel pair in $p_U$ using the deformation function $u$ to get the output mapping in an LUT $\tau_p$.

## 5.3. Results

The experiment was evaluated using partitions in the PI direction of the histogram dataset. All the joint histograms in the partition were added together and the pdf of the total was computed. There were different number of partitions used to determine which one offers the most reduction in the difference between the input pdf and the reference. Each reference and its corresponding current partition were registered independently. An sample partitioned pdf set where the total data pdf were divided into 6 partitions is shown in Fig. 5.5. The figure shows the difference in the concentration of the joint histogram, indicating

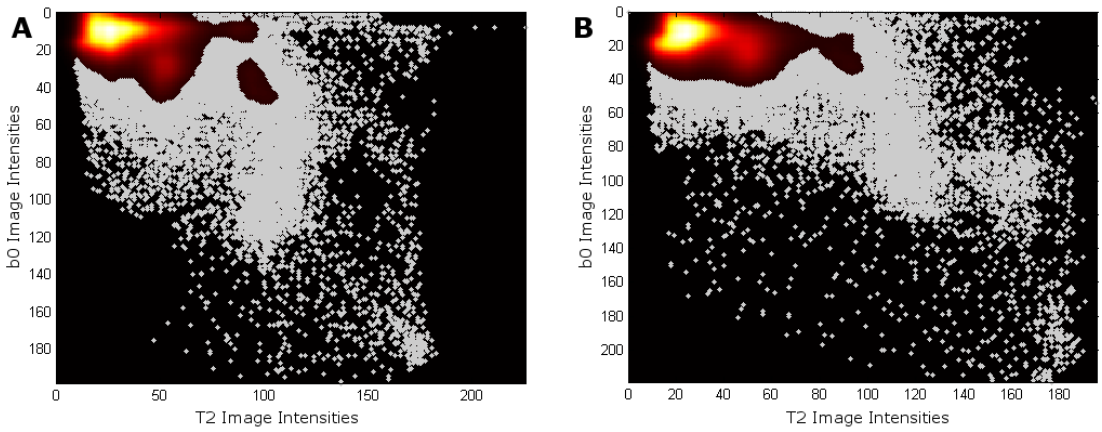


Figure 5.5: The reference (A) and input (B) probability density function (pdf) of the summation of histograms using six partitions. These pdfs belong to the fourth partition (summation of joint histograms 34-44).

the intensity variations between input and reference images. Different number of partitions was used in the evaluation.

To compute the effect of registration on the input histogram, its difference with the reference histogram was computed using SSD. The SSD distance is expressed as $d$. The smaller the difference means that the registration made a better transformation of the input histogram to fit that of the reference, meaning a more effective intensity standardization. The large anatomical differences and large deformations in the DWI images make voxel-wise evaluation not ideal. Instead, the quality measure used was the relative distance between the reference and the current histogram before and after standardization. The measure $q$, is expressed as

$$q = \frac{d_{after}}{d_{before}} \times 100 \tag{5.7}$$

where $d_{before}$ and $d_{after}$ are the distance between input and reference histogram before and after registration, respectively.

Figure 5.6 shows the graph of relative distance between input and reference pdf with respect to the number of partitions. Six number of partitions were tried, 1 combined data, 3, 6, 9, 11, and 15 partitions. The one where all the data were combined in one partition gives the biggest difference between input and reference pdf, thus the biggest intensity variations. The difference was almost 75%. The 3

and 6 partitions, on the other hand gives the best intensity standardization result with only 41% relative distance between input and reference pdf.

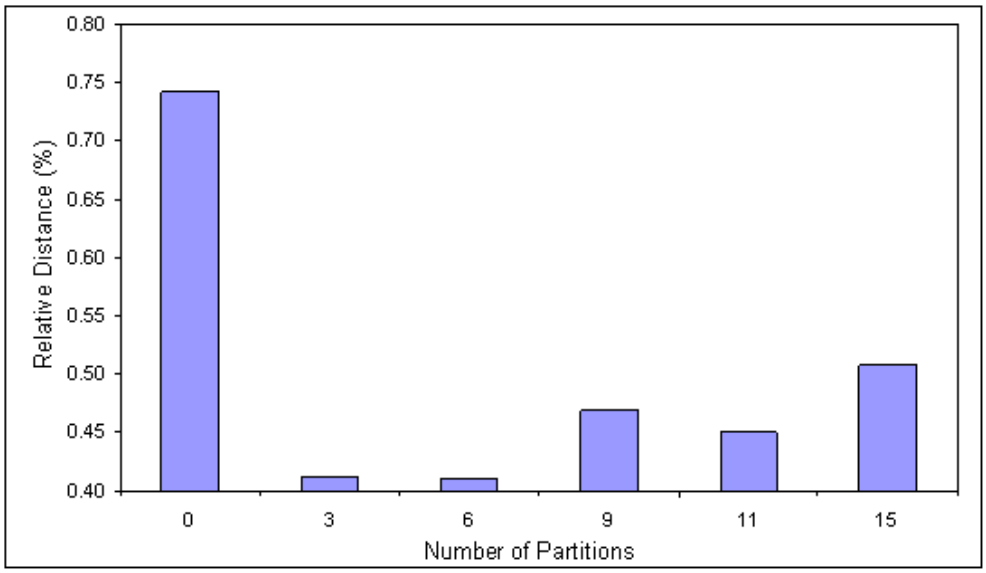


Figure 5.6: The graph shows the relative distance between the reference and current histograms with respect to the number of standardization partitions used in the intensity standardization. The optimal number of partitions (i.e. one with least difference) are 3 and 6. This means the use of 3-6 partitions offer the most similarity between input and reference pdf after image registration.

## 5.4. Discussion

The method used for inter-slice intensity variation reduction used the combined histogram of a pair of images instead of using a single reference or input image. It also uses spatial information between the set of images to estimate the linear mapping between the intensities of the adjacent slices. In intensity standardization, the common problem that complicates its application is the task of getting the corresponding locations between the input image and the reference. With the use of joint histogram, however, the two sets of images for the same patients give the same location for tissues and organ. Thus, the joint histogram includes the unique correspondence of a tissue class in T2-weighted and DWI images. This

correspondence incorporates a spatial information on the tissues and organs characterized by those intensity level combinations. It can then be used to correct intensity variations in other scans without having to align landmarks in the input images and the corresponding template images.

The results of the experiment show that it is best to use between three to six partitions to get the optimal intensity standardization. Increasing the number of partitions will make the estimation of pdfs unreliable. On the other hand, fewer partitions means the standardization is affected by inhomogeneities and small structures are bypassed in the registration.

The use of SSD as distance measure made it possible to reach a relative distance of $q = 0.4122$ as shown in Fig. 5.6. This means an almost 60% reduction in the distance between the joint histograms. Achieving higher results, on the other hand is not possible due to the anatomical differences between datasets and the deformations present in the DWI images.

With this method, it is possible to make the intensities of the heart anatomical regions consistent for all slices in the cine scout scan. This can improve the accuracy of the automatic computation of the subject-specific respiratory correction factors to be used in the CMRA scan.

# Chapter 6

# Conclusion

Coronary MR angiography presents a non-invasive and efficient way of detecting blockages and lesions in the coronary artery. This capability can help detect the severity of the coronary artery disease and aid physicians in giving diagnostics. However, CMRA does not come without its limitations. Respiratory motion during scan can produce artifacts that adversely affect the quality of the CMRA scan. Consequently, the visibility of the coronary artery and its lesions are also affected. To address this, this paper discussed methods that can help minimize the effects of respiratory motion. The first solution is the use of subject-specific correction factors from the tracking of the heart motion. The second is the use of a simulation platform to evaluate different respiratory motion correction methods and their effect on the CMRA acquisition. With the simulation platform, it is possible to evaluate the correction methods without the effects of other sources of image artifacts like cardiac cycle or magnetic inhomogeneities in the MR scanner.

## 6.1. Subject-specific Respiratory Motion Correction

The use of navigator gating to correct for respiratory motion in CMRA scans is one of most commonly used techniques by clinicians today. However, most scans rely on the use of a fixed correction factor that assumes that the SI motion of the heart is a factor 0.6 of the diaphragm motion. This fixed correction factor does

not take into account the motion variations between patients. The acquisition of a patient-specific correction factor offers a more accurate way of estimating the respiratory motion of the heart. We presented a method to estimate the upper and lower heart correction factor by tracking the upper and lower endocardium, respectively. Results showed that using the average of these two correction factors gives the best image quality compared to using either of the two or the fixed correction factor commonly used in clinical scans.

## 6.2. Respiratory Motion Correction Simulation Platform

This study demonstrated a simulation platform that can be used to simulate respiration-induced cardiac motion and the subsequent respiratory gating. The simulation was done to compare the effectiveness of different respiratory motion correction methods and the use of different motion correction factors or parameters. The initial part of the study confirmed that there is intersubject variability in heart motion. There is also a significant difference in the motion of the upper and the lower heart during respiration. The simulation platform was used to evaluate the effects of using the correction factors acquired in the cine scan and other respiratory motion correction methods like the affine motion correction. The actual acquisition of a CMRA scan and motion correction is simulated for all the methods. The simulation platform includes a set of image quality assessments to quantitatively measure the resulting scan for each correction method. This enables the evaluation of different respiratory motion correction methods without other sources of motion artifacts. Comparison of the image quality results for different correction parameters shows good correlation between the results of the simulated scans and that of the actual CMRA scan. The simulation and subsequent quantitative comparison allows for the estimation of subject-specific respiratory motion correction parameters that can be used in an actual CMRA scan.

## 6.3. Future Work

Although the software and implementation are sufficient for the objectives described above, there are some additional features that will be added for this study. For the subject-specific tracking of the heart, a 2D motion estimation from the cine images is desired. A non-rigid image registration of the cine slices to estimate the motion between slices will be added as one option in the heart motion tracking. For the simulation platform, a number of k-space image reconstruction techniques will also be added, including the most commonly used techniques in commercial MR scanners. However, since these techniques are proprietary, the implementation of the exact algorithms will not be possible. The basic techniques are described in publications and can be implemented in the simulation platform. Finally, a user interface will be developed for users to easily choose and design their simulation experiments.

# Acknowledgements

ad maiorem + Dei gloriam

St. Ignatius of Loyola

First, I would like to thank God for bestowing me with His blessings and inspiring me to persevere. His lessons gave me the courage to do things not only for myself but also for the greater good of others and His greater glory.

I'm very grateful to my family for the inspiration and showing utmost patience with me. I may not be with them during my graduate studies but they are always in my heart and in my mind. Their stories bring joy to me and make being away from home more bearable.

I also want to thank my friends, especially Raula and Cecilia for sharing all those memories of joys and challenges in my years in NAIST. Great would be an understatement to describe you as friends. Your advice and encouragement helped me a lot in completing this dissertation. Also, I wouldn't be in NAIST if not for the help of my *sempais* Edi, Jo, Albert, and Randy. Their guidance and wisdom proved invaluable in helping me cope with life in Japan and more importantly, life in general. And of course, many thanks to Emarc, Clare, JC, Akie, Jimson and Lyn for making NAIST feel more like home. As the saying goes, silver is expensive but friends are gold.

I would also like to extend my gratitude for Okada-*sensei* and Kuhara-*san* for their unwavering support during the duration of my research. Especially to Okada-*sensei*, who was always ready and willing to give valuable input during our research discussions. Kuhara-*san* and all of MR Department of Toshiba Medical Systems were a big reason for the completion of this research with their technical training and financial support.

In addition, I am grateful to my thesis committee members, Kanaya-*sensei* and Sugiura-*sensei*, whose review of my dissertation provided valuable insights and suggestions. This dissertation would not be complete without their contributions.

Last but not the least, I would like to thank my advisers Minato-*sensei* and Sato-*sensei*. Their guidance and patience is like light at the end of the tunnel for me. They were there from the moment I entered NAIST until the moment I completed my dissertation. I wouldn't be where I am now without their wisdom and graciousness. For all of that I offer a big *arigatou gozaimasu*.

# Publication List

## Journal

1. F.R. Punzalan, T. Sato, T. Okada, S. Kuhara, K. Togashi and K. Minato, "Respiratory Motion and Correction Simulation Platform for Coronary MR Angiography." *IEICE Transactions on Information and Systems.* vol. E96-D, no. 1, pp. 111-119, January 2013 (Chapters 1, 3–4)

## International Conferences

1. F.R. Punzalan, T. Sato, T. Okada, S. Kuhara, K. Togashi and K. Minato, "New Approach for Patient-specific Estimation of Cardiac Motion due to Respiration." *Proceedings of ISMRM-ESMRMB Joint Annual Meeting 2010 (Abstract 2819).* vol. 17, May 2010. (Chapters 1, 3–4)

2. F.R. Punzalan, T. Sato, T. Okada, S. Kuhara, K. Togashi and K. Minato, "Joint Histogram-based Intensity Standardization of Diffusion-weighted MRI Images." *IFMBE Proceedings - World Congress on Medical Physics and Biomedical Engineering.* vol. 29, September 2009. (Chapter 5)

## Domestic Conferences

1. F.R. Punzalan, T. Sato, T. Okada, S. Kuhara, K. Togashi and K. Minato, "Affine Motion Parameter Estimation for Respiratory Motion Correction in Coronary MRA." *Proceedings of Biological and Medical Engineering Symposium, September 2010.* (Chapter 3)

# References


[1] J. Y. Moon, J. W. Chung, J. H. Kim, Y. K. Ahn, and M. H. Jeong. Simultaneous subacute stent thrombosis of two sirolimus-eluting stents in a patient treated by ReoPro, thrombus aspiration and triple anti-platelet agents. *Int. J. Cardiol.*, 130:e25–29, Oct 2008.

[2] D. M. Koh and D. J. Collins. Diffusion-weighted MRI in the body: applications and challenges in oncology. *AJR Am J Roentgenol*, 188:1622–1635, Jun 2007.

[3] P. Ammann, H. P. Brunner-La Rocca, W. Angehrn, H. Roelli, M. Sagmeister, and H. Rickli. Procedural complications following diagnostic coronary angiography are related to the operator's experience and the catheter size. *Catheter Cardiovasc Interv*, 59:13–18, May 2003.

[4] T. Batyraliev, M. R. Ayalp, A. Sercelik, Z. Karben, G. Dinler, F. Besnili, S. Ozgul, and I. Perchucov. Complications of cardiac catheterization: a single-center study. *Angiology*, 56:75–80, 2005.

[5] M. Naghavi, P. Libby, E. Falk, S. W. Casscells, S. Litovsky, J. Rumberger, J. J. Badimon, C. Stefanadis, P. Moreno, G. Pasterkamp, Z. Fayad, P. H. Stone, S. Waxman, P. Raggi, M. Madjid, A. Zarrabi, A. Burke, C. Yuan, P. J. Fitzgerald, D. S. Siscovick, C. L. de Korte, M. Aikawa, K. E. Juhani Airaksinen, G. Assmann, C. R. Becker, J. H. Chesebro, A. Farb, Z. S. Galis, C. Jackson, I. K. Jang, W. Koenig, R. A. Lodder, K. March, J. Demirovic, M. Navab, S. G. Priori, M. D. Rekhter, R. Bahr, S. M.

Grundy, R. Mehran, A. Colombo, E. Boerwinkle, C. Ballantyne, W. Insull, R. S. Schwartz, R. Vogel, P. W. Serruys, G. K. Hansson, D. P. Faxon, S. Kaul, H. Drexler, P. Greenland, J. E. Muller, R. Virmani, P. M. Ridker, D. P. Zipes, P. K. Shah, and J. T. Willerson. From vulnerable plaque to vulnerable patient: a call for new definitions and risk assessment strategies: Part I. *Circulation*, 108:1664–1672, Oct 2003.

[6] T. K. Foo, V. B. Ho, M. Saranathan, L. Q. Cheng, H. Sakuma, D. L. Kraitchman, K. C. Wu, and D. A. Bluemke. Feasibility of integrating high-spatial-resolution 3D breath-hold coronary MR angiography with myocardial perfusion and viability examinations. *Radiology*, 235:1025–1030, Jun 2005.

[7] R. R. Edelman, W. J. Manning, D. Burstein, and S. Paulin. Coronary arteries: breath-hold MR angiography. *Radiology*, 181:641–643, Dec 1991.

[8] T. S. Sachs, C. H. Meyer, B. S. Hu, J. Kohli, D. G. Nishimura, and A. Macovski. Real-time motion detection in spiral MRI using navigators. *Magn Reson Med*, 32:639–645, Nov 1994.

[9] J. N. Oshinski, L. Hofland, S. Mukundan, W. T. Dixon, W. J. Parks, and R. I. Pettigrew. Two-dimensional coronary MR angiography without breath holding. *Radiology*, 201:737–743, Dec 1996.

[10] M. Stuber, R. M. Botnar, P. G. Danias, D. K. Sodickson, K. V. Kissinger, M. Van Cauteren, J. De Becker, and W. J. Manning. Double-oblique free-breathing high resolution three-dimensional coronary magnetic resonance angiography. *J. Am. Coll. Cardiol.*, 34:524–531, Aug 1999.

[11] M. Weiger, P. Bornert, R. Proksa, T. Schaffter, and A. Haase. Motion-adapted gating based on k-space weighting for reduction of respiratory motion artifacts. *Magn Reson Med*, 38:322–333, Aug 1997.

[12] M. E. Huber, D. Hengesbach, R. M. Botnar, K. V. Kissinger, P. Boesiger, W. J. Manning, and M. Stuber. Motion artifact reduction and vessel enhancement for free-breathing navigator-gated coronary MRA using 3D k-space reordering. *Magn Reson Med*, 45:645–652, Apr 2001.

[13] K. McLeish, D. L. Hill, D. Atkinson, J. M. Blackall, and R. Razavi. A study of the motion and deformation of the heart due to respiration. *IEEE Trans Med Imaging*, 21:1142–1150, Sep 2002.

[14] Y. Wang, S. J. Riederer, and R. L. Ehman. Respiratory motion of the heart: kinematics and the implications for the spatial resolution in coronary imaging. *Magn Reson Med*, 33:713–719, May 1995.

[15] R. Ross. Cellular and molecular studies of atherogenesis. *Atherosclerosis*, 131 Suppl:3–4, Jun 1997.

[16] S. Glagov, E. Weisenberg, C. K. Zarins, R. Stankunavicius, and G. J. Kolettis. Compensatory enlargement of human atherosclerotic coronary arteries. *N. Engl. J. Med.*, 316:1371–1375, May 1987.

[17] H. C. Stary, A. B. Chandler, R. E. Dinsmore, V. Fuster, S. Glagov, W. Insull, M. E. Rosenfeld, C. J. Schwartz, W. D. Wagner, and R. W. Wissler. A definition of advanced types of atherosclerotic lesions and a histological classification of atherosclerosis. A report from the Committee on Vascular Lesions of the Council on Arteriosclerosis, American Heart Association. *Arterioscler. Thromb. Vasc. Biol.*, 15:1512–1531, Sep 1995.

[18] E. Falk and A. Fernandez-Ortiz. Role of thrombosis in atherosclerosis and its complications. *Am. J. Cardiol.*, 75:3B–11B, Feb 1995.

[19] Hurst W. *The Heart, Arteries and Veins. 10th ed.* McGraw-Hill, New York, 2002.

[20] World Health Organization. The top 10 causes of death. 2004.

[21] Z. A. Fayad and V. Fuster. The human high-risk plaque and its detection by magnetic resonance imaging. *Am. J. Cardiol.*, 88:42E–45E, Jul 2001.

[22] P. J. Scanlon, D. P. Faxon, A. M. Audet, B. Carabello, G. J. Dehmer, K. A. Eagle, R. D. Legako, D. F. Leon, J. A. Murray, S. E. Nissen, C. J. Pepine, R. M. Watson, J. L. Ritchie, R. J. Gibbons, M. D. Cheitlin, T. J. Gardner, A. Garson, R. O. Russell, T. J. Ryan, and S. C. Smith. ACC/AHA

guidelines for coronary angiography: executive summary and recommendations. A report of the American College of Cardiology/American Heart Association Task Force on Practice Guidelines (Committee on Coronary Angiography) developed in collaboration with the Society for Cardiac Angiography and Interventions. *Circulation*, 99:2345–2357, May 1999.

[23] T. J. Noto, L. W. Johnson, R. Krone, W. F. Weaver, D. A. Clark, J. R. Kramer, and G. W. Vetrovec. Cardiac catherization 1990: a report of the Registry of the Society for Cardiac Angiography and Interventions. *Cathet Cardiovasc Diagn*, 24:75–83, Oct 1991.

[24] S. Paulin, G. K. von Schulthess, E. Fossel, and H. P. Krayenbuehl. MR imaging of the aortic root and proximal coronary arteries. *AJR Am J Roentgenol*, 148:665–670, Apr 1987.

[25] S. E. Nissen and P. Yock. Intravascular ultrasound: novel pathophysiological insights and current clinical applications. *Circulation*, 103:604–616, Jan 2001.

[26] Y. Uchida, F. Nakamura, T. Tomaru, T. Morita, T. Oshima, T. Sasaki, S. Morizuki, and J. Hirose. Prediction of acute coronary syndromes by percutaneous coronary angioscopy in patients with stable angina. *Am. Heart J.*, 130:195–203, Aug 1995.

[27] S. E. Nissen, J. C. Gurley, C. L. Grines, D. C. Booth, R. McClure, M. Berk, C. Fischer, and A. N. DeMaria. Intravascular ultrasound assessment of lumen size and wall morphology in normal subjects and patients with coronary artery disease. *Circulation*, 84:1087–1099, Sep 1991.

[28] C. Herzog, S. A. Nguyen, G. Savino, P. L. Zwerner, J. Doll, C. D. Nielsen, T. G. Flohr, T. J. Vogl, P. Costello, and U. J. Schoepf. Does two-segment image reconstruction at 64-section CT coronary angiography improve image quality and diagnostic accuracy? *Radiology*, 244:121–129, Jul 2007.

[29] T. J. Vrtiska, J. G. Fletcher, and C. H. McCollough. State-of-the-art imaging with 64-channel multidetector CT angiography. *Perspect Vasc Surg Endovasc Ther*, 17:3–8, Mar 2005.

[30] M. J. Budoff, D. Dowe, J. G. Jollis, M. Gitter, J. Sutherland, E. Halamert, M. Scherer, R. Bellinger, A. Martin, R. Benton, A. Delago, and J. K. Min. Diagnostic performance of 64-multidetector row coronary computed tomographic angiography for evaluation of coronary artery stenosis in individuals without known coronary artery disease: results from the prospective multicenter ACCURACY (Assessment by Coronary Computed Tomographic Angiography of Individuals Undergoing Invasive Coronary Angiography) trial. *J. Am. Coll. Cardiol.*, 52:1724–1732, Nov 2008.

[31] H. H. Oei, R. Vliegenthart, A. E. Hak, A. Iglesias del Sol, A. Hofman, M. Oudkerk, and J. C. Witteman. The association between coronary calcification assessed by electron beam computed tomography and measures of extracoronary atherosclerosis: the Rotterdam Coronary Calcification Study. *J. Am. Coll. Cardiol.*, 39:1745–1751, Jun 2002.

[32] R. Virmani, A. P. Burke, A. Farb, and F. D. Kolodgie. Pathology of the unstable plaque. *Prog Cardiovasc Dis*, 44:349–356, 2002.

[33] M. Vembar, M. J. Garcia, D. J. Heuscher, R. Haberl, D. Matthews, G. E. Bohme, and N. L. Greenberg. A dynamic approach to identifying desired physiological phases for cardiac imaging using multislice spiral CT. *Med Phys*, 30:1683–1693, Jul 2003.

[34] J. Barkhausen, P. Hunold, M. Jochims, H. Eggebrecht, G. V. Sabin, R. Erbel, and J. F. Debatin. Comparison of gradient-echo and steady state free precession sequences for 3D-navigator MR angiography of coronary arteries. *Rofo*, 174:725–730, Jun 2002.

[35] C. U. Herborn, J. Barkhausen, I. Paetsch, P. Hunold, M. Mahler, K. Shamsi, and E. Nagel. Coronary arteries: contrast-enhanced MR imaging with SH L 643A–experience in 12 volunteers. *Radiology*, 229:217–223, Oct 2003.

[36] F. Sardanelli, F. Zandrino, G. Molinari, A. Iozzelli, M. Balbi, and A. Barsotti. MR evaluation of coronary stents with navigator echo and breath-hold cine gradient-echo techniques. *Eur Radiol*, 12:193–200, Jan 2002.

[37] Z. A. Fayad, V. Fuster, J. T. Fallon, T. Jayasundera, S. G. Worthley, G. Helft, J. G. Aguinaldo, J. J. Badimon, and S. K. Sharma. Noninvasive in vivo human coronary artery lumen and wall imaging using black-blood magnetic resonance imaging. *Circulation*, 102:506–510, Aug 2000.

[38] M. Stuber, R. M. Botnar, K. V. Kissinger, and W. J. Manning. Free-breathing black-blood coronary MR angiography: initial results. *Radiology*, 219:278–283, Apr 2001.

[39] R. M. Botnar, M. Stuber, K. V. Kissinger, W. Y. Kim, E. Spuentrup, and W. J. Manning. Noninvasive coronary vessel wall and plaque imaging with magnetic resonance imaging. *Circulation*, 102:2582–2587, Nov 2000.

[40] P. A. Wielopolski, R. J. van Geuns, P. J. de Feyter, and M. Oudkerk. Coronary arteries. *Eur Radiol*, 10:12–35, 2000.

[41] M. S. Dirksen, H. J. Lamb, R. van der Geest, and A. de Roos. Toward comparability of coronary magnetic resonance angiography: proposal for a standardized quantitative assessment. *Eur Radiol*, 13:2353–2357, Oct 2003.

[42] Y. Wang, E. Vidan, and G. W. Bergman. Cardiac motion of coronary arteries: variability in the rest period and implications for coronary MR angiography. *Radiology*, 213:751–758, Dec 1999.

[43] P. G. Danias, M. Stuber, R. M. Botnar, K. V. Kissinger, R. R. Edelman, and W. J. Manning. Relationship between motion of coronary arteries and diaphragm during free breathing: lessons from real-time MR imaging. *AJR Am J Roentgenol*, 172:1061–1065, Apr 1999.

[44] O. L. Wade. Movements of the thoracic cage and diaphragm in respiration. *J. Physiol. (Lond.)*, 124:193–212, May 1954.

[45] P. Cluzel, T. Similowski, C. Chartrand-Lefebvre, M. Zelter, J. P. Derenne, and P. A. Grenier. Diaphragm and chest wall: assessment of the inspiratory pump with MR imaging-preliminary observations. *Radiology*, 215:574–583, May 2000.

[46] S. A. Nehmeh, Y. E. Erdi, T. Pan, E. Yorke, G. S. Mageras, K. E. Rosenzweig, H. Schoder, H. Mostafavi, O. Squire, A. Pevsner, S. M. Larson, and J. L. Humm. Quantitation of respiratory motion during 4D-PET/CT acquisition. *Med Phys*, 31:1333–1338, Jun 2004.

[47] K. C. McCall and R. Jeraj. Dual-component model of respiratory motion based on the periodic autoregressive moving average (periodic ARMA) method. *Phys Med Biol*, 52:3455–3466, Jun 2007.

[48] Kevin F. King Matt A. Bernstein and Xiaohong Joe Zhou. *Handbook of MRI Pulse Sequences*. Elsevier, Oxford, UK, 2004.

[49] Ronan O'Rahilly and Fabiola Muller. *Basic Human Anatomy: A Regional Study of Human Structure*. WB Saunders, 1982.

[50] G. Shechter, C. Ozturk, J. R. Resar, and E. R. McVeigh. Respiratory motion of the heart from free breathing coronary angiograms. *IEEE Trans Med Imaging*, 23:1046–1056, Aug 2004.

[51] J. Keegan, P. Gatehouse, G. Z. Yang, and D. Firmin. Coronary artery motion with the respiratory cycle during breath-holding and free-breathing: implications for slice-followed coronary artery imaging. *Magn Reson Med*, 47:476–481, Mar 2002.

[52] K. Nehrke, P. Bornert, D. Manke, and J. C. Bock. Free-breathing cardiac MR imaging: study of implications of respiratory motion–initial results. *Radiology*, 220:810–815, Sep 2001.

[53] A. M. Taylor, J. Keegan, P. Jhooti, D. N. Firmin, and D. J. Pennell. Calculation of a subject-specific adaptive motion-correction factor for improved real-time navigator echo-gated magnetic resonance coronary angiography. *J Cardiovasc Magn Reson*, 1:131–138, 1999.

[54] H. W. Korin, R. L. Ehman, S. J. Riederer, J. P. Felmlee, and R. C. Grimm. Respiratory kinematics of the upper abdominal organs: a quantitative study. *Magn Reson Med*, 23:172–178, Jan 1992.

[55] P. G. Danias, M. V. McConnell, V. C. Khasgiwala, M. L. Chuang, R. R. Edelman, and W. J. Manning. Prospective navigator correction of image position for coronary MR angiography. *Radiology*, 203:733–736, Jun 1997.

[56] A. M. Taylor, P. Jhooti, F. Wiesmann, J. Keegan, D. N. Firmin, and D. J. Pennell. MR navigator-echo monitoring of temporal changes in diaphragm position: implications for MR coronary angiography. *J Magn Reson Imaging*, 7:629–636, 1997.

[57] R. J. van Geuns, P. A. Wielopolski, B. J. Rensing, P. M. van Ooijen, M. Oudkerk, and P. J. de Feyter. Magnetic resonance imaging of the coronary arteries: anatomy of the coronary arteries and veins in three-dimensional imaging. *Coron. Artery Dis.*, 10:261–267, Jun 1999.

[58] C. L. Schultz, R. J. Alfidi, A. D. Nelson, S. Y. Kopiwoda, and M. E. Clampitt. The effect of motion on two-dimensional Fourier transformation magnetic resonance images. *Radiology*, 152:117–121, Jul 1984.

[59] M. L. Wood, V. M. Runge, and R. M. Henkelman. Overcoming motion in abdominal MR imaging. *AJR Am J Roentgenol*, 150:513–522, Mar 1988.

[60] M. L. Wood and R. M. Henkelman. Suppresion of respiratory motion artifacts in magnetic resonance imaging. *Med. Phys.*, 13:794–805, 1986.

[61] L. Axel, R. M. Summers, H. Y. Kressel, and C. Charles. Respiratory effects in two-dimensional Fourier transform MR imaging. *Radiology*, 160:795–801, Sep 1986.

[62] J. H. Maki, M. R. Prince, F. J. Londy, and T. L. Chenevert. The effects of time varying intravascular signal intensity and k-space acquisition order on three-dimensional MR angiography image quality. *J Magn Reson Imaging*, 6:642–651, 1996.

[63] R. L. Ehman and J. P. Felmlee. Adaptive technique for high-definition MR imaging of moving structures. *Radiology*, 173:255–263, Oct 1989.

[64] E. M. Haacke and J. L. Patrick. Reducing motion artifacts in two-dimensional Fourier transform imaging. *Magn Reson Imaging*, 4:359–376, 1986.

[65] P. Jhooti, F. Wiesmann, A. M. Taylor, P. D. Gatehouse, G. Z. Yang, J. Keegan, D. J. Pennell, and D. N. Firmin. Hybrid ordered phase encoding (HOPE): an improved approach for respiratory artifact reduction. *J Magn Reson Imaging*, 8:968–980, 1998.

[66] Y. Wang and R. L. Ehman. Retrospective adaptive motion correction for navigator-gated 3D coronary MR angiography. *J Magn Reson Imaging*, 11:208–214, Feb 2000.

[67] E. Atalar and L. Onural. A respiratory motion artifact reduction method in magnetic resonance imaging of the chest. *IEEE Trans Med Imaging*, 10:11–24, 1991.

[68] M. V. McConnell, V. C. Khasgiwala, B. J. Savord, M. H. Chen, M. L. Chuang, R. R. Edelman, and W. J. Manning. Prospective adaptive navigator correction for breath-hold MR coronary angiography. *Magn Reson Med*, 37:148–152, Jan 1997.

[69] J. A. Derbyshire, G. A. Wright, R. M. Henkelman, and R. S. Hinks. Dynamic scan-plane tracking using MR position monitoring. *J Magn Reson Imaging*, 8:924–932, 1998.

[70] D. J. Atkinson and R. R. Edelman. Cineangiography of the heart in a single breath hold with a segmented turboFLASH sequence. *Radiology*, 178:357–360, Feb 1991.

[71] H. Sakuma, N. Kawada, H. Kubo, Y. Nishide, K. Takano, N. Kato, and K. Takeda. Effect of breath holding on blood flow measurement using fast velocity encoded cine MRI. *Magn Reson Med*, 45:346–348, Feb 2001.

[72] D. A. Feinberg, N. M. Rofsky, and G. Johnson. Multiple breath-hold averaging (MBA) method for increased SNR in abdominal MRI. *Magn Reson Med*, 34:905–909, Dec 1995.

[73] P. G. Danias, M. Stuber, R. M. Botnar, K. V. Kissinger, M. L. Chuang, and W. J. Manning. Navigator assessment of breath-hold duration: impact of supplemental oxygen and hyperventilation. *AJR Am J Roentgenol*, 171:395–397, Aug 1998.

[74] R. L. Ehman, M. T. McNamara, M. Pallack, H. Hricak, and C. B. Higgins. Magnetic resonance imaging with respiratory gating: techniques and advantages. *AJR Am J Roentgenol*, 143:1175–1182, Dec 1984.

[75] D. R. Bailes, D. J. Gilderdale, G. M. Bydder, A. G. Collins, and D. N. Firmin. Respiratory ordered phase encoding (ROPE): a method for reducing respiratory motion artefacts in MR imaging. *J Comput Assist Tomogr*, 9:835–838, 1985.

[76] Y. Wang, R. C. Grimm, J. P. Felmlee, S. J. Riederer, and R. L. Ehman. Algorithms for extracting motion information from navigator echoes. *Magn Reson Med*, 36:117–123, Jul 1996.

[77] H. A. Ward, S. J. Riederer, R. C. Grimm, R. L. Ehman, J. P. Felmlee, and C. R. Jack. Prospective multiaxial motion correction for fMRI. *Magn Reson Med*, 43:459–469, Mar 2000.

[78] Y. L. Liu, S. J. Riederer, P. J. Rossman, R. C. Grimm, J. P. Debbins, and R. L. Ehman. A monitoring, feedback, and triggering system for reproducible breath-hold MR imaging. *Magn Reson Med*, 30:507–511, Oct 1993.

[79] E. Nagel, A. Bornstedt, B. Schnackenburg, J. Hug, H. Oswald, and E. Fleck. Optimization of realtime adaptive navigator correction for 3D magnetic resonance coronary angiography. *Magn Reson Med*, 42:408–411, Aug 1999.

[80] D. Manke, K. Nehrke, P. Bornert, P. Rosch, and O. Dossel. Respiratory motion in coronary magnetic resonance angiography: a comparison of different motion models. *J Magn Reson Imaging*, 15:661–671, Jun 2002.

[81] R. W. Fischer, R. M. Botnar, K. Nehrke, P. Boesiger, W. J. Manning, and D. C. Peters. Analysis of residual coronary artery motion for breath hold

and navigator approaches using real-time coronary MRI. *Magn Reson Med*, 55:612–618, Mar 2006.

[82] D. Manke, K. Nehrke, and P. Bornert. Novel prospective respiratory motion correction approach for free-breathing coronary MR angiography using a patient-adapted affine motion model. *Magn Reson Med*, 50:122–131, Jul 2003.

[83] C. Jahnke, K. Nehrke, I. Paetsch, B. Schnackenburg, R. Gebker, E. Fleck, and E. Nagel. Improved bulk myocardial motion suppression for navigator-gated coronary magnetic resonance imaging. *J Magn Reson Imaging*, 26:780–786, Sep 2007.

[84] J. Sra, D. Krum, A. Malloy, M. Vass, B. Belanger, E. Soubelet, R. Vaillant, and M. Akhtar. Registration of three-dimensional left atrial computed tomographic images with projection images obtained using fluoroscopy. *Circulation*, 112:3763–3768, Dec 2005.

[85] J.J.K. O'Ruanaidh and T. Pun. Rotation, scale and translation invariant digital image watermarking. *Signal Processing*, 66:303–317, 1998.

[86] D. Manke, P. Rosch, K. Nehrke, P. Bornert, and O. Dossel. Model evaluation and calibration for prospective respiratory motion correction in coronary MR angiography based on 3-D image registration. *IEEE Trans Med Imaging*, 21:1132–1141, Sep 2002.

[87] T. Deguillaume. A method for the estimation and recovering from general affine transformation in digital watermarking applications. *IS&T/SPIE's 14th Annual Symposium, Electronic Imaging 2002: Security and Watermarking of Multimedia Contents IV*, 4675:313–322, 2002.

[88] K. Nehrke and P. Bornert. Prospective correction of affine motion for arbitrary MR sequences on a clinical scanner. *Magn Reson Med*, 54:1130–1138, Nov 2005.

[89] S.D. Roes, G. Korosoglou, Schar M., and et al. Correction for heart rate variability during 3D whole heart MR coronary angiography. *J Magn Reson Imaging*, 27:1046–1053, 2008.

[90] West J. *Respiratory Physiology.* Williams and Wilkins, Baltimore, 1995.

[91] Sherwood Lauralee. *Fundamentals of Physiology: A Human Perspective.* Thomson Books, 2006.

[92] T. Okada, S. Kanao, A. Ninomiya, S. Sato, S. Kuhara, T. Kamae, K. Gotoh, and K. Togashi. Whole-heart coronary magnetic resonance angiography with parallel imaging: comparison of acceleration in one-dimension vs. two-dimensions. *Eur J Radiol*, 71:486–491, Sep 2009.

[93] R. M. Botnar, M. Stuber, P. G. Danias, K. V. Kissinger, and W. J. Manning. Improved coronary artery definition with T2-weighted, free-breathing, three-dimensional coronary MRA. *Circulation*, 99:3139–3148, Jun 1999.

[94] D. Li, J. Zheng, and H. J. Weinmann. Contrast-enhanced MR imaging of coronary arteries: comparison of intra- and extravascular contrast agents in swine. *Radiology*, 218:670–678, Mar 2001.

[95] M. B. Hofman, R. E. Henson, S. J. Kovacs, S. E. Fischer, R. B. Lauffer, K. Adzamli, J. De Becker, S. A. Wickline, and C. H. Lorenz. Blood pool agent strongly improves 3D magnetic resonance coronary angiography using an inversion pre-pulse. *Magn Reson Med*, 41:360–367, Feb 1999.

[96] L. O. Hall J. C. Bezdek and L. P. Clarke. Review of MR image segmentation techniques using pattern recognition. *Med. Phys.*, 20:1033–1048, 1993.

[97] Ulaş Bağcı, Jayaram K. Udupa, and Li Bai. The role of intensity standardization in medical image registration. *Pattern Recogn. Lett.*, 31:315–323, March 2010.

[98] R. Kikinis, M. E. Shenton, G. Gerig, J. Martin, M. Anderson, D. Metcalf, C. R. Guttmann, R. W. McCarley, W. Lorensen, and H. Cline. Routine quantitative analysis of brain and cerebrospinal fluid spaces with MR imaging. *J Magn Reson Imaging*, 2:619–629, 1992.

[99] L. G. Nyul and J. K. Udupa. On standardizing the MR image intensity scale. *Magn Reson Med*, 42:1072–1081, Dec 1999.

[100] M. R. Fisher, M. T. McNamara, and C. B. Higgins. Acute myocardial infarction: MR evaluation in 29 patients. *AJR Am J Roentgenol*, 148:247–251, Feb 1987.

[101] W. A. Edelstein, P. A. Bottomley, and L. M. Pfeifer. A signal-to-noise calibration procedure for NMR imaging systems. *Med Phys*, 11:180–185, 1984.

[102] T. Yamamoto, T. Nambu, K. Miyasaka, and Y. Morita. Accurate and practical calibration of MR signal intensities by the new transmission amplitude method: Application of the numerical diagnosis to MRI. *Radiology*, 209:1582, 1998.

[103] W. M. Wells, W. L. Grimson, R. Kikinis, and F. A. Jolesz. Adaptive segmentation of MRI data. *IEEE Trans Med Imaging*, 15:429–442, 1996.

[104] M. N. Ahmed, S. M. Yamany, N. Mohamed, A. A. Farag, and T. Moriarty. A modified fuzzy C-means algorithm for bias field estimation and segmentation of MRI data. *IEEE Trans Med Imaging*, 21:193–199, Mar 2002.

[105] Y. Ge, J. K. Udupa, L. G. Nyul, L. Wei, and R. I. Grossman. Numerical tissue characterization in MS via standardization of the MR image intensity scale. *J Magn Reson Imaging*, 12:715–721, Nov 2000.

[106] P. Hellier. Consistent intensity correction of MRI images. pages 1109–1112, 2003.

[107] Frericks B et al Jager F, Deuerling-Zheng Y. A new method for MRI intensity standardization with application to lesion detection in the brain.

[108] M. E. Moseley, J. Kucharczyk, H. S. Asgari, and D. Norman. Anisotropy in diffusion-weighted MRI. *Magn Reson Med*, 19:321–326, Jun 1991.

[109] P. J. Basser, J. Mattiello, and D. LeBihan. MR diffusion tensor spectroscopy and imaging. *Biophys. J.*, 66:259–267, Jan 1994.

[110] R. K. Gupta, S. Saksena, A. Agarwal, K. M. Hasan, M. Husain, V. Gupta, and P. A. Narayana. Diffusion tensor imaging in late posttraumatic epilepsy. *Epilepsia*, 46:1465–1471, Sep 2005.

[111] E. Spuentrup, A. Buecker, G. Adam, J. J. van Vaals, and R. W. Guenther. Diffusion-weighted MR imaging for differentiation of benign fracture edema and tumor infiltration of the vertebral body. *AJR Am J Roentgenol*, 176:351–358, Feb 2001.

[112] J. Modersitzki. *Numerical methods for image registration.* Oxford Univ. Press, New York, 2004.